Coherence in Rydberg Atoms: Measurement and Control

Mary Kutteruf
Coeur d'Alene, ID

A.B. Bryn Mawr College, 2003

A Dissertation presented to the Graduate Faculty
of the University of Virginia in Candidacy for the Degree of
Doctor of Philosophy

Department of Physics

University of Virginia
December, 2010

Abstract

We demonstrate a variety of techniques for measuring and controlling dephasing and decoherence in alkali metal Rydberg atom systems. Specifically, we investigate the coherence of the spin-orbit interaction in individual atoms and of dipole-dipole resonant energy exchange between pairs of atoms. Rydberg atoms are a good model system for exploring decoherence because they are sensitive to noise in their environments.

The phase coherence of wave packets encoded on the fine-structure Rydberg states of lithium atoms is measured using a population echo and preserved using pulsed and continuous dynamic decoupling techniques. Pulsed electric fields toggle the spin-orbit coupling, repeatedly flipping the state vector, and preventing the slow acquisition of phase noise in a bang-bang scheme. Continuous dynamic decoupling is implemented by driving population between the relevant electronic states with a resonant rf field. The energy spacing between the levels is locked to the rf frequency as long as the Rabi rate is much greater than the dephasing rate.

We demonstrate a technique which reduces the average relative velocity between interacting potassium Rydberg atoms, extending the atom transit time and allowing us to control when all resonant energy exchange interactions in the ensemble begin and end. Velocity reduction is achieved without the use of a chopper wheel by exciting a small cylinder of atoms and allowing them to thermally expand prior to tuning them into resonance.

Resonant energy transfer is explored further in a nearly frozen rubidium Rydberg gas. We observe enhancement in the transition signal when the probability amplitudes acquired on opposite sides of the resonance interfere constructively compared to the population transferred when remaining on either side of the resonance. This enhancement reflects the coherence of the energy exchange interaction and decays over 10 μs microseconds. The observed coherence time is much longer than previously measured dephasing times in nearly frozen Rydberg gases.

Contents

List of Figures

Acknowledgements

I would like to begin by thanking the American taxpayers who have provided funding for me and my work through grants from the Air Force Office of Scientific Research and the National Science Foundation, including the NSF IGERT SELIM program. I would also like to acknowledge financial support from the University of Virginia through UVA FEST and from the Physics Department through a semester teaching assistantship. Thanks also go to my advisor, Prof. Bob Jones, for writing the grant proposals that funded this research and to Ian Harrison who administered the SELIM program.

Of course, Prof. Jones has provided much more than financial support over the last seven years. His guidance and insight have been invaluable and I am deeply grateful. His help and patience have made this research possible.

Many other faculty members have helped me along this journey. I would like to thank the members of my research committee, Prof. Hirosky and Prof. Pfister, for their helpful comments over the years. Prof. Sackett and his research group have provided insight in getting the magneto-optical trap working and making accurate measurements of its characteristics. They also loaned me a diode laser while our repumping laser was being repaired. Prof. Gallagher and his lab also provided invaluable help in setting up the MOT as well as in allowing me to borrow whatever I might need. They also raised interesting questions about my research in joint group meetings and shared productive feedback on presentations before conferences.

I have been fortunate to work with great people on all of my experiments. The lithium experiments were originally set up by Dr. Lung Ko. I worked closely with Dr. Russell Minns on taking the data shown in chapter 3, and Melissa Dolph joined the group for a summer to help Russell take the data for chapter 4. John White worked on the potassium experiment with me for a summer and wrote the Lab View code used to record the resonance width data shown in chapters 5 and 6. Dr. Thibault Vogt showed me how to put the MOT together and helped me get the rubidium experiment started. I am grateful for the hard work of Prof. Charles Conover and Hussain Zaidi in writing and modifying Shaper5, the data collection program which facilitated the collection of much of the data contained in this thesis.

I am also grateful for the insight and humor of the other graduate students in the Jones group. Jeremy Murray-Krezan showed me the ropes of the lab when I worked with him during the summer before my first year of graduate school and always provided insight into the mysterious inter-workings of the lab and the Bob. Xiangdong Zhang was the lab computer master and was always willing to lend a helping hand. I was fortunate to have group members working across the street in the Chemistry building, Kelsie Betsch, Dan Pinkham and Brett Sickmiller, to remind me that molecules are evil, complicated systems that I want nothing to do with.

Thanks also goes to my college friend Molly Clarkson who was generous enough to copy edit my dissertation thus preventing excessive violence against the English language.

I had a great group of graduate students in my incoming class and I learned a great deal from all of them. I would like to thank Justin Wright and Po-Shan Leang for their friendship and support over the last seven years. Thanks to Melissa Bloomer for letting me keep her husband as my "physics boyfriend," and to Russell Bloomer for being my friend and companion on the road of experiment failure for the last seven years.

I would be remiss in not acknowledging the people who really put me on the path to getting my PhD in physics at UVA. Prof. Mike Noel is the inspiring teacher and scientist who first introduced to to the fascinating world of Rydberg atoms and I am deeply grateful. I'm also deeply indebted to Ed Tyllia who first focused my interest in science back in high school.

Last but certainly not least, I would like to thank my family. I have been lucky to have the love and support of my parents, Chris Kutteruf and Anita Robinson. I would not be here without them. I also have to thank my sister, Rachel Kutteruf. It's hard to make me look good all the time, but Rachel has always tried hard, and for that I am grateful.

Chapter 1

Introduction

This dissertation focuses on measuring and preserving coherence in Rydberg atom systems. Classically, the relative coherence of waves is critical for observing constructive and destructive interference between them. Similarly, in quantum systems, coherence is required to observe phenomena related to interference and/or entanglement. Therefore, maintaining coherence is fundamental to the study of the wave nature of quantum systems and of few and many body quantum phenomena. Furthermore, knowledge of the mechanisms through which a system loses coherence is key to understanding, and perhaps, controlling dynamics of that system. This becomes more challenging as the number of degrees of freedom in a system, and the number of interactions between system elements and their environment increases.

The relevance of coherence goes well beyond academic interest in the fundamental quantum nature of the universe. For example, the quantum properties of interference, entanglement and superposition hold the promise of a powerful new paradigm in information processing. Of particular interest to physicists is Richard Feynman's 1982 prediction that a quantum computer could be used to simulate quantum systems, a task beyond the computing power of classical computers then and now [7]. Three years later, David Deutsch expanded this idea, proving that, in principle, a quantum computer could be used to perfectly model any physical system [8]. Outside of the physics community, much of the interest in quantum computing has focused on Peter Shor's 1994 invention of an algorithm which would enable a quantum computer to quickly factor large numbers to their primes, as many standard cryptographic methods gain their strength from the inability of computers to factor large numbers [9, 10].

Quantum computation requires the ability to control individual quantum systems and interactions between quantum systems in order to create entanglement and implement quantum gates. It is also necessary to control interactions between quantum systems and their environments as uncontrolled interaction can destroy entanglement and quantum information. Understanding and controlling decoherence is, therefore, an active area of investigation [4, 5, 11–34] in fundamental quantum mechanics and for practical applications.

1.1 Quantum Coherence

Light from a continuous wave laser is coherent because it has a predictable phase, while light from a hot filament is incoherent because the light emitted has a random phase. Similarly, a two (or more) level quantum system is coherent as long as there is a predictable or well-defined phase between the levels. The wave function of such a superposition or wave packet can be expressed as

$$\Psi = \alpha \left|1\right\rangle + \sqrt{1-\alpha^2}e^{-i\phi(t)} \left|2\right\rangle = \begin{pmatrix} \alpha \\ \sqrt{1-\alpha^2}e^{-i\phi(t)} \end{pmatrix} \tag{1.1}$$

where $\phi(t)$ is the phase. In the eigenbasis of the Hamiltonian, the phase between the levels evolves such that $\phi(t) = \phi_0 - iEt/\hbar$, where ϕ_0 is the phase at $t = 0$, E is the energy difference between the levels, and t is time. If E changes with time in an unpredictable way, the phase, $\phi(t)$, is no longer well-defined and the system looses its coherence.

Phase coherence is required for waves to interfere. As the phase between two waves is varied in a controlled manner, the pattern of constructive and destructive interference changes, as in a Michelson interferometer. When the relative phase of the waves is well-defined, a predictable interference pattern results. No such interference results from waves viewed over a time interval that exceeds their mutual coherence time. In quantum systems, interference can be observed by rotating the state vector via unitary transformations such that phase variations between the states are mapped to variation in probability differences between the states.

In the experiments discussed in this dissertation, we observe ensembles of many nominally identical quantum systems. If the energy level spacing varies across the ensemble, phase will be acquired at different rates in different parts of the ensemble. Consider two atoms A and B, each of which have two states $|1\rangle$ and $|2\rangle$ that are separated by an electric field dependent energy E. If atom A is in a different field than atom B, $E_A = E$ will be different than $E_B = E + \delta$ and the atoms will acquire phase at different rates, $\phi_A(t) = -iEt/\hbar$ and $\phi_B(t) = -i(E+\delta)t/\hbar$. Therefore, the wavepackets on each atom will go in and out of phase with each other while each remains perfectly coherent. In an ensemble of hundreds or thousands of atoms, this inhomogeneous dephasing can completely obscure coherence of the system.

Decoherence and dephasing were first explored in the 1950s in spin system using nuclear magnetic resonance (NMR) [35–37], and many of the techniques for measuring and controlling dephasing in quantum systems derive from that work. A powerful technique from NMR is the use of "echoes" to separate the effects of dephasing and decoherence as will be shown in chapter 3 [35]. As long as the energy between the states does not vary with time, the dephasing of the ensemble can be reversed by flipping the state vector after a time T and allowing it to evolve for an additional time T. Flipping the state vector effectively reverses the sign of $\phi(T)$, so at $t = 2T$ the $\phi(T) = \phi_0$ for all time independent values of E,

$$\begin{aligned}
\Psi(t=0) &= \begin{pmatrix} \alpha \\ \sqrt{1-\alpha^2}e^{i\phi_0} \end{pmatrix} \xrightarrow{propagate} \Psi(t=T) = \begin{pmatrix} \alpha \\ \sqrt{1-\alpha^2}e^{-i(ET/\hbar-\phi_0)} \end{pmatrix} \xrightarrow{flip} \\
\Psi(t=T) &= \begin{pmatrix} \sqrt{1-\alpha^2}e^{-i(ET/\hbar-\phi_0)} \\ \alpha \end{pmatrix} = \begin{pmatrix} \sqrt{1-\alpha^2} \\ \alpha e^{i(ET/\hbar-\phi_0)} \end{pmatrix} \xrightarrow{propagate} \\
\Psi(t=2T) &= \begin{pmatrix} \sqrt{1-\alpha^2} \\ \alpha e^{i(ET/\hbar-\phi_0)-iET/\hbar} \end{pmatrix} = \begin{pmatrix} \sqrt{1-\alpha^2} \\ \alpha e^{-i\phi_0} \end{pmatrix} \xrightarrow{flip} \begin{pmatrix} \alpha \\ \sqrt{1-\alpha^2}e^{i\phi_0} \end{pmatrix}.
\end{aligned} \tag{1.2}$$

If E is changing on a time scale less than T, the phase cancelation will not be complete. Observing how accurately the initial state is recovered with increasing T provides a measure of the coherence of the system. For quantum systems in which there is no efficient method to flip the state vector, alternative methods have been developed to probe dephasing and decoherence [38–40]. In chapter 6, we will discuss a novel technique for probing coherent interactions between cold Rydberg atoms.

Probably the simplest way to prevent decoherence is to choose a quantum system in which the energy spacing is unaffected by changes in the surrounding environment and there are no additional interactions which might cause undesirable phase acquisition [17, 18]. However, for many quantum systems such decoherence free subspaces are not naturally occurring and even small time dependent variations in local fields will lead to decoherence. Chapters 3 and 4 focus on preserving coherence through the use of dynamic decoupling. In chapter 3, we show that if the variation in E is sufficiently slow, decoherence can be prevented using pulsed dynamic decoupling in which a series of echoes repeatedly flip the state vector, canceling the phase before the energy spacing can change as in spin-flip narrowing in NMR [36, 37][5]. Alternatively, in analogy with spin-locking, the phase evolution can be driven with a resonant field, locking the energy separation to the field frequency, as will be

Table 1.1: Atomic units

Quantity	Atomic Unit	Definition
mass	electron mass m_e	9.1×10^{-31} kg
charge	proton charge e	1.6×10^{-19} C
length	Bohr radius $a_0 = \hbar^2/e^2m$	5.29×10^{-11} m
velocity	electron velocity in first Bohr orbit $v_0 = e^2/\hbar$	2.19×10^{6} m/s
energy	twice the ionization potential of hydrogen $e^2m/\hbar$	4.36×10^{-18} J
		27.2 eV
electric field	field at the first Bohr orbit $e/a^2 = e^5m^2/\hbar^4$	5.14×10^{9} V/cm
time	$a_0/v_0 = \hbar^3/e^4m$	2.42×10^{-17} s

shown in chapter 4 [4].

1.2 Atomic Units

Atomic units are defined by the properties of the ground state of hydrogen. This unit scale is convenient for atomic physics and will be used throughout this dissertation. Atomic units define

$$\hbar = m_e = e = 4\pi\varepsilon_0 = 1 \tag{1.3}$$

where $\hbar$ is Planck's constant divided by 2π, m_e is the mass of the electron, $-e$ is the charge of the electron, and ε_0 is the permittivity of free space. Table 1.1 lists the definitions of various atomic units.

1.3 Rydberg Atoms

The experiments discussed in this dissertation involve exciting alkali metal atoms (specifically ^{7}Li, ^{39}K and ^{85}Rb) to Rydberg states. Rydberg atoms are atoms in which an electron is excited to a state with a high principal quantum number ($n \gtrsim 10$) [41]. Due to their large orbits, the Rydberg electron is easily perturbed by environmental electric and magnetic fields, black body radiation and unwanted collisions. This makes Rydberg atoms excellent systems in which to explore decoherence and dephasing. The large polarizabilities and transition dipole moments which make Rydberg atoms susceptible to environmental noise are also responsible for the strong long range interactions that exist between Rydberg atoms. These interactions make Rydberg atoms candidates for quantum computation as they can be used to entangle Rydberg electrons and/or perform quantum logic [42–47].

Various properties of Rydberg atoms scale with the principal quantum number n. Of particular importance to the work presented here are the scalings of the binding energy ($W \propto n^{-2}$), the energy between adjacent n states ($\Delta W \propto n^{-3}$), the geometric cross section ($\sigma \propto n^4$), the dipole moment between adjacent states ($\mu \propto n^2$), and the polarizability ($\alpha \propto n^7$) [41]. To determine the matrix elements associated with these quantities, it is necessary to calculate the Rydberg electron wavefunctions for the states involved using quantum defect theory. The Rydberg electron spends most of its time near the classical outer turning point where the potential is similar to that created by a point charge. We therefore treat interactions with the core of unexcited inner electrons as a perturbation which shifts the energy of the excited electron such that

$$W = \frac{-Ry}{(n-\delta_\ell)^2} = \frac{-Ry}{n^{*2}} \tag{1.4}$$

where $Ry = k^2 e^4 m / 2\hbar^2 = 1/2$ in atomic units for a singly excited neutral atom ($k = 1/2\pi\varepsilon_0$), and δ_ℓ is the experimentally observed quantum defect for states with orbital angular momentum ℓ. In general, δ_ℓ is larger for the low angular momentum states as their highly elliptical orbits polarize and penetrate the core. Outside of the radius of the core, the Rydberg electron's wavefunction is similar to that of a hydrogenic electron, but the presence of the core electrons results in a phase shift in the radial wavefunction. The properties of Rydberg atoms in which we are interested depend on bound state wavefunctions outside the core [41] which are calculated via the Numerov method [48–51].

1.4 Resonant Energy Transfer

Resonant energy transfer occurs when a pair of atoms or molecules exchange energy, changing only their internal states as one partner is excited to a higher energy final state and the other is deexcited to a lower state. The energy exchange is often mediated by the dipole-dipole potential and occurs most efficiently if the energy separations of the initial and final states of both interacting partners are identical. Such near matches in energy spacing naturally occur in a number of atomic and molecular systems. Two of the most familiar such Förster resonances [52] provide parts of the population inversion mechanisms in carbon dioxide and helium neon lasers. In the former, CO_2 is excited from a ground state to the first asymmetric stretching states, (1,0,0) and (0,0,1), when N_2 dexcites from first vibrational state to its ground state, while in the HeNe laser, helium atoms in the 2^3S and 2^1S states exchange energy with ground state neon atoms exciting them to the 2s and 3s states respectively [53].

Rydberg atoms provide an ideal system for studying resonant energy transfer because the high density of states, and the variation in state separation with principal quantum number and angular momentum increases the probability of finding chance coincidences. Furthermore, Stark tuning to correct for small energy differences can be accomplished with modest electric fields. Varying the electric field allows for continuous tuning of the energy level separation, allowing for spectroscopy of the dipole-dipole resonances [41]. Chapters 5 and 6 describe using pulsed electric fields to control resonant energy exchange and discuss it in more detail.

1.5 Dissertation Structure

The remainder of this dissertation is divided into five chapters detailing experiments and one concluding chapter which summarizes our results and examines prospects for future work. We begin with a detailed description of the experimental apparatus used in the subsequent chapters. In the third chapter, we demonstrate the use of population echoes to measure and preserve the quantum coherence of single qubits stored in lithium Rydberg atoms [5]. In the following chapter, we describe using a radio frequency field to drive population between the constituent states in a wavepacket or qubit, preventing decoherence in a method analogous to spin locking in NMR [4]. Chapter five describes a new technique for reducing the relative velocities between Rydberg atoms in a thermal beam, in an experiment similar to one performed by Thomson, Renn and Gallagher [54]. By reducing the relative velocities of neighboring atoms before they interact, one can control when the dipole-dipole resonant energy exchange begins and ends for all of the interacting atoms. These experiments illustrate the coherence of Rydberg-Rydberg interactions in a random ensemble over short time scales. The final experimental chapter describes a novel method of coherence spectroscopy which allows us to confirm the coherence of the dipole-dipole interaction between cold Rydberg atoms over time scales on the order of the spontaneous emission time of the atoms.

Chapter 2

Experimental Setup

The experiments in this dissertation involve exciting atomic alkali metals to Rydberg states with laser light in high and ultra-high vacuum. This chapter will discuss the general experimental setup. The experiments are performed in the laser laboratory located in room 166 of the physics building. Heating and air conditioning systems are designed to maintain the lab temperature between 69 ^{0}F and 70 ^{0}F to stabilize sensitive equipment. To maintain the cleanliness vital to any laser laboratory, soldering and light machining take place in a shop area which is separated from the main lab by a divider and curtain. Two fume hoods allow for the proper handling of volatile chemicals. Optics not currently in use are stored in drawers to protect them from dust and other contaminants. Lasers, vacuum chambers and optics are secured on Newport RS 3000 optical tables which are designed to reduce mechanical vibration. Newport's I-2000 Series Isolator legs provide additional vibration reduction for some experiments. All experiments were preformed at a repetition rate of fifteen hertz.

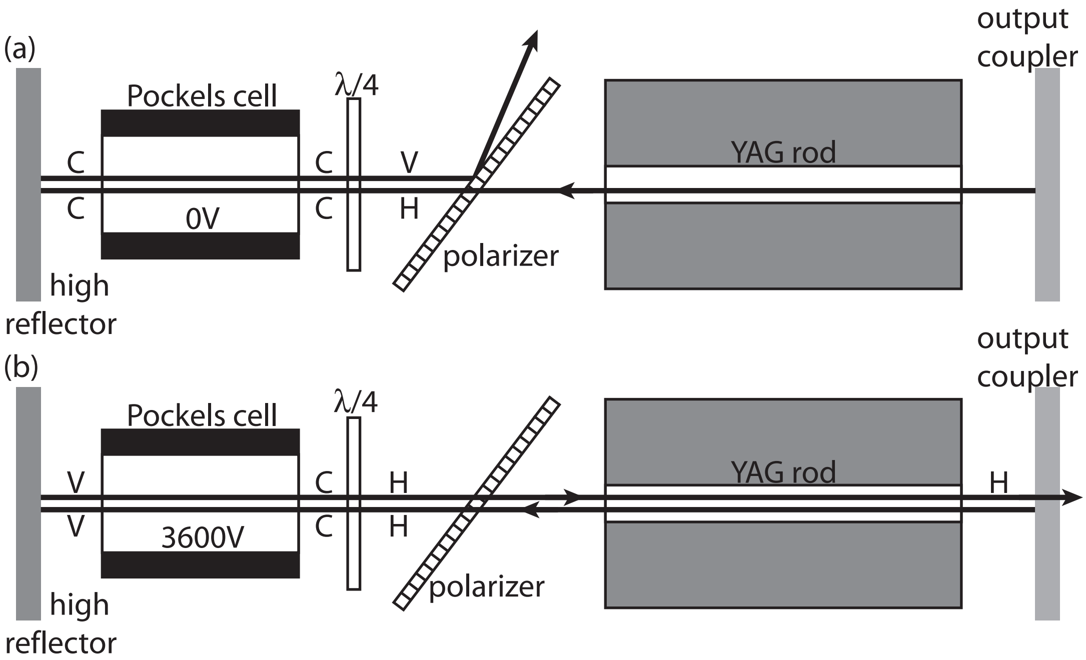

Figure 2.1: Schematic illustrating the Q-switch of the Surelight III Nd:YAG laser (a) closed and (b) open. The forward and backward light paths have been separated for clarity. H means horizontal polarization, V means vertical polarization and C means circular polarization [1].

2.1 Lasers

2.1.1 Nd:YAG Laser

A pulsed neodymium-doped yttrium aluminium garnet (Nd:$Y_3Al_5O_{12}$ or Nd:YAG) laser provides the foundation of these experiments, pumping the dye lasers and amplifiers used to excite Rydberg atoms. In the Continuum Surelite III laser, flashlamps pump a rod of YAG, exciting the Nd^{+3} ions to states which quickly decay to the $^4F_{3/2}$ state. The light emitted by the Nd^{+3} ions decaying to the $^4I_{1/2}$ level travels out of the rod, through a horizontal polarizer and a quarter-wave plate as shown in figure 2.1. The light then passes through a Pockels cell which does not change the polarization unless a voltage of approximately 3600 V is applied, in which case the light experiences a quarter wave rotation. Without this rotation, the light reflected back through the Pockels cell and quarter-wave plate arrives at the polarizer with vertical polarization and is rejected as shown in figure 2.1(a). When the Pockels cell is activated, the light passes through the polarizer and gain rod before being partially reflected by the output coupler, as in figure 2.1(b). Thus, the polarizer, wave plate and Pockels cell act as a Q-Switch preventing lasing until the gain in the rod is at its maximum (233 μs after the flashlamp fire) and then opening the cavity. This allows most of the gain to be swept out in a five nanosecond 1064 nm infrared (IR) pulse with high peak power. For these experiments, two Potassium Dihydrogen Phosphate (KDP) crystals generate additional beams at the second and third harmonics of the fundamental frequency resulting in light with wavelengths of 532 nm and 355 nm respectively [1]. The three beams are separated, and the fundamental is dumped while the second and third harmonics are used to pump different dye lasers and amplifiers as described in section 2.1.2.

2.1.2 Dye Lasers

Pulsed dye lasers are used to drive Rydberg excitations. When a solution of organic dye is excited by light, it fluoresces over range a wavelengths. By placing dye in a cavity, it is possible to stimulate this fluorescence and create a laser. Such a laser is tunable over the fluorescence band of the dye. Since different dyes fluoresce in bands from the infrared (LDS 925) to the ultraviolet (Stilbene 420), the laser color can easily be changed. For these experiments, Hansch [55] and Littman [56, 57] styles of lab-built dye lasers are used. In both, dye dissolved in methanol is circulated through a cell formed by a quartz cuvette so fresh dye is excited with every laser shot. Refreshing the dye is necessary as the dye molecules can take a long time to relax all the way back to the ground state. The second or third harmonic of the Nd:YAG (depending on the dye) is focused about a millimeter into the dye cell by a cylindrical lens, creating a line of gain medium across the face of the cell.

In the Hansch-style laser shown in figure 2.2, light leaving the dye cell along the laser path is expanded by a telescope onto a grating. The angle of the grating determines the wavelength of light that is diffracted back into the laser cavity. The light passes back

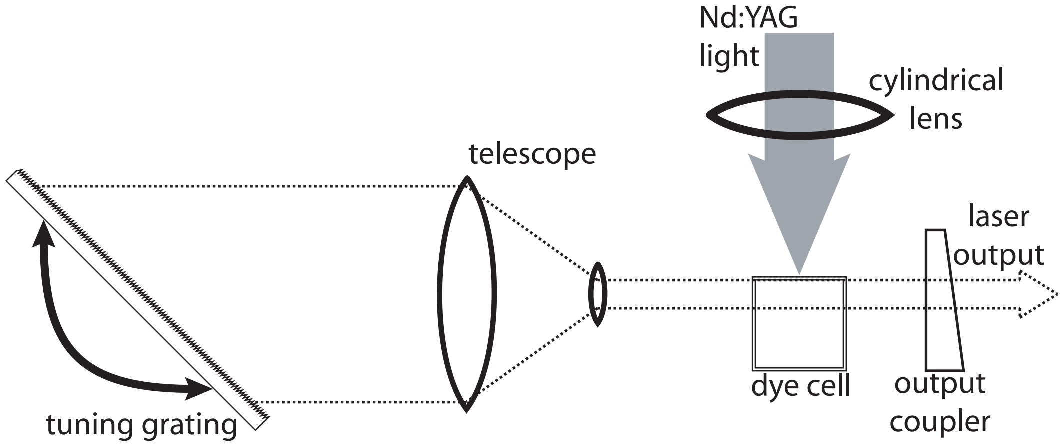

Figure 2.2: Schematic for a Hansch dye laser

through the dye cell, before reaching the glass wedge which serves as the output coupler allowing the majority of the light to escape from the cavity [55]. These lasers typically have line widths on the order of 1 cm^{-1}. Hansch lasers are generally selected to drive low lying transitions that do not require a more refined line width and where the superior power stability is an asset. They can also offer more power than the Littman lasers, making them ideal for processes which are less efficient than atomic transitions such as harmonic generation.

Littman-style dye lasers achieve narrower line widths than do Hansch lasers. As shown in figure 2.3, light leaving the dye is retro-reflected through the cell before striking a grating at grazing incidence. The zero order reflection provides the laser's output, while the first order diffraction is directed back onto the grating and into the laser cavity by the tuning mirror. Changing the angle of the tuning mirror changes the wavelength of the laser [56, 57]. The line width can be narrowed further by replacing the tuning mirror with a second grating which diffracts its first order back into the cavity, although this tends to increase the laser's power and its frequency instability. A double-grating Littman laser can create laser pulses with a line width of 0.14 cm^{-1} [58]. The pulses from both Littman and Hansch lasers have durations comparable to the duration of the pumping light pulse.

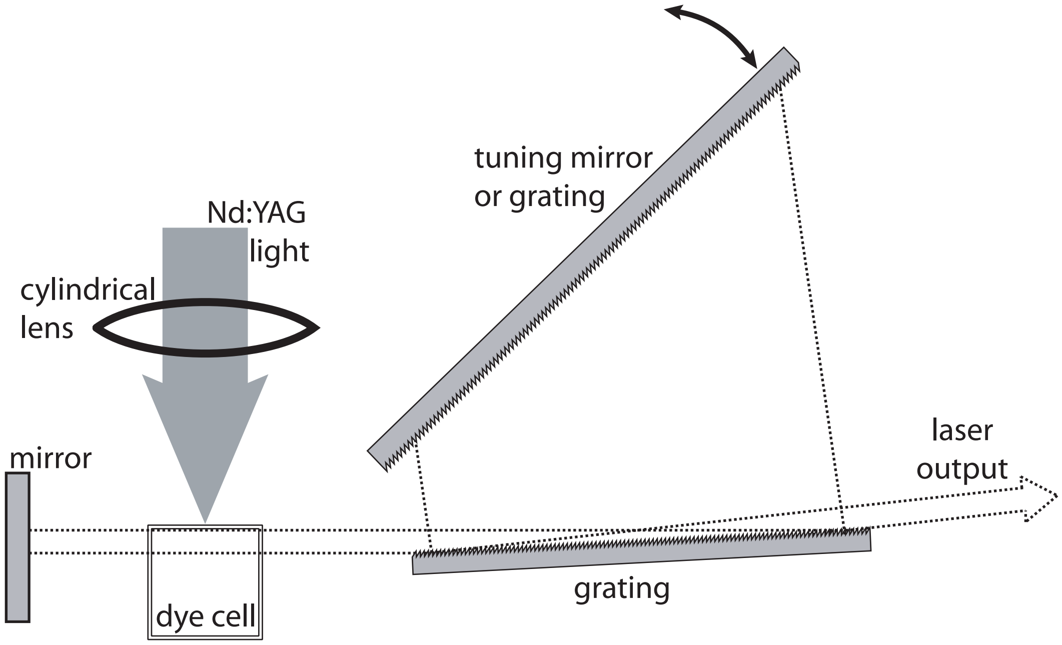

Figure 2.3: Schematic for a Littman dye laser

A related technique can be used to create a single pass amplifier. A dilute solution of dye (typically 10-30% of the concentration used in a laser) is circulated through a dye cell. A cylindrical lens focuses the pump light into the cell, creating a two millimeter tall line of excited dye. Light from any source which lies within the frequency range of the dye that passes through the excited dye will be amplified. This technique is often used to amplify dye lasers or other lasers which have a desirable mode structure but low power.

2.1.3 Diode Lasers

The Vortex tunable diode lasers from New Focus, used to cool rubidium atoms in the magneto-optical trap (MOT) discussed in section 2.4, work on the same principle as the Littman dye laser described in section 2.1.2. In this external cavity diode laser shown in figure 2.4, light from the diode is collimated onto a grating at grazing incidence. As in the dye laser, the zero order diffraction provides the laser output while the first order is reflected back onto the grating by a prism (which is used instead of a mirror to simplify

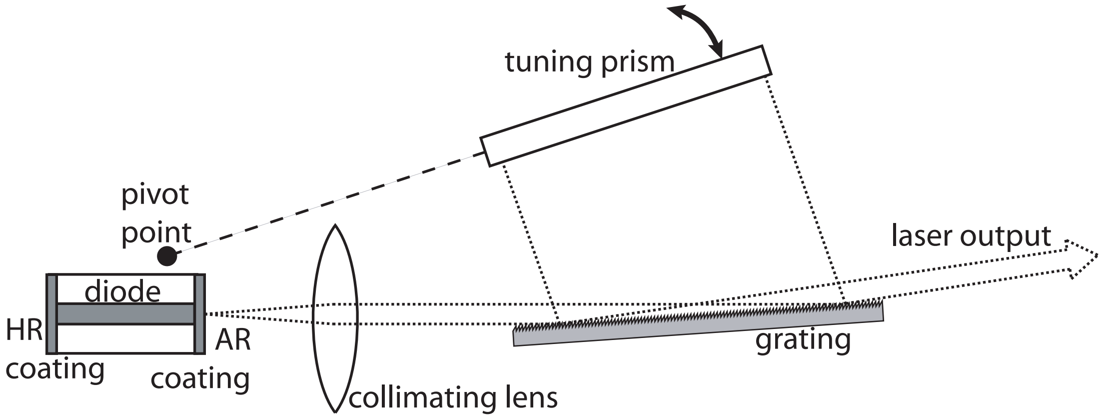

Figure 2.4: Schematic for a 6000 Vortex Series tunable diode laser [2]

laser alignment), and some small fraction returns to the antireflection-coated diode to be amplified. Largely mode-hop free tuning is achieved by carefully selecting the rotation point of the tuning prism. The prism angle is selected by varying the voltage across a piezoelectric actuator (piezo), with higher piezo voltage corresponding to longer wavelength. The piezo voltage is changed either by turning a knob on the laser controller or by applying a voltage to the BNC connector on the back of the laser controller. The latter method allows for a continuous sweep of the laser frequency and for the application of feedback to servo-lock the laser color [2]. Although the voltage can be varied between 0 V and 117 V, the piezo can be locked stably only between 50 V and 80 V. The laser color can also be tuned by varying the current to the diode, although this also reduces the output power. These lasers typically have a tuning range of 140 GHz, a line width of less than 500 kHz, and an output power of 50 mW [2].

2.2 Vacuum Systems

2.2.1 High Vacuum Systems

The atomic beam experiments described in chapters 3, 4 and 5 are performed in vacuum chambers at pressures on the order of 10^{-6} torr. The vacuum chambers are constructed of aluminum cylinders with removable flanges sealed to the chamber with O-rings. These flanges can accommodate electrical feedthroughs of various types, cooling water feedthroughs, vacuum gauges and glass or quartz windows which allow laser light into the interaction region. Plexiglass windows are mounted to the top of the chamber, allowing visual inspection of the system while in operation.

To achieve the desired pressure, the chamber is pumped to less than a hundred millitorr by a mechanical roughing pump. Then, the chamber is isolated from the roughing pump, and the gate valve separating the chamber from the diffusion pump is opened. The diffusion pump heats silicone-based oil, creating jets of downward moving vapor which force any gasses they encounter to the bottom of the pump where the oil condenses and the gasses are evacuated by the roughing pump [59]. A water-cooled baffle between the pump and chamber limits the infiltration of pump oil into the chamber. The diffusion pump is water-cooled, but should the cooling water stop flowing, the pump oil will stop condensing at the bottom of the pump and instead fill the chamber. Overheating can also damage the pump oil requiring the cleaning of the pump and replacement of the oil. To prevent this,F the pump's power is interlocked to a temperature sensor. An additional interlock prevents the diffusion pump from heating when the exhaust line pressure is greater than 100 millitorr which can similarly tax the pump oil or spread the oil though out the vacuum chamber.

The vacuum chamber used for the lithium experiments in chapters 3 and 4 and shown in figure 2.5 consists of a vertically oriented cylinder with a diameter of approximately twenty inches and a height of approximately twelve inches. The vacuum is maintained by a Dresser Vacuum DPD 6-1800 diffusion pump.

The chamber shown in figure 2.6 and used for the potassium beam experiment discussed in chapter 5 is a horizontal cylinder with an approximate diameter of eleven inches and a length of seventeen inches. This chamber has considerably less volume and therefore uses the smaller CVC-PMCS-2C diffusion pump. Both diffusion pumps are backed by the same Welch Duo Seal mechanical pump. The distinguishing feature of this system is the cold

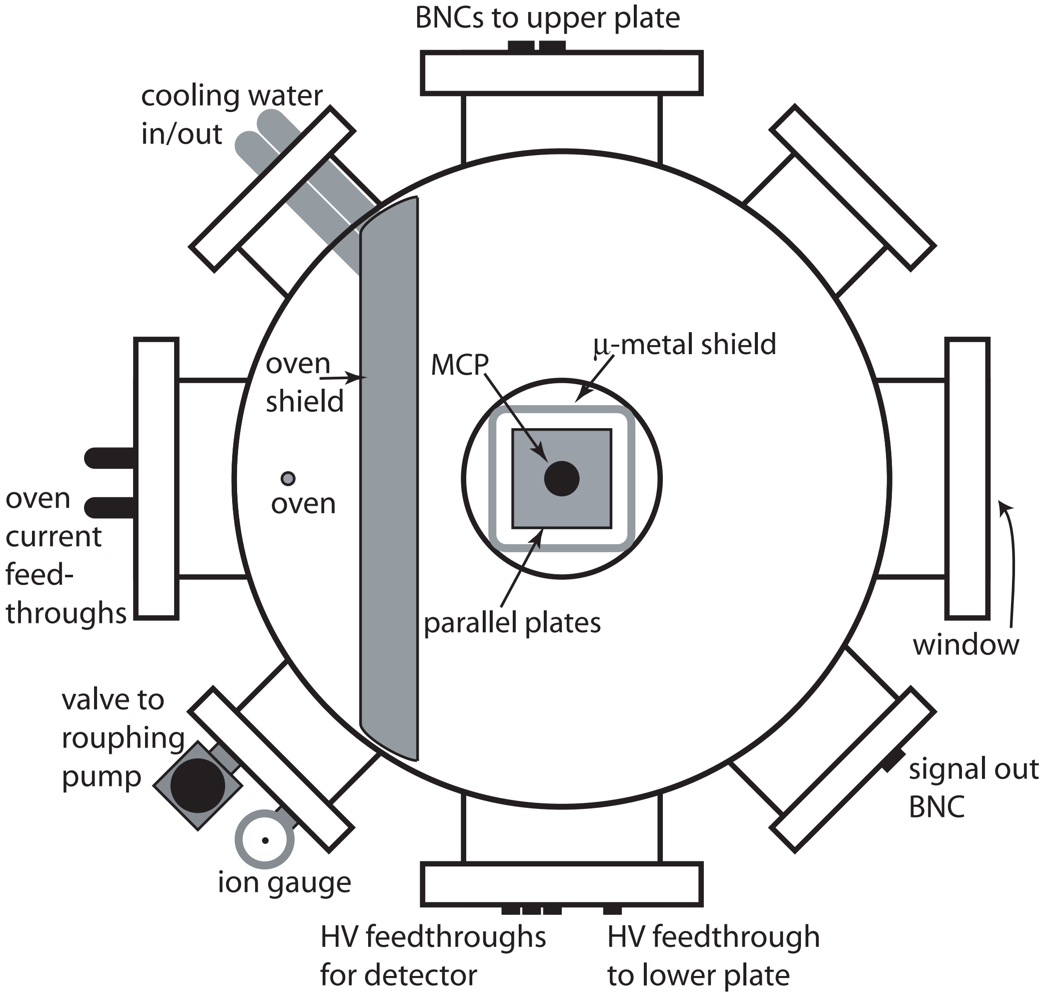

Figure 2.5: Schematic of the vacuum chamber used for the experiments in chapters 3 and 4.

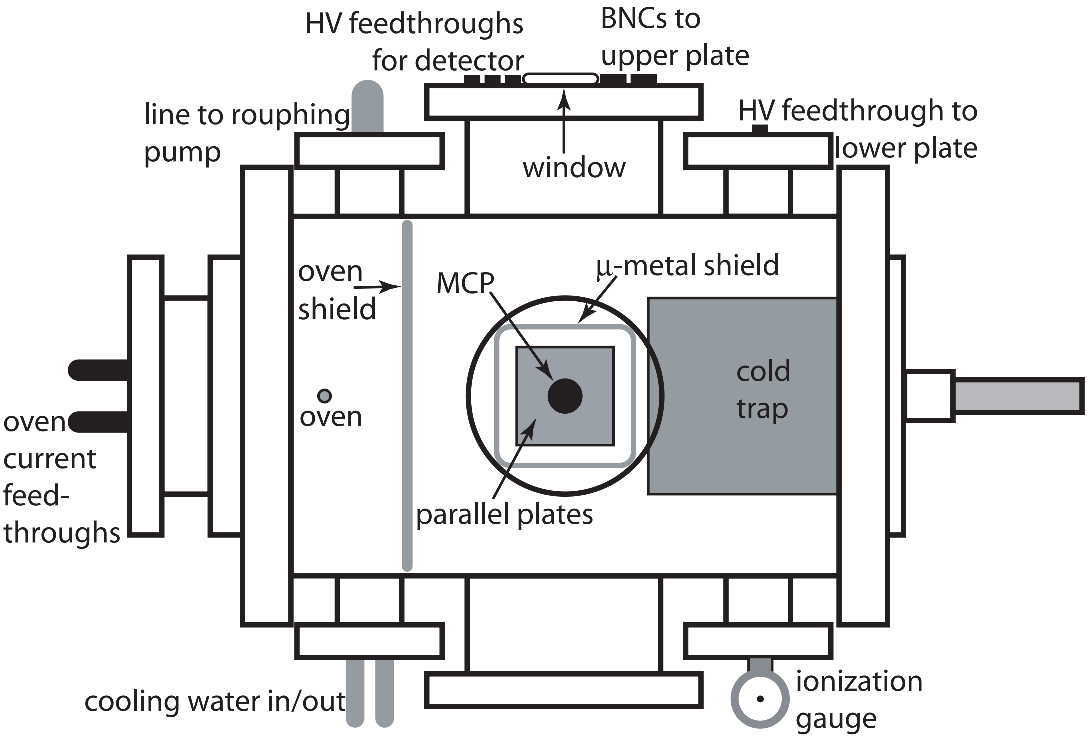

Figure 2.6: Schematic of the vacuum chamber used for the experiment in chapter 5.

trap. When this brass can is filled with liquid nitrogen, gases in the chamber condense on its exterior and the pressure is reduced. The cold trap also improves the collimation of the atomic beam by catching the majority of the potassium atoms after they pass though the interaction region and preventing them from bouncing off the walls of the chamber and reentering the interaction region with random velocities.

2.2.2 Ultra High Vacuum System

The experiments described in chapter 6 are performed in a stainless steel spherical cube chamber from Kimball Physics, Inc. (item number MCF600-SS200408) at pressures below 5×10^{-9} torr. The main body of the chamber is a hollow sphere with an outer diameter of 6.5 inches and an inner diameter of 4.8 inches intersected by two vertical 6 inch CF sealed glass windows. Eight 1 1/3 inch windows, one 2 3/4 inch window, a four-way cross and two six-way crosses are attached to the main chamber as shown in figure 2.7. Windows, a nude

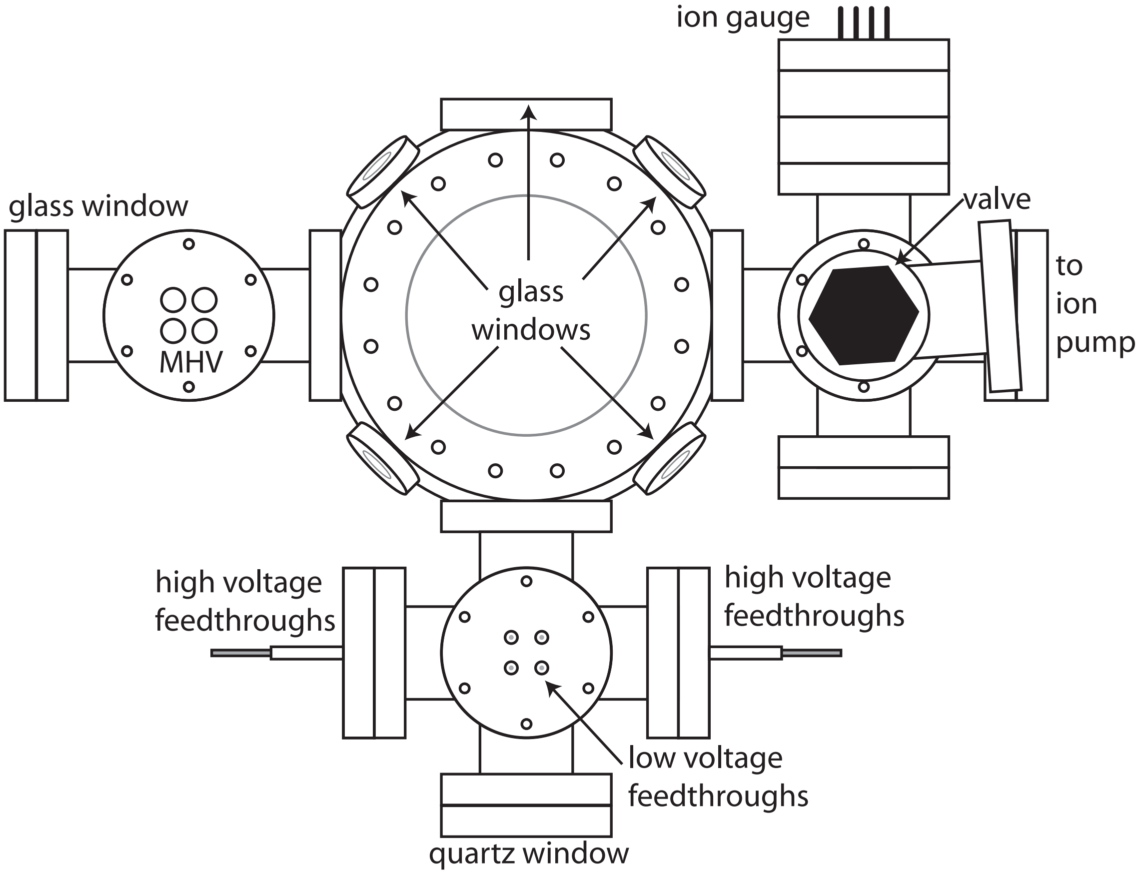

Figure 2.7: Schematic of the vacuum chamber used for the experiment in chapter 6.

ion gauge, high and low voltage feedthroughs, a valve to attach a roughing pump and the ion pump are attached to the crosses by CF seals.

The vacuum is achieved by first rough pumping the chamber with a turbo pump backed by a sorption pump. Once the pressure is below 10^{-4} torr, the TiTan 20S ion pump from Gamma Vacuum may be turned on, but it is desirable to rough to lower pressures because this speeds the pump down and extends the life of the ion pump. In the ion pump, electrons expelled from the high voltage element are pulled into an array of anode tubes where they are trapped by the 1200 gauss magnetic field provided by permanent magnets surrounding the pump body. Gasses which enter the anode tubes are ionized by the electron plasma, and the high electric field accelerates the ions toward the cathode plate. After impacting the cathode, the ion undergoes one of two reactions as it ejects material from the cathode. Some ions undergo chemical reactions with the cathode materials forming inert solids. Other ions bounce off the cathode with enough energy to embed in other pump surfaces [60]. Rubidium can adversely affect the performance of the ion pump by building up on its surface, creating an electrical path between the anode and cathode. If this build up effects pump performance, baking the ion pump at between 150 ^{0}C and 200 ^{0}C for 8 hours into the roughing pump should remove the buildup [61]. After the chamber has been exposed to atmospheric pressure, it is necessary remove water and other gases from the walls of the chamber. To this end, the chamber is heated to between 100 ^{0}C to 150 ^{0}C for 24 to 48 hours. It is best to use the turbo pump during the beginning of this baking process, but as long the pressure in the chamber remains below 10^{-5} torr the ion pump can be used alone [62].

2.2.3 Gauges

The pressures in all the vacuum systems are measured by two types of gauges: thermocouple and Bayard-Alpert ionization gauges. Varian senTorr gauge controllers are used to monitor both types of gauges. A thermocouple gauge measures pressures from 10^{-3} torr to

10^2 torr by monitoring the temperature of a filament. At higher pressures, gasses conduct heat away from the filament more efficiently, lowering its temperature. These gauges are used to measure the pressure while the chambers are being roughed, as well as the pressure of the fore-line of the high vacuum systems described in section 2.2.1.

Bayard-Alpert ionization gauges work on a similar principle to the ion pump described in section 2.2.2. A hot 30 V filament ejects electrons which are accelerated to the grid which is held at about 180 V. As they travel, they ionize a fraction of the gases they encounter. The resulting ions are accelerated away from the filament to the relatively negatively charged (grounded) central ion collection wire. Thus, the current at the collection wire is proportional to the pressure for a given grid voltage and background gas composition. We use two types of Varian ionization gauges: nude and glass-enclosed. Glass-enclosed gauges sit outside the main chamber in a glass bell and are attached to the main chamber by a glass tube, while nude gauges sit inside the chamber. The glass-enclosed ion gauges, used to monitor the high vacuum systems described in section 2.2.1, measure pressures between 10^{-10} torr to 10^{-3} while the nude gauge, used to monitor the UHV system described in section 2.2.2, can measure pressures as low as 2×10^{-11} torr. The nude ionization gauge in the UHV system cannot be left on while data is being collected because the filament electrons destroy the MOT. The ion pump can also be used to monitor the pressure in the chamber by measuring the current at the cathode. The ion pump controller has a setting that performs this calculation, but this is not as accurate as the ionization gauge.

2.3 Atomic Beams

The experiments described in chapters 3 through 5 take place in thermal atomic beams of lithium and potassium. The first step to creating an atomic beam is constructing the oven from a 6 inch long, 3/8 inch diameter steel tube with a wall thickness of approximately .006 inches. One end of the tube is crimped and a small (.4 mm to 1 mm diameter) hole is drilled in the center of the tube. To prepare the alkali metal solid, the mineral oil in which the sample is stored to prevent oxidation must be removed, typically by rinsing the metal in toluene. Once cleaned, the metal is stuffed into the oven until the tube is filled to just below the hole. Any metal that becomes stuck in the hole is cleared and the top of the oven is crimped before the oven is clamped to its mount on a vacuum flange. The oven is aligned so that the hole points directly towards the interaction region.

Once the system is under vacuum, alternating current through the oven is slowly increased to a maximum of between fifteen and sixty amps. The current is supplied by a series of transformers that step down the standard 120 VAC, 60 Hz to approximately 6.8 VAC resulting in an increase in the current by a factor of about 18. A Variac AC variable transformer controls the current. Large high-current feedthroughs and thick copper wire connecting the transformers to the feedthroughs ensure that the majority of the power is dissipated in the oven despite its small resistance of about 0.1 Ω. This results in the resistive heating of the oven which causes the alkali metal inside to vaporize. The vapor effuses out of the hole in the oven forming a wide cone. The atoms are collimated by a quarter centimeter tall, centimeter wide hole in the water-cooled copper shield such that only the small part of the cone which is traveling directly towards the interaction region to pass through. The shield contains the majority of the alkali metal and any other debris emitted by the oven to a small area, keeping the rest of the chamber relatively clean. The beam is further collimated as it enters the interaction region by a five millimeter teflon slit. These atomic beams typically have densities of 10^7 to 10^8 atoms/cm^3 [63]. The atoms in the beam have a distribution of velocities given by

$$\Phi(v) = \frac{Nv^3}{2}\left(\frac{m}{kT}\right)^2 e^{-\frac{mv^2}{2kT}} \tag{2.1}$$

which is normalized so $\int \Phi(v)dv = N$, where m is the atomic mass, k is Boltzmann's constant, T is the temperature of the oven producing the beam, and N is the number of atoms per unit volume [64–67]. Typical temperatures range between 400 K and 800 K with typical velocities on the order of 1 mm/μs.

The interaction region is defined by a pair of parallel square metal plates, 7.5 cm on a side. These plates are used to apply electric fields to the atoms which control the atomic energy spacing via the Stark effect and ionize the atoms. While the bottom plate is solid, a 25 mm by 2 mm slit parallel to the atomic beam in the top plate allows charged particles to be pushed out of the interaction region to the detector above. To improve the electric field homogeneity under the slit, a fine wire mesh is fixed to the plate. To minimize the magnetic field, a μ-metal shield surrounds the interaction region resulting in a small magnetic field which, according to our experiments, is much less than 100 mG.

2.4 Magneto-Optical Trap

A magneto-optical trap (MOT) provides the atomic source for the experiments described in chapter 6 by combining a magnetic field gradient and three orthogonal pairs of counter-propagating laser beams to cool and trap rubidium atoms. A MOT is an excellent source of cold atoms because of its ease of operation and relatively low cost. This type of trap does not require precise laser beam intensity balancing, nor a high degree of polarization, both of which result in robust cooling and trapping. The requisite magnetic field can be generated by air or water cooled coils, while relatively inexpensive diode lasers are available to drive the trapping transition in rubidium and most other alkali metals [3]. The vapor loading method used allows for a compact room temperature vacuum system, further limiting costs [68]. Since first being demonstrated in 1987 [69], the MOT technique has been developed and refined resulting in a large volume of literature on the subject. Therefore, the discussion here will be limited to a brief overview of the theory of operation and a description of our experimental implementation.

2.4.1 Theory of Operation

For simplicity, consider a stationary two state atom with a spin S=0 ground state and a spin S=1 excited state in a one-dimensional weak inhomogeneous magnetic field. Assuming the magnetic field in the z-direction varies linearly so $B_z(z) = Mz$ where M is a constant, the Zeeman effect will break the spin degeneracy, splitting the excited state by an energy $\Delta E = \mu m_s B = \mu m_s M z$ resulting in the position dependent energies shown in figure 2.8. Consider a beam of σ_- light propagating in the $-\hat{z}$ direction and a counter-propagating beam of σ_+ light. If both beams are red detuned from the zero-field resonance, then an atom with a position $z > 0$ will preferentially absorb photons from the σ_- beam because the $m_s = -1$ state is closer to resonance with the light. Conversely, for an atom at $z < 0$, the $m_s = 1$ state is shifted down, and the atom will therefore preferentially absorb photons from the σ_- beam. As long as the light beams are weak, the atom scatters any absorbed photons in random directions, resulting in a net force on the atom, pushing it toward the origin. The red detuning from resonance also provides velocity damping similar to that seen in optical molasses [70]. Thus, cooling and confinement are achieved simultaneously. It is straight forward to extend this method to three dimensions with the addition of counter-propagating beams and magnetic field gradients along the y and x axes. The field gradients are provided by a "spherical quadrupole" magnetic field generated by a pair of anti-Helmholtz coils as shown in figure 2.9. The motion of a trapped atom is that of a damped harmonic oscillator, although in this case the motion is strongly overdamped [3, 69].

2.4.2 Implementation

The MOT is created in the vacuum chamber described in section 2.2.2. Rubidium vapor is produced by resistively heating metal getters containing anhydrous rubidium salts of chromic acid and a reducing agent. Heating the getters initiates the reduction reaction which liberates the rubidium from the chromate, and the rubidium evaporates. The quantity of rubidium dispensed increases with the applied current [71].

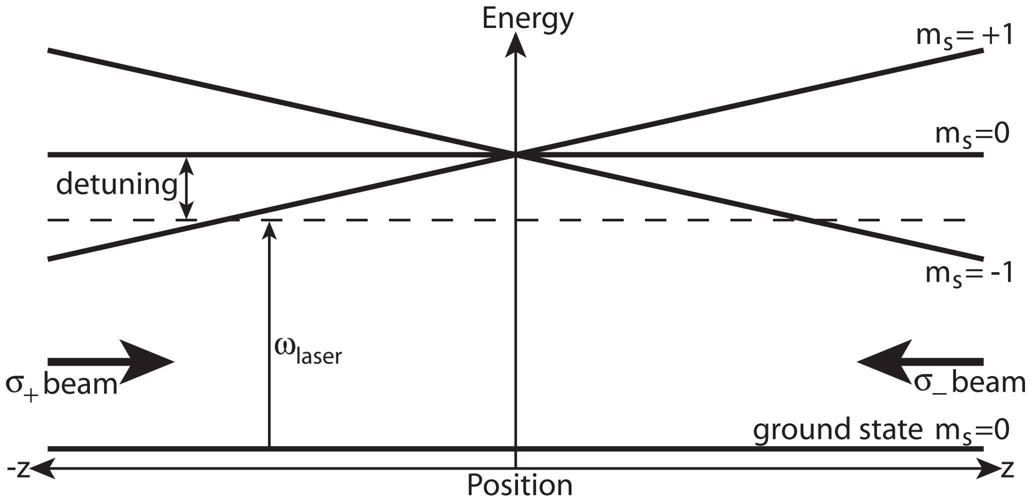

Figure 2.8: Schematic for a 1-D MOT. The dashed line represents the energy of the laser seen by a stationary atom. The Zeeman effect splits the excited state creating a position-dependent transition probability due to the inhomogeneous magnetic field. Atoms to the right of the origin are more likely to scatter photons from the σ_- beam while atoms to the left of the origin are more likely to scatter photons from the σ_+ beam. Thus, atoms are pushed toward the origin [3].

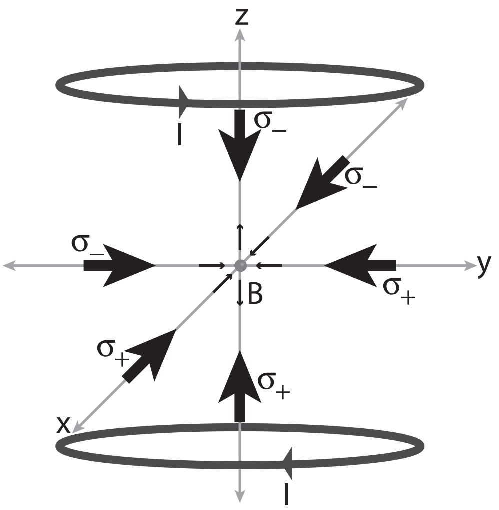

Figure 2.9: Schematic for a 3-D MOT. The small arrows on the axes show the direction of the magnetic field along the axes. The large arrows show the laser beam directions and are labeled with their polarizations. The rings represent the anti-Helmholtz coils used to produce the magnetic field. The current direction is marked by arrows and labeled I.

Two field coils provide the requisite magnetic field gradient. Each coil consists of 114 turns of Polyurethane-Nylon coated copper wire wrapped around a fifteen-centimeter diameter aluminum and plastic frame. To prevent current from being induced in the aluminum when the current is switched on or off, a wedge of plastic completes the circular aluminum frame. An enclosed chamber in the frames allows chilled water to cool the coils. The coils fit snugly around the vacuum chamber's six-inch windows and when mounted the have an inner axial separation of seven centimeters. The coils are connected in series such that they carry current in opposite directions. To estimate the magnetic field near the midpoint of coils, consider two coaxial rings of current with radii R separated by a distance $2A$. Then the magnetic field close to the origin is approximated by

$$B_z = \sum_n b_n B_{zn} \approx b_1 z + b_3 \left(z^3 - \frac{3z\rho^2}{2} \right), \tag{2.2}$$

$$B_\rho = \sum_n b_n B_{\rho n} \approx b_1 - \frac{\rho}{2} + b_3 \left(-\frac{3\rho z^2}{2} + \frac{\rho^2 z}{8} \right), \tag{2.3}$$

$$b_1 = \frac{3\mu_0 I A R^2}{(R^2 + A^2)^{5/2}}, \tag{2.4}$$

$$b_3 = \frac{5(4A^2 - 3R^2)}{6(A^2 + R^2)^2} \times b_1, \tag{2.5}$$

where z is taken to be along the coils' axis and origin is taken to be the midpoint of the pair [72, 73]. In our case $R \approx 9$ cm and $A \approx 5$ cm, so $b_1 \gg b_3$ and the field varies linearly in all directions near the zero in the field at the origin. The magnetic field gradients are

$$\frac{\partial B}{\partial z} = b_1 = -2\frac{\partial B}{\partial \rho}, \tag{2.6}$$

so the field gradient along the coils axis is twice that in the radial direction [72, 73]. Typically, ten amps of current through the coils provide our magnetic field resulting in an on axis field gradient of approximately 15 Gauss/cm.

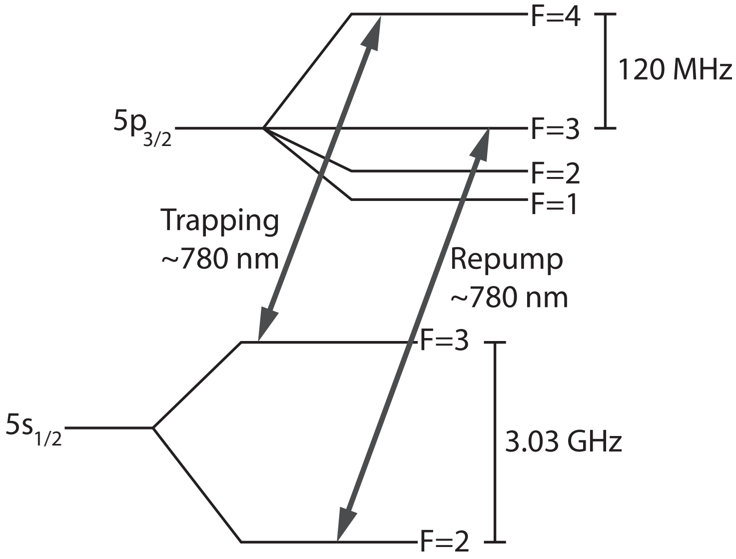

Figure 2.10: Energy diagram for the ground and first excited states of ^{85}Rb. The trapping $5s_{1/2}, F = 3 \longrightarrow 5p_{3/2}, F = 4$ and repump, $5s_{1/2}, F = 2 \longrightarrow 5p_{3/2}, F = 3$ transitions are driven by two 780 nm diode lasers.

The atomic structure of ^{85}Rb is more complex than that described in the simple model of section 2.4.1, but the analogy is straightforward. The ground state of the outer electron is the $5s_{1/2}$ state, while the first excited state, $5p_{3/2}$, is split onto two fine structure states $J = 1/2$ and $J = 3/2$. The nuclear spin, $\vec{I}$, couples with the electron's total angular momentum, $\vec{J}$, giving rise to hyperfine structure such that the total angular momentum $\vec{F}$ is given by $\vec{F} = \vec{I} + \vec{J}$. The resulting hyperfine splitting has the form $E_{hfs} = A\vec{I} \cdot \vec{J}$ where A is an experimentally determined constant. As shown in figure 2.10, since $I = 5/2$ in ^{85}Rb, the ground state is broken into two hyperfine states, $F = 2, 3$ with a splitting of about 3.03 GHz. The first excited state is split into four hyperfine states, $F = 1, 2, 3, 4$, with average splittings of 100 MHz [72]. In an ideal system, selection rules would dictate that excited atoms decay only to their initial state, and therefore, no atoms would be lost from the trap. The relevant selection rule in this case requires $\Delta F = 0, \pm 1$, making the $5s_{1/2}$, $F = 3$ to $5p_{3/2}$, $F = 4$ transition appealing as the excited atoms are forbidden from decaying back into the $5s_{1/2}$, $F = 2$ state which is inaccessible to the laser. Unfortunately, the trapping laser drives some population to the $5p_{3/2}$, $F = 3$ state due to its proximity to the $5p_{3/2}$, $F = 4$ state (about 120 MHz). From the $5p_{3/2}$, $F = 3$ state, an atom can decay into the $5s_{1/2}$, $F = 2$ state, and hence, it is lost from the trap. To counter this trap-destroying process, a second "repump" laser is tuned to the $5s_{1/2}$, $F = 2$ to $5p_{3/2}$, $F = 3$, thus exciting the atoms which decay into the "dark" state back into a state from which they can reenter the trapping cycle [72, 74].

Two of the commercial diode lasers described in section 2.1.3 drive the trapping and repump transitions. Both lasers' frequencies are set by servo-locking to Doppler-free saturated absorbtion spectra. The saturated absorbtion spectrum is obtained via a pump-probe measurement. A pump beam with enough intensity to saturate the transition of interest (about four percent of the laser light in our application) is directed through a room temperature glass cell filled with rubidium vapor, and a fraction (about five percent) of the pump beam is then reflected back through the path of the pump as a probe. Consider the case where the laser is detuned a small amount δ to the red of the Doppler-free frequency, ω_0. If we take the pump light to be traveling in the $-\hat{x}$ direction, atoms with velocity components $v_x = \delta c/\omega_0$ absorb light from the pump beam, while the probe beam will excite a different set of atoms with $v_x = -\delta c/\omega_0$. If there were only one possible transition, the probe beam attenuation would trace out the Doppler broadened resonance at all frequencies except ω_0. Only atoms that are stationary in the $\hat{x}$ direction can absorb light with a frequency ω_0, but they will be excited by both the pump and probe beams. Since the pump beam saturates the transition, there are fewer stationary atoms in the ground state for the probe beam to excite, causing the intensity of the transmitted probe to increase. The presence of additional transitions leads to multiple peaks in the transmitted intensity of the probe. These "crossover" resonances occur between true resonances where an atom has the correct velocity components to absorb either a red-shifted photon from one beam and go to the lower lying state or to absorb a blue-shifted photon from the other beam and go to the higher lying state. The features of the crossover resonances depend on the states involved

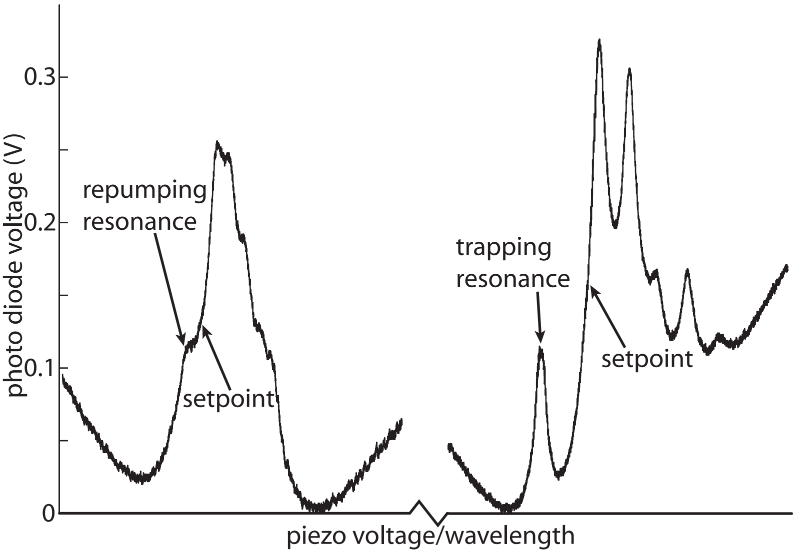

Figure 2.11: Plots of the saturated absorbtion spectrum near the repumping and trapping resonances. The larger nearby peaks are the "crossover" resonances. The lasers are locked to the sides of the crossover peaks near the real resonances.

and the geometry of the beam overlap [75].

The transmitted intensity of the probe beam also varies with the total laser power. In order to obtain a more stable spectrum, we monitor the intensity of the pump beam as well as the probe on photodiodes. The photodiodes are tied together in a push-pull configuration so that when the intensity on both diodes increases, the signal level remains unchanged. The spectrum is generated by sweeping the piezo voltage with a triangle or sine wave. The saturated absorbtion spectrum near the trapping and repump transitions are shown in figure 2.11. The servo-loop locks the laser to the side of a resonance. The frequency set point is selected by adding an offset voltage to the photodiode signal so that the desired point is at zero volts. When locked, the saturated absorption signal is compared to zero volts and the resulting error signal is feedback to the piezo, thus locking the laser.

In order to lock the trapping laser with the desired red detuning, an acousto-optic modulator (AOM) from IntraAction Corp. (Model AOP-402AF3) is added to the part of the beam used to generate the saturated absorbtion spectrum. The AOM uses radio frequency sound waves in a transparent bulk material to diffract light passing through the material. The light passing though the AOM is doppler-shifted by an amount equal to the drive frequency, so $\omega_{out} = \omega_{in} \pm \omega_{rf}$ [76]. Driving the AOM at 36 MHz, the first order blue shift is used to lock the laser to the side of the crossover near the $5s_{1/2}$, $F = 3$ to $5p_{3/2}$, $F = 4$ resonance, as shown in figure 2.11. The repump laser is locked to the side of the of the crossover peak just above the $5s_{1/2}$, $F = 2$ to $5p_{3/2}$, $F = 3$ resonance.

The main trapping and repumping beams are enlarged prior to being sent into the vacuum chamber. The trapping beam is expanded to a diameter of about 8 mm by a telescope comprised of a −100 mm lens and a 1000 mm lens. Because the collimation of the repump beam does not affect the MOT, a single −200 mm lens is used to expand the beam resulting in a diameter of about 8 mm when the beam first enters the chamber. The repump beam passes through the chamber twice, first through the 6 inch vertical windows and then diagonally through two of the 1 1/3 inch windows as show in figure 2.12. After expansion, the trapping light is divided into three approximately equal beams, and each is given the correct polarization by its own $\lambda/4$ wave plate just before entering the chamber. One beam passes horizontally through the 6 inch windows while the other two cross the chamber through two pairs of 1 1/3 inch windows. Each beam passes though another $\lambda/4$ wave plate before being retro-reflected back along the same path. The retro-reflected light is prevented from feeding back into the laser by a Faraday isolator positioned just in front of the laser.

As in the beam experiments, applied electric fields are used to control atomic interactions and ionization. These fields are generated by applying voltages on two pairs of vertical stainless steel rods rather than parallel plates in order to allow better optical access to the MOT. The rods in each pair are separated by 2.29 cm while the pairs are 1.52 cm apart. The four vertical rods are positioned in the center of the main vacuum chamber with the axis of separation between the pairs parallel to the 6 inch windows. The detector is held about 5 cm from the nearest pair of rods in front of the 2 3/4 in flange connected to the four-way cross.

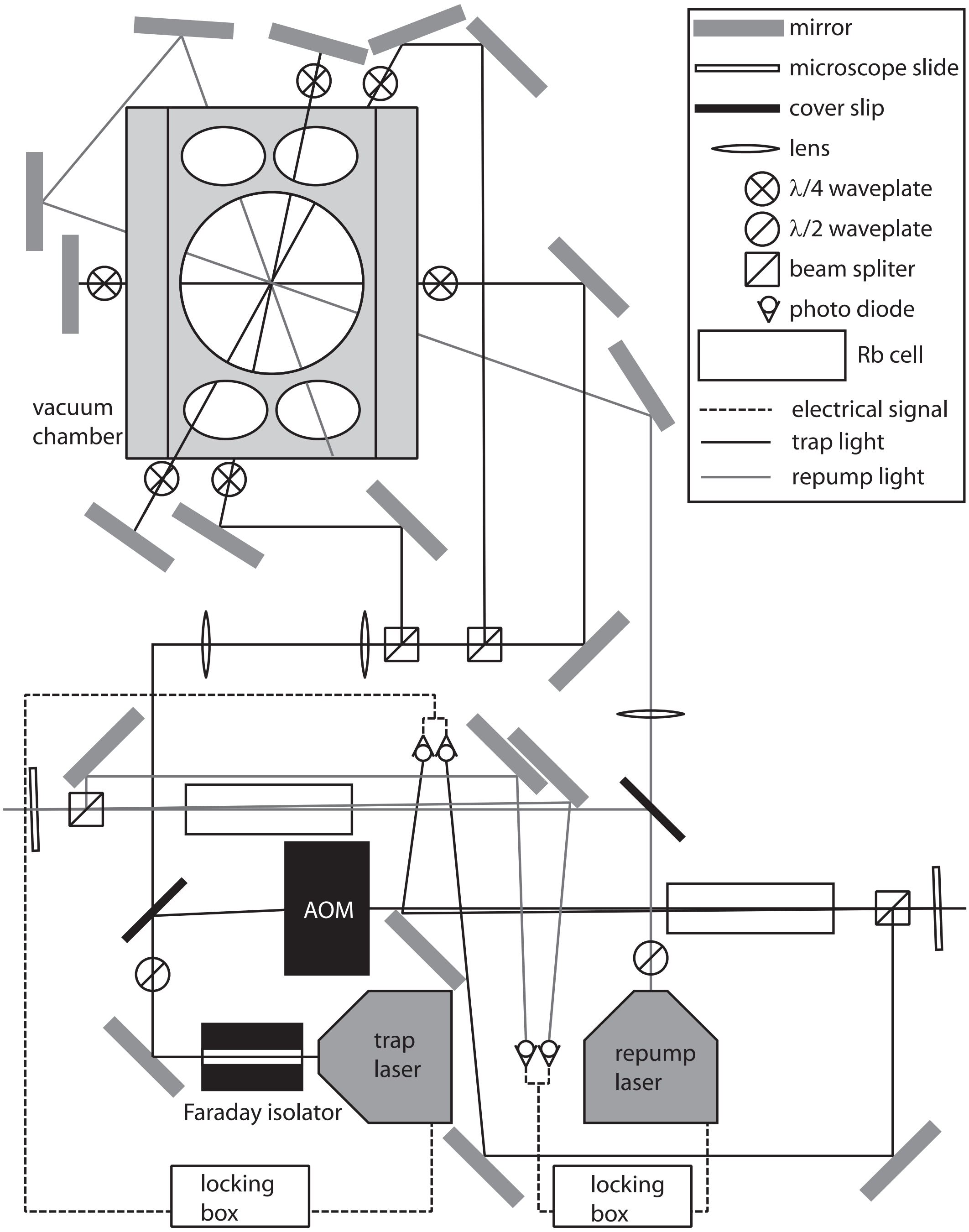

Figure 2.12: Schematic of the lasers' paths for the MOT.

2.4.3 Characterization

The temperature and density of the Rydberg atoms excited in the MOT affect the interactions between the atoms. We begin by determining the size of the MOT. Ultra-fast (100 fs) laser pulses from the Ti:Al_2O_3 (Ti:sapphire or Ti:sapphs) laser system described in other recent dissertations [63, 77, 78] are expanded in the horizontal direction by a −300 mm focal length lens and are then focused into the MOT by a 300 mm cylindrical lens forming a horizontal line across the MOT. The Ti:sapphs' bandwidth is broad enough to include the transition from the ground state ($5s_{1/2}$) to the $5p_{3/2}$ states at 780 nm and the transition from the $5p_{3/2}$ states to the $5d$ states at 776 nm. The ionization threshold is less than one photon energy from the $5d$ states (specifically the ionization threshold is one 1252 nm photon from the $5d$ states) so the ultra-fast pulses very efficiently ionize rubidium atoms from both the ground and trapped states by two and three photon ionization. The resulting ions are pushed to the multi-channel plate charged particle detector by 167 V applied to the rods farthest from the detector. Decreasing the repetition rate of the Ti:sapphs laser to .1 Hz so that the MOT returns to full size before the next laser shot, and varying the vertical position of the Ti:sapphs' light, we record the ionization from different slices of the MOT. Integrating the ionization signal for each slice, we find the MOT profile shown in figure 2.13(b). Fitting a Gaussian to the integrated signal gives a MOT diameter of .4 mm. On a day to day basis we monitor the MOT size on a CCD camera. Looking at a single camera line at the center of the MOT, we determine the width of the MOT by fitting a Gaussian to the signal where the conversion factor for the time axis is 0.7 mm/μs. It should be noted that this conversion factor depends on the position and focusing of the camera.

To determine the temperature of the atoms in the MOT, Pockels cells and polarizers are placed in the trapping and repump beams. When a 4.727 kV pulse is applied to the Pockels cells, the polarization of the light from the diode lasers is rotated 90^0 and is blocked by the polarizer as in the Q-switch described in section 2.1.1. We note that, in order to eliminate unwanted light forces on the atoms, the beam intensity when switched off must

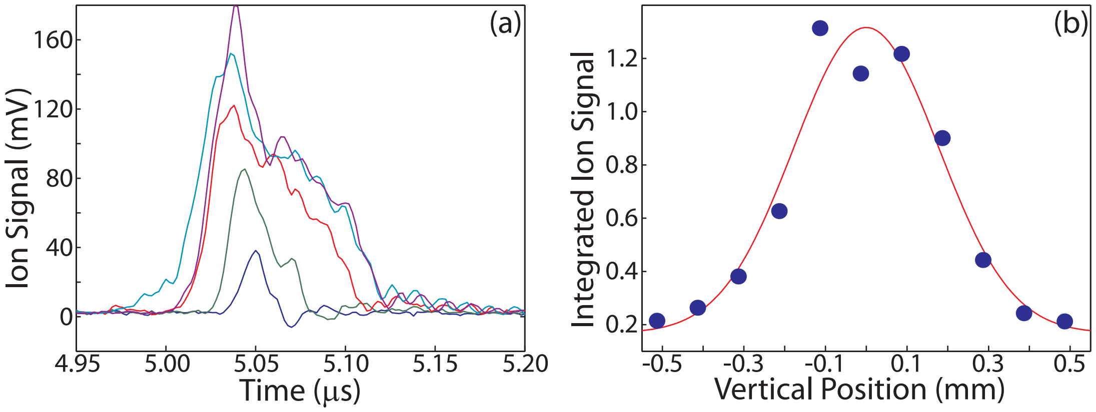

Figure 2.13: (a) Plot of ionization signal from different slices of the MOT each separated by .1 mm. The asymmetry in the time of flight signal indicates that the ions were undergoing coulomb repulsion. Using a lower Ti:sapph intensity generally reduces this asymmetry. (b) Plot of the MOT profile given by the integrated signal (blue) from (a) is fit with a Gaussian (red). The fit indicates a MOT diameter of .42 mm.

be $< 0.1\%$ of the intensity when the MOT is operating. Without the trapping light field, the cloud of cold atoms falls due to gravity and expands as shown in figure 2.14(c). The rate of the clouds expansion is determined by the atoms temperature. For a temperature T, the velocity distribution in the x direction is

$$\Phi(\upsilon_x) = \sqrt{\frac{m}{2\pi kT}}e^{-\frac{m\upsilon_x^2}{2kT}} \tag{2.7}$$

where k is the Boltzmann constant and m is the mass of the atom. The atom cloud will expand at a rate equal to the full width at half the maximum of the one dimensional velocity distribution, $\upsilon = 23.1\sqrt{T}$. We monitor the expansion of the cloud by ionizing a series of horizontal slices through the cloud using the short pulses from the Ti:sapph laser 4 ms and 8 ms after the trapping and repumping light are switched out of the chamber. The horizontal expansion can be seen directly in the ion time of flight as ions at different positions in the expanding cloud arrive at the detector at different times. This time of flight was calibrated by removing the expanding lens, placing a vertical slit in the laser beam, and recording the ion signal for various horizontal slit positions.

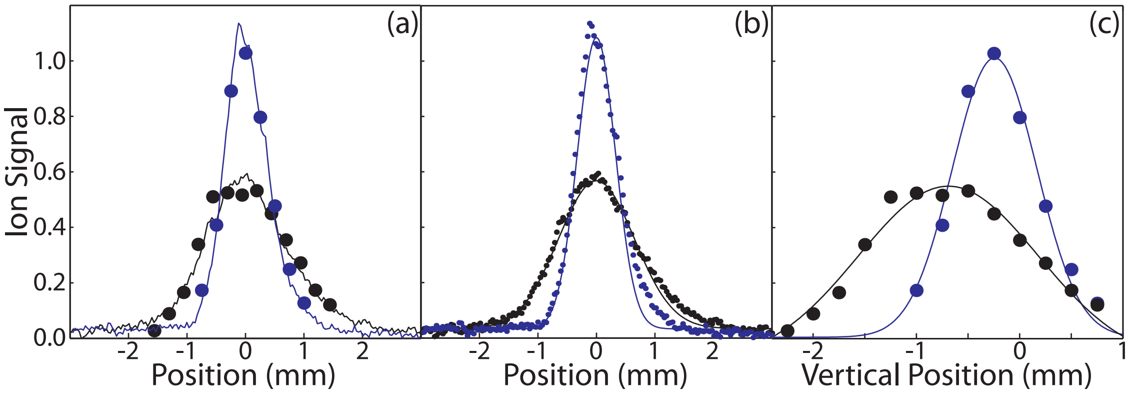

Figure 2.14: (a) Plots of the horizontal (solid lines) and vertical (points) atom distributions following 4 ms (blue) and 8 ms (black) expansions are nearly identical. (b) Plots of the measured expansion (points) of the atom cloud at 4 ms (blue) and 8 ms (black) shows good agreement with the predicted expansion (lines) for a temperature of 67.5 μK. (c) Plot of the atom cloud falling due to gravity. The atoms appear to have an initial downward velocity of 5 cm/s, likely due to the finite turn-off time of the trapping laser.

Integrating over the horizontal time of flight slices reveals the fall and expansion of the atom cloud. We compare the vertical and horizontal expansions in figure 2.14(a) by averaging all of the time of flight scans and centering both the vertical and horizontal peaks at zero. We normalize the horizontal and vertical expansion profiles such that their integrals are one and observe good agreement. The data for both expansion times are consistent with a cloud temperature of 67.5 μK as shown in figure 2.14. The only inconsistency in the data is an apparent initial downward atom velocity of 5 cm/s likely related to the finite turnoff time of the trapping and repumping lasers. We note that the horizontal time of flight measurement provides a single shot temperature determination and can be used to check for temperature variations for different MOT laser and magnetic field conditions.

In an effort to find a way to change the temperature of the atoms in the MOT without destroying the trap, the repump laser intensity was decreased by a factor of 20, and the trapping laser detuning was varied from 32 MHz to 41 MHz (i.e. the AOM frequency) without any significant affect on the temperature as observed using a horizontal time of flight projection of the expanding atoms.

To determine the MOT density, we first attempted to compare the photoionization signal from the MOT with the ionization signal from a known density of background rubidium in the chamber. This method ultimately gave unreliable results likely due to variations in the microchannel plate detector efficiency over its active area and to the large dynamic range in the background rubidium signal sizes between the high densities which we could measure through direct absorption and the low background densities at which the MOT functioned properly. Therefore we used an all optical technique as demonstrated by Han [79]. The number of trapped atoms in the $5p_{3/2}$, $F = 4$ state is proportional to total the amount of light scattered by those atoms. Since the trapping transition is saturated, each atom spends half of its time in the excited state, scattering a photon once every two natural lifetimes. Thus, the scattered power from a single atom is given by

$$P_1 = \frac{hc}{\lambda}\frac{1}{2\tau} = 4.7 \text{ pW} \tag{2.8}$$

where h is Planck's constant, c is the speed of light, λ is the wavelength of the scattered photon (780 nm for the $5p_{3/2}$ to $5s_{1/2}$ transition) and τ is the natural lifetime (27 ns). So the number of atoms in the MOT (N_a) is given by

$$N_a = \frac{P_{total}}{P_1} \tag{2.9}$$

where P_{total} is the total power scattered from the MOT [72]. On a day to day basis, we monitor the amount of light scatted by the MOT with a CCD camera which is attenuated so that even the largest and brightest MOTs do not cause saturation. To calibrate the camera signal, a 75 mm lens images light from the MOT into a power meter (Coherent model LM-2, serial number L927 borrowed from Prof. Gallagher's lab) for a number of different sized atom clouds. The image position is found by searching with a CCD camera with it's lens removed. There is a large amount of scattered light from the windows which tends to overwhelm the light scattered from the MOT making it difficult to locate the MOT's image. To eliminate some of the scattered light, a 1 cm aperture is placed between the lens and the power meter. The apertures block light from the MOT hitting the lens more than $r = 7$ mm from the center of the lens, effectively reducing the area of the lens. In the future, it would be advisable to remove the intermediate aperture once the image has been located to increase the amount of light seen by the power meter. The lens is 160 mm from the image of the MOT, indicating that the lens is $R = 140$ mm from the MOT. We assume that each glass surface (two each on the vacuum window and the lens) has a transmittance $\mathcal{T} = .96$, and therefore the total power radiated by the MOT is

$$P_{total} = \frac{P_{meter}}{\mathcal{T}^4} \frac{4R^2}{r^2}, \tag{2.10}$$

where P_{meter} is the measured power. We determined that the power meter had been calibrated such that it displayed half of the of the actual power. This was determined by measuring total power of the trapping beam with another power meter (Coherent Powermax model PM3Q, serial number 0322A05), attenuating the beam with Schott neutral density filters and measuring the power with the low-power power meter. This miscalibration likely arose from calibrating the meter with its supposed divide by one thousand attenuator in place. We find that this attenuator results in the same attenuation at 780 nm as a NG-1 filter, $\mathcal{T} = 2 \times 10^{-3}$. Taking this factor of two into account, we find typical total powers range up to 45 μW or 9.6×10^6 atoms for large MOTs. However, for small MOTs, like those in which most experiments are preformed, there is insufficient power to obtain an accurate density measurement. Therefore, we calibrate the CCD camera signal to the power meter for large MOTs and use the calibrated CCD to determine the atom density for smaller MOTs.

To compare P_{total} to the camera signal, we record a line from the camera at the center of the MOT. The line is effectively a surface in the x-z plane which has been integrated along z (the depth of the MOT) at $y = 0$. Assuming the MOT has a Gaussian profile (as indicated by figure 2.13(b)), we can write

$$\rho(x,y,z) = \rho_0 e^{-\left(x^2/\Delta x^2 + y^2/\Delta y^2 + z^2/\Delta z^2\right)} \tag{2.11}$$

where ρ_0 is the peak density. Thus, the camera line signal, S_{line}, is proportional to the light scattered by the atoms in the plane at $y = 0$ integrated over z:

$$S_{line}(x, y = 0) = \sqrt{\pi} C \rho_0 \Delta z e^{-x^2/\Delta x^2} \tag{2.12}$$

where C is a constant of proportionality. Assuming the MOT has the same width in all dimensions,

$$\Delta x = \Delta y = \Delta z = \frac{1}{\sqrt{\pi}} \int \frac{S_{line}(x, y = 0)}{S_{line}(x = 0, y = 0)} dx \tag{2.13}$$

where $S_{line}(x = 0, y = 0)$ is the peak value of the camera line signal. The total signal recorded by all lines of the camera is then

$$S_{total} = \Delta x \int S_{line}(x, y = 0) dx = \frac{1}{\sqrt{\pi} S_{line}(x = 0, y = 0)} \left(\int S_{line}(x, y = 0) dx \right)^2 . \tag{2.14}$$

We find that the total camera signal scales linearly with the total power, such that $P_{total} = S_{total} 18$ μW and $N_a = S_{total} 3.7 \times 10^6$ where S_{total} is in V·μs^2.

We excite two Rydberg states and approximate that one fifth of the total number of atoms are excited to each Rydberg state. This is a compromise between the trapping laser saturating its transition during the dye laser pulse, in which case a quarter of the atoms would be excited to each Rydberg state, and the trapping lasers having a negligible effect during the dye laser pulse, in which case one sixth of the atoms would be excited to each Rydberg state. Again we assume that the MOT is spherical and determine the density by dividing the number of Rydberg atoms by the volume, $V = 4\pi w^3/3$, where w is the half width at half max of the camera line signal converted to centimeters by multiplying by .07 cm/μs. Using this method we find that, for typical experiments, our Rydberg atom

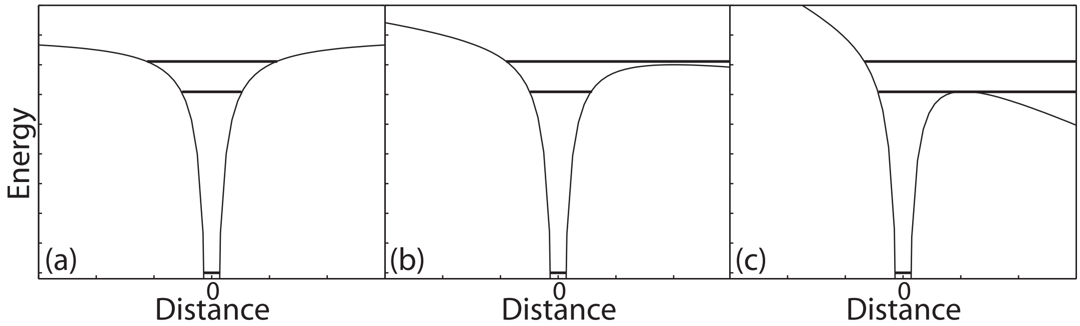

Figure 2.15: Illustration of the atomic $1/r$ potential in the presents of no electric field (a), an electric field E_1 (b) and an electric field $E_2 > E_1$ (c). In (b), the electric field is tipped, allowing the highest lying state to ionize over the barrier. In (c), the barrier is further suppressed allowing the second highest lying state to ionize.

density ranges from 4×10^8 cm^{-3} to 4.5×10^9 cm^{-3}. These densities are a factor of 1.3 less than expected based upon the interactions between the Rydberg atoms as will be discussed in chapter 6. However, this discrepancy is well within the experimental error given the uncertainty in the width of the MOT and the assumption that the MOT is spherical. An error of 0.05 mm in our measurement of the width described above would yield a density increase of 50%.

2.5 Data Acquisition

2.5.1 Selective Field Ionization

The experiments discussed in this dissertation involve creating Rydberg atoms, manipulating them, and then measuring their final state distribution. This is accomplished by state selective ionization and detection of the resulting ions with a charged particle detector [41, 80]. In an applied electric field, the atomic $1/r$ potential is tipped, allowing the electron to escape over the barrier as shown in figure 2.15. Since which states ionize depends on the size of the electric field, applying a slowly rising electric field ramp like that shown in figure 2.16 (b) allows for the sequential ionization of successively lower-lying states. The voltage pulse is applied to the parallel plate or rod pair farthest from the detector. Thus,

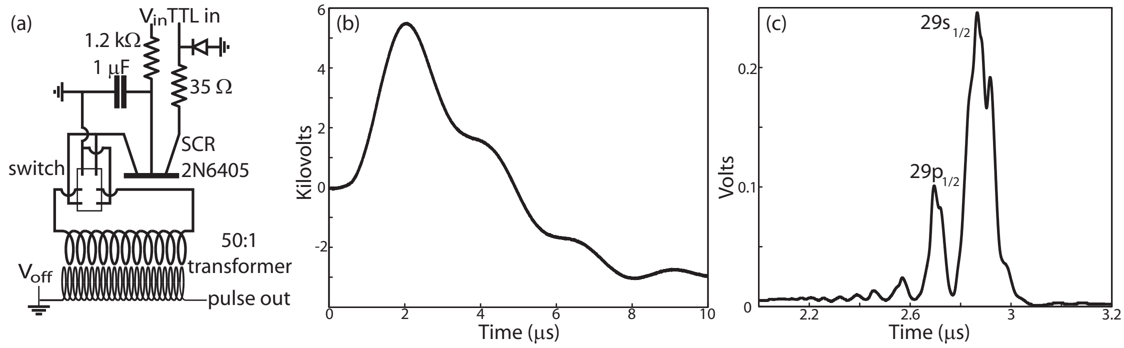

Figure 2.16: (a) Schematic of the circuit that produces field ionization pulse. A 5 μs TTL pulse triggers the SCR allowing current to flow from the capacitor through the transformer. The SCR closes when the voltage pulse rings, reversing its sign. The switch allows for the selection of pulse polarity: positive for ion detection and negative for electrons. For these experiments, ion detection is used. Additional static or slowly varying voltage can be added to the transformer output via V_{off}. The height of the pulse depends on the size of V_{in}. (b) The ramped electric field pulse resulting from the circuit in (a) ionizes lower lying states at later times. (c) Ionization signal as a function of time for potassium Rydberg atoms. The higher lying $29\mathrm{p}_{1/2}$ state is clearly separated from the $29\mathrm{s}_{1/2}$ state.

the pulse accelerates the resulting ions toward the detector.

2.5.2 Micro Channel Plate Detector

The ions strike a detector composed of two matched micro-channel plates (MCP) shown in figure 2.17. Ions hitting the MCP cause cascades of electrons through the micro-channels and out the back of the plate. These electrons are similarly amplified in the second MCP before being collected on a metal plate or phosphor screen. The phosphor screen can be used to observe the spatial distribution of the ions, but for these experiments the resulting voltage is used instead. The time-dependent ionization allows for the differentiation between atomic states as shown in figure 2.16 (c).

2.5.3 Data Collection Programs

Two computer programs are used to record the size of the various ionization peaks. A LabView program written by Jon White is used to retrieve traces of the ionization signal from a Tektronix TDS 3054B oscilloscope and then gate and integrate the various

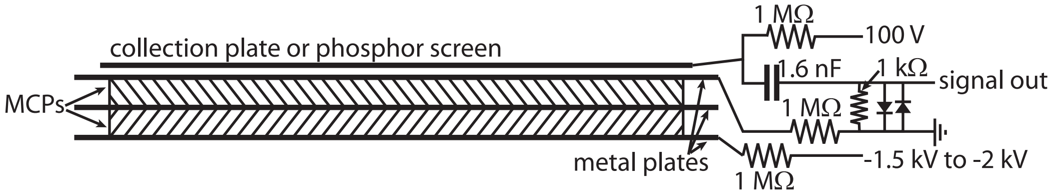

Figure 2.17: Schematic of micro-channel plate detector (MCP) set up to detect ions. The detector is constructed by fixing two micro-channel plates between three thin metal plates which allow voltage to be applied to the micro-channel plates. When detecting electrons, 50 V is applied to the front metal plate to attract the electrons while 1.5 kV to 2 kV is applied to the back metal plate. For detecting ions, −1500 V to −2000 V is applied to the front plate and the back plate is held slightly below ground. Increasing the high voltage results in increased amplification. For matched MCPs the middle plate is allowed to float. The electrons emitted by the MCPs are collected on a metal plate or phosphor screen which is held at 100 V above the voltage on the back plate. When 4 to 5 kV is applied to phosphor screen it will luminesce when struck by electrons from the MCP and can thus be used to observe the spatial distribution of the ions striking the detector.

ionization peaks. Alternatively, Stanford Research Systems SR250 gated integrator and boxcar averagers are used to gate and integrate over the various peaks. The resulting values are read off a Stanford Research Systems SR245 computer interface by Shaper5, a program written by Charlie Conover and revised for these experiments by Hussain Zaidi. In addition to collecting data, this program can control the electronics discussed in the following section through GPIB connections.

2.6 Electronics

These experiments rely on applying various electric fields with precise, reproducible timing. This timing control is provided by a Stanford Research Systems DG535 digital delay/pulse generator. The DG535 provides four variable delays with jitter of five picoseconds relative to the single fixed delay and is triggered on every fourth cycle of the AC line. Triggering from the AC line allows for the excitation of the atoms in the beam experiments when the current through the oven is zero, and thus, the magnetic field in the interaction region, is at a minimum. The DG535 triggers the Nd:YAG's flashlamps and Q-switch, the arbitrary waveform generator that provides electric control fields, the ionization pulse, and the oscilloscope or boxcars for data collection [81]. All of the output delays can be controlled by the data collection program Shaper5.

A Tektronix AWG510 arbitrary waveform generator (AWG) provides the control fields for these experiments. As the name suggests, the AWG can be programmed to produce a wide range of voltage patterns subject to certain restrictions. The output voltages can range between −2 V and 2 V with a maximum peak to peak voltage of 2 V into 50 Ω with a resolution of 1 mV. The sampling frequency of the output waveform can be varied between 50 MHz and 1 GHz, although for these experiments the sampling frequency is always set to 500 kHz or 1 GHz which allows for 2 V rise times of 2 ns or 1 ns respectively. Shaper5 controls the AWG by sending it sequences of waveform patterns. The waveform must be composed of a multiple of 4 points in the range 256 to 4,198,048 points. If longer duration waveforms are desired, the sampling frequency can be reduced, but this increases the voltage rise time [82].

In order to obtain pulses with fast (few nanosecond) rise/fall times and peak to peak voltages greater than 2 V, an AV-141F amplifier was purchased from Avtech Electrosystems Ltd. The amplifier has a 10× gain and an output range of ±5 V into 50 Ω with a 4 ns rise and fall time. With a bandwidth from DC to 75 MHz, the amplifier can reproduce pulses as short as 10 ns [83].

Chapter 3

Pulsed Dynamic Decoupling

A major obstacle to quantum information storage and processing is the loss of quantum coherence due to uncontrolled environmental interactions. The development of methods to prevent or reduce the effects of decoherence is, therefore, an extremely active area of research [11–30]. In the experiments discussed in this chapter, pulsed electric fields dynamically decouple an ensemble of single qubits from their environment. The qubits are encoded in the *np* fine-structure doublets of lithium Rydberg atoms. These experiments show that, although the spin-orbit coupling naturally creates an approximate decoherence-free subspace, periodic dynamic decoupling is a substantially more effective method for preserving coherence. Rydberg atoms provide a good model system for examining decoherence because their large polarizabilities and transition dipole moments make them sensitive to decoherence due to black-body radiation, collisions and small stray electromagnetic fields [41]. The properties of Rydberg atoms that make them sensitive to multiple sources of decoherence, also make them interesting systems for exploring quantum control [84–88] and quantum information processing [42, 43, 45, 47, 89]. For example, fast search algorithms have been used to recover classical information stored in Rydberg wave packets [90]. In addition, the use of binary-collisions [42–44] or many-Rydberg-atom interactions [45] to entangle Rydberg electrons and/or perform quantum logic operations is also being explored [46, 47, 91].

3.1 Single Qubits

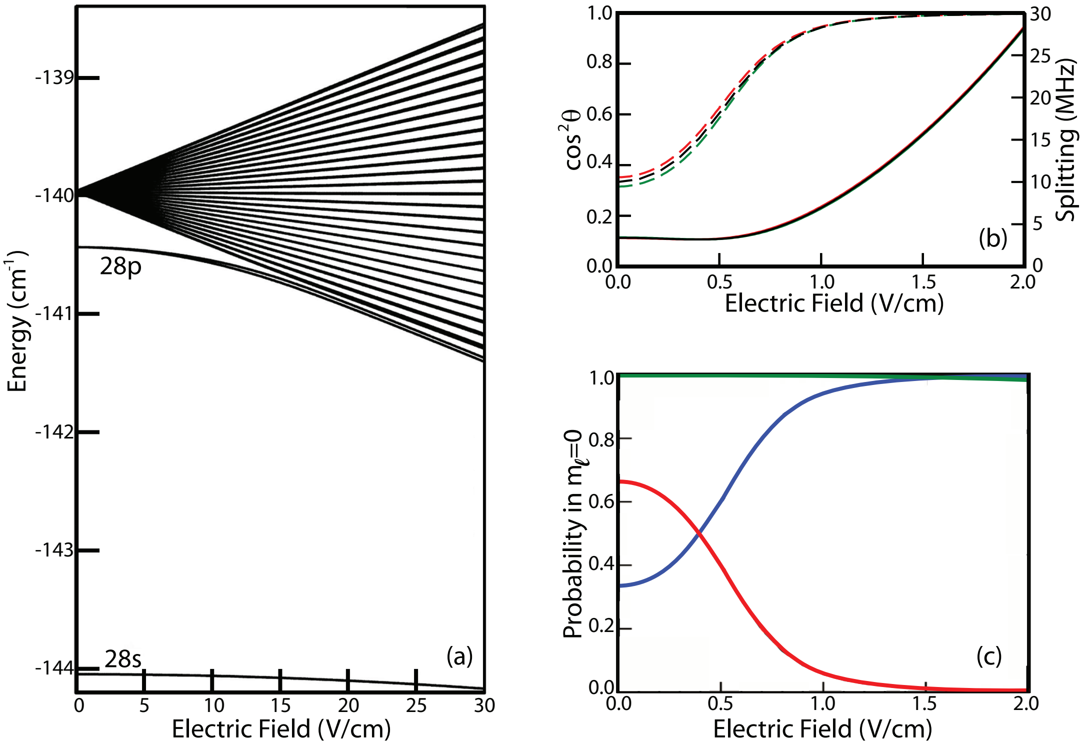

Figure 3.1: (a) Plot of the calculated Stark spectrum for $n = 28$ in lithium shows that the p states' quantum defect ($\delta = 0.047$) leaves them well separated from the manifold for electric fields of less than five volts per centimeter [4]. (b) Plot of the energy splittings (solid curves) and admixture parameters, $\cos^2\theta$ (dashed curves), for the $28p_{1/2}$, $28p_{3/2}$ $m_J = \pm 1/2$ fine-structure states as a function of electric field. In zero magnetic field (black) the $m_J = \pm 1/2$ states behave identically with $\cos^2\theta = 1/2$ at the minimum splitting $E = E_0$ near $F_0 = 0.4$ V/cm. In a weak magnetic field B_s, the $m_J = \pm 1/2$ states are similar, but not identical with $\cos^2\theta = 1$, $E \simeq 7.3\ \mathrm{MHz/(V/cm)}^2 F^2 \mp \mu_B B_s$ for $F \gg F_0$ and $\cos^2\theta \simeq (1 \mp \eta)/2$, $E \simeq E_0 + 1.6\ \mathrm{MHz}\eta^2$ near $F = F_0$ with $\eta = \mu_B B_s / E_0 \ll 1$. The $m_J = 1/2$ (blue) and $m_J = -1/2$ (red) curves are shown explicitly for $B_s = 100$ mG.[5]. (c) Plot of $|-\rangle$ (blue) and $|+\rangle$ (red) which adiabatically connect the $J = 1/2$ and $J = 3/2$ states to the high field $|m_\ell| = 0$ and 1 states respectively projected onto the $m_\ell = 0$ state as a function of electric field. The green curve is the sum of the red and blue curves, indicating that there is very little mixing of other angular momentum states.

The qubits are encoded in Rydberg wave packets as the complex amplitudes of two np fine-structure eigenstates and are coherently shuttled between two subspaces using pulsed electric fields. The results presented here focus on $n = 28$, but analogous results have been obtained for other states. The lithium np levels have a nonzero quantum defect ($\delta = 0.047$)

as shown for $n = 28$ in figure 3.1(a) and the $28p$ electron therefore undergoes negligible Stark mixing with other orbital angular momentum states in electric fields $F \leq 2$ V/cm as shown in figure 3.1(c), and $\ell = 1$ remains a good quantum number. In a small electric field ($F \ll 1$ V/cm), the fine structure energy splitting is much larger than the Stark energy shifts, so the eigenfunctions are entangled superpositions of the electron spin and orbital angular momentum states, specifically the field dependent eigenstates $|+\rangle$ and $|-\rangle$ corresponding to the $J = 3/2$ and $J = 1/2$ zero field states. In the absence of a magnetic field, the $m_j = \pm 1/2$ states behave identically so we explicitly consider only the $m_j = 1/2$ states where $|+\rangle = \sin\theta\,|0\rangle\,|\uparrow\rangle + \cos\theta\,|1\rangle\,|\downarrow\rangle$ and $|-\rangle = \cos\theta\,|0\rangle\,|\uparrow\rangle - \sin\theta\,|1\rangle\,|\downarrow\rangle$ where θ is a field dependent parameter, $|0\rangle$ and $|1\rangle$ are the $28p$ $|m_\ell| = 0$ and 1 eigenstates, and $|\uparrow\rangle$ and $|\downarrow\rangle$ are the up and down spin projections. The total electronic angular momentum (J) is a conserved quantity in the presence of the spin-orbit coupling, and therefore, we refer to this basis as the J subspace. The lithium np fine-structure states exhibit an avoided level crossing as a function of an externally applied static electric field. Near the center of the avoided crossing ($F = F_0 = 0.4$ V/cm for $n = 28$), the energy splitting between the two states is essentially independent of small changes in the electric and magnetic fields as shown in figure 3.1(b), resulting in an approximate decoherence-free subspace in which the qubits are relatively immune to phase errors.

In large fields ($F \geq 1.3$ V/cm for $n = 28$), the Stark shift between the eigenstates of the z-projection of electronic orbital angular momentum ($|m_\ell| = 0$ and 1) greatly exceeds the fine structure splitting, so the electron spin and orbital angular momentum decouple, leaving the qubits in a basis comprised of the m_ℓ eigenstates, $|0\rangle$ and $|1\rangle$. In this m_ℓ basis, the z-projection of the orbital angular momentum is a conserved quantity, and the energy splittings between the qubit states increase as F^2. This basis is attractive for controlling resonant interactions between Rydberg atoms, like those discussed in chapters 5 and 6, by using applied electric fields to Stark tune the energy spacings, but it is also prone to qubit dephasing due to stray electric (F_s) and magnetic (B_s) fields as shown in figure 3.1(b).

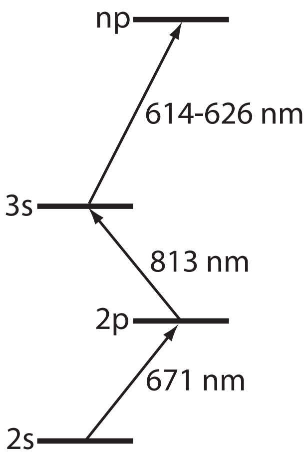

Figure 3.2: Schematic of the excitation of p Rydberg states in lithium. A LDS 698 dye laser producing light at 671 nm excites population from the ground state ($2s$) to the $2p$ state. A LDS 821 dye laser drives population from the $2p$ to the $3s$ state with 813 nm light. A DCM dye laser tuned between 614 nm and 626 nm excites a particular np doublet with $23 < n < 33$. All laser are vertically polarized parallel to the direction of the applied electric field.

The experiments are performed in the chamber shown in figure 2.5. Parallel field plates with half-inch separation are used to create vertical electric fields in the interaction region. These fields are used to shuttle the qubits between subspaces, to field-ionize the Rydberg atoms enabling the measurement of the state of the ensemble, and as will be discussed in chapter 4, to resonantly dress the atoms.

Light from three Littman dye lasers that is polarized parallel to the applied electric field is focused into a counter-propagating atomic beam, driving the transitions shown in figure 3.2. The z projection of the total electronic angular momentum, m_J, is conserved during the laser excitation in the presence of an electric field, $F \leq 2$ V/cm. Angular momentum selection rules dictate that only $|m_J| = 1/2$ Rydberg levels with $m_\ell = 0$ character are excited from the $3s$ state. A μ-metal shield reduces the magnetic field in the interaction region to < 100 mG. As shown in figure 3.1(b), the $m_J = \pm 1/2$ states behave identically in the absence of a magnetic field, so for simplicity consider only $m_J = 1/2$.

The field-dependent $28p$, $m_J = 1/2$ eigenstates ($|-\rangle$ and $|+\rangle$) adiabatically connect the zero-field $J = 1/2$ and $J = 3/2$ states to the strong field $m_\ell = 0$ and $m_\ell = 1$ states respectively. Expanding $|-\rangle$ and $|+\rangle$ in the m_ℓ basis ($|0\rangle$ and $|1\rangle$) gives

$$|+\rangle = \sin\theta\,|0\rangle\,|\uparrow\rangle + \cos\theta\,|1\rangle\,|\downarrow\rangle \tag{3.1a}$$

and

$$|-\rangle = \cos\theta\,|0\rangle\,|\uparrow\rangle - \sin\theta\,|1\rangle\,|\downarrow\rangle \tag{3.1b}$$

where θ is a field-dependent admixture parameter (see figure 3.1(b) and (c)).

The laser excitation takes place in the small static electric field at the center of the avoided crossing ($F_0 = 0.4$ V/cm) where $\theta = 45^o$ and the energy splitting between the two fine-structure levels has a shallow minimum, $E = E_0 \approx 3.2$ MHz. Both fine-structure states are excited within the coherent bandwidth of the third dye laser pulse (200 MHz$\sim \frac{1}{5\ \mathrm{ns}}$). Identical wave packets are produced in every atom on each laser shot because any variation in the duration of the third laser pulse is $\ll 1/E_0$. The wavepacket in atom k at a time t is

$$\Psi_J^k(t) = \frac{1}{\sqrt{2}}\left(|-\rangle + |+\rangle\, e^{-i\phi_k(t)}\right) = \frac{1}{\sqrt{2}}\left[1, e^{-i\phi_k(t)}\right]_J \tag{3.2}$$

where $\phi_k(t) = \int_0^t E_k(t')dt'$, $t = 0$ at the peak of the third laser pulse and we assume without loss of generality that the amplitude of the $|-\rangle$ state is positive real. In a perfect decoherence-free subspace, the energy splitting between the states would have the same time-independent value for all the atoms in the ensemble, $E_k(t) = E_0$, so all the qubits would acquire phase at the same rate, specifically $\phi_k(t) = \phi_0(t) = E_0 t$.

To measure the coherence of the qubit after a time $t = \delta$, a fast rising (1 to 2 ns) electric field step increases the field to 1.8 V/cm, projecting the wave packet onto the m_ℓ basis by performing a Hadamard transformation,

$$U_H = \frac{1}{\sqrt{2}}\begin{bmatrix} 1 & 1 \\ 1 & -1 \end{bmatrix}. \tag{3.3}$$

The field step coherently mixes the amplitudes of $|+\rangle$ and $|-\rangle$, converting the phase difference between the states into amplitude differences in $|0\rangle$ and $|1\rangle$, thus acting as an intra-atomic beam splitter. If perfect coherence is maintained, the wave function of atom k in the new basis is

$$\Psi^k_{m_\ell}(t) = \cos\frac{\phi_k(\delta)}{2}\,|0\rangle + \sin\frac{\phi_k(\delta)}{2}\,|1\rangle\, e^{-i\varphi_k(t)} = \left[\cos\frac{\phi_k(\delta)}{2}, \sin\frac{\phi_k(\delta)}{2} e^{-i\varphi_k(t)}\right]_{m_\ell} \tag{3.4}$$

where $\varphi_k(t) = \pi/2 + \int_\delta^t \epsilon_k(t')dt' = \varphi_k(t_{m_\ell}) = \pi/2 + \int_0^{t_{m_\ell}} \epsilon_k(t'_{m_\ell})dt'_{m_\ell}$, $\epsilon_k(t)$ is the time-dependent Stark splitting between the $|m_\ell| = 0$ and 1 levels, t_{m_ℓ} is the time in the m_ℓ basis and where we ignore an irrelevant global phase factor. The explicit electron spin notation is dropped since the spin states for each m_ℓ level are degenerate in the absence of a magnetic field, and the final-state measurements are spin independent. Ramped field ionization is used to measure the population in the $|0\rangle$ and $|1\rangle$ states. The total Rydberg signal decreases monotonically as the ionization pulse is delayed, as shown in figure 3.3(c). Spontaneous emission, primarily to the $2s$ and $3s$ states, and the motion of the Rydberg atoms from beneath the extraction slit account for this loss of signal but do not affect the coherence of the remaining atoms. Since the simultaneous measurement of an ensemble of N atoms is equivalent to the sum of N single-atom measurements, normalizing the population in the m_ℓ states to the total Rydberg atom population gives the probabilities that a qubit is in the $|m_\ell| = 0$ and 1 states ($\langle P_{0,1}\rangle$). Figure 3.3(a) shows the qubit probability oscillating between the $|m_\ell| = 0$ and 1 states as a function of δ. For a fixed value of δ, the probabilities of finding the qubit in $|m_\ell| = 0$ and 1 states are independent of the time, t_{m_ℓ}, that the qubit is left in the m_ℓ basis, which ensures that amplitude noise due to environmental interactions is negligible.

To measure the phase acquired by a qubit in the m_ℓ basis, we first create a qubit with equal amplitude in both states by projecting onto the m_ℓ basis after one eighth of the spin orbit period ($\delta = \pi/4E_0 \simeq 40$ ns). After a time t_{m_ℓ} in the m_ℓ basis, the qubit state vector

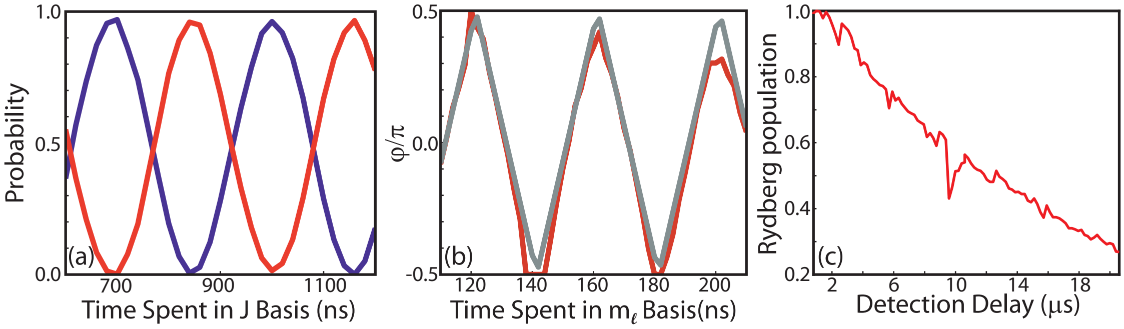

Figure 3.3: (a) Plot of the measured state probability. The probability oscillates between the $|0\rangle$ (red) and $|1\rangle$ (blue) as a function of the time, δ, the qubit remains in the J basis. (b) Plot of the phase ($\varphi = \epsilon_0 T$, $\epsilon_0 = 23$ MHz) acquired in the m_ℓ basis. The measured (red) and predicted (grey) phase show good agreement. (c) Plot of the total Rydberg signal as the ionization pulse is delayed. The observable Rydberg population decreases due to spontaneous emission and excited atoms moving from beneath the extraction slit.

is $1/\sqrt{2}[1, e^{-i\varphi_k(t_{m_\ell})}]_{m_\ell}$. At a time $t_{m_\ell} = T$, we apply a $\sqrt{NOT}$ gate,

$$U_{\sqrt{NOT}} = \frac{1}{2}\begin{bmatrix} 1-i & 1+i \\ 1+i & 1-i \end{bmatrix}. \tag{3.5}$$

The gate is realized using a negative Hadamard field step that projects the qubit back onto the J basis, followed by a delay equal to one-quarter of the spin-orbit period, $\Delta = \pi/2E_0 \simeq 80$ ns, and a final positive Hadamard field step that projects the qubit back onto the m_ℓ basis. The $\sqrt{NOT}$ gate acts as an intra-atomic interferometer for the m_ℓ states converting the phase difference between $|0\rangle$ and $|1\rangle$ into a probability difference in the same basis,

$$\left| U_{\sqrt{NOT}} \begin{bmatrix} 1/\sqrt{2} \\ e^{-i\varphi_k(T)}/\sqrt{2} \end{bmatrix} \right|^2 = \frac{1}{2}\begin{bmatrix} 1-\sin(\varphi_k(T)) \\ 1+\sin(\varphi_k(T)) \end{bmatrix}. \tag{3.6}$$

Figure 3.3(b) shows good agreement between the observed and expected phase acquired in the m_ℓ basis for short times where we make the approximation that the Stark energy splitting is time independent and the same for all atoms ($\epsilon_k(t) = \epsilon_0 \simeq 23$ MHz), so $\varphi(T) = \epsilon_0 T$.

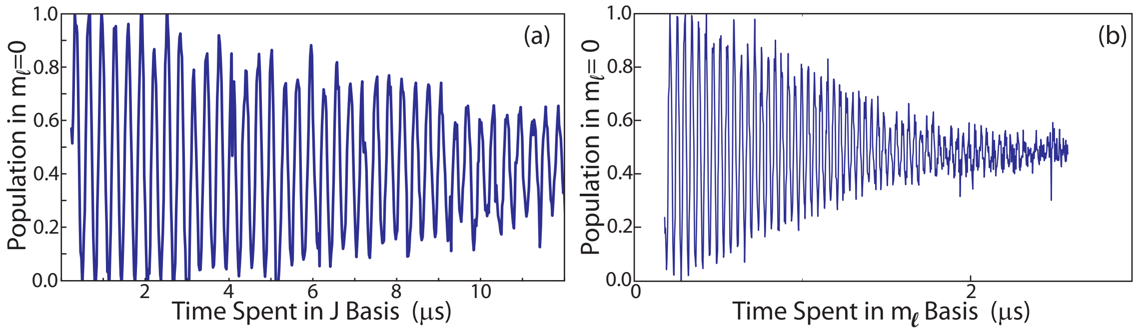

Figure 3.4: (a) Plot of a typical decay of the amplitude modulation for qubits left in the J basis. The modulation amplitude drops below 0.5 in about 10 μs. Decay time as much as a factor of two smaller have been observed on different days under nominally identical conditions. In the J basis, the energy difference between the qubit states is insensitive to small variations in the electric field, so all qubits acquire phase at the same rate, and the coherence of the ensemble decays slowly in comparison to the dephasing time in the m_ℓ basis. (b) Plot of a typical decay of the amplitude modulation for qubits left in the m_ℓ basis. The energy splitting varies as the square of the electric field which causes the ensemble to dephase quickly [4, 5].

3.2 Dephasing and Decoherence

If perfect coherence is maintained in either subspace, $\langle P_0 \rangle$ and $\langle P_1 \rangle$ will continue to oscillate between 0 and 1 for as long as observable Rydberg population remains. Figure 3.4 shows that the modulation amplitude, $C(t)$, decreases in both subspaces, indicating that the coherence is not maintained across the ensemble. $C(t)$ falls much more rapidly in the m_ℓ basis indicating a loss of macroscopic phase coherence for $T > 2$ μs, while in the J basis, the coherence persists for 10 to 15 μs since the J subspace is an approximately decoherence-free.

No evidence is found for variations in the qubit amplitude, nor is any expected within the time duration of the experiments. Stray fields and long-range collisions are much more likely to induce phase changes via adiabatic energy shifts than to cause population transfer between qubit levels. In addition, spontaneous emission from the upper to the lower qubit level in either basis is negligible, and we measure no population transfer to other ℓ or m_ℓ states at any delay. Accordingly, at all delays, the measured values of $\langle P_{0,1} \rangle$, averaged over several oscillations, are equal to 1/2 within experimental accuracy. Therefore, we assume that the decay of $C(t)$ is due solely to the absence of a well-defined qubit phase in the ensemble.

In the m_ℓ basis, the coherence time is independent of the Rydberg atom and background gas densities, so atom-atom collisions are not a primary source of decoherence. Rather, inhomogeneous dephasing is the result of time-independent variations in $\epsilon_k(t)$ due to the sensitivity of the energy splitting between the qubit states to stray electric (F_s) and magnetic (B_s) fields. Atoms in different locations have different energy splittings and acquire phase at different rates due to local variation in field. Additionally, homogeneous dephasing occurs as the atoms move through the interaction region, encountering different patch fields which results in time-dependent energy splittings. Since the phase of an individual qubit is the time integral of this splitting, these time dependent fields destroy the coherence of the wavepacket in each atom. Once lost, this coherence cannot be recovered without explicit knowledge of the time dependent fields experienced by each atom.

Stray fields $F_s \sim 20$ mV/cm or $B_s \sim 200$ mG or some combination of weaker fields could account for the rapid dephasing in the m_ℓ basis. Electric field variations of this magnitude would lead to a dephasing time in the J basis of one millisecond. Magnetic fields of this size are unlikely as they are several times larger than indicated by direct measurement. Furthermore, the magnetic field dependence of the admixture coefficients introduce small errors in the logic gates, but the success of the dynamic decoupling experiments described in this chapter suggests that $B_s \ll 100$ mG. A magnetic field $B_s \sim 200$ mG would lead to a dephasing time of 100 μs in J. It is therefore unlikely that the loss of coherence in the J basis is due to stray fields. Since inhomogeneous dephasing is negligible in the J basis, $C(t)$ is a direct measure of the ensemble coherence in this basis, and is equal to twice the magnitude of the off-diagonal components of the density matrix.

Although the exact interaction leading to the decoherence in the J basis is unknown, it is likely that both of the following interactions play a role. First, time-dependent interactions due to long-range collisions between atoms or collisions between Rydberg atoms and a small number of photoelectrons/photoions in the ensemble [92] would alter the phase of individual atoms in an unpredictable way. Second, because the electron and nuclear spins are not measured in the experiment, the time-independent hyperfine interaction results in an intrinsic uncertainty in the energy splitting between the qubit levels within each atom. In lithium, the hyperfine splitting between the $28p_{1/2}$, $F = 1, 2$ eigenstates is $\delta E_{hfs} \simeq 34$ kHz while that between the $28p_{3/2}$, $F = 0, 1, 2, 3$ eigenstates is less than 1 kHz [93], where F is the is the quantum number associated with the total atomic angular momentum, $\vec{F} = \vec{J} + \vec{I}$, where $\vec{I}$ is the nuclear spin. Since both $F = 1$ and 2 components are excited by the laser, the qubit energy is not well-defined within each atom. Accordingly, we expect a modulation or quantum beat in the time-dependent coherence. This modulation should have a full period $\tau_{hf} \simeq 2\pi/\delta E_{hfs} \simeq 28$ μs. Therefore, in the absence of any other interactions, the coherence should drop from its initial maximum to some minimum value around a time of $\tau_{hf}/2 \simeq 14$ μs which is not inconsistent with the observed coherence time. In the frequency domain, the limited observation time ensures that the hyperfine states are not well-resolved, resulting in a homogeneous qubit energy uncertainty $\sim \delta E_{hf}$ and a corresponding phase uncertainty in each atom. Because there are no observable Rydberg atoms left in the interaction region after twenty microseconds, we are not able to determine if the coherence partially recovers after a full hyperfine beat period. Regardless of the precise cause of the decoherence in the J basis, it is clear that even when encoded in a nominally decoherence-free subspace which immunizes them against one or more dominant interactions, other couplings may still severely limit the useful lifetime of qubits [4, 5].

3.3 Bang-Bang Dynamic Decoupling

Pulsed dynamic decoupling can overcome this limitation by simultaneously eliminating decoherence due to multiple environmental interactions. This section describes a bang-bang scheme that is similar to the Carr-Purcell technique for measuring or eliminating the effects

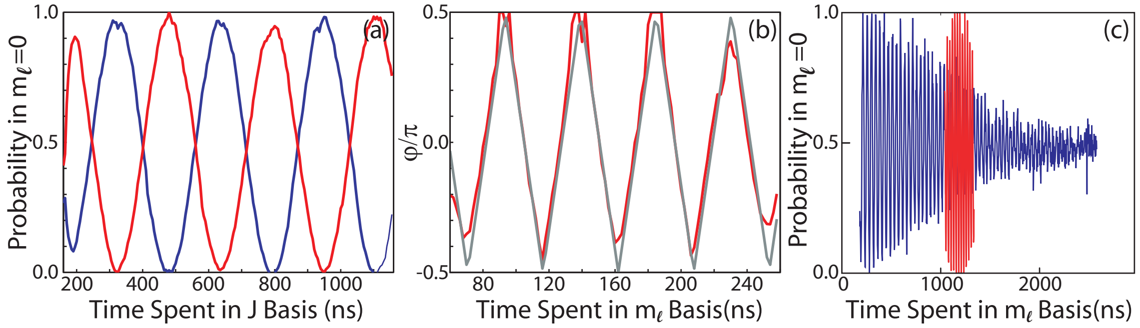

Figure 3.5: (a) Plot of P_0 with (red) and without (blue) a NOT operation. (b) Plots of the measured (red) and predicted (grey) phase following a single NOT operation show good agreement. (c) Plot of the probability in $m_\ell = 0$ with (red) and without (blue) a single NOT operation applied near $T = 500$ ns. The NOT operation causes the qubits to rephase near $2T = 1000$ ns, creating a population echo which has the same amplitude modulation as the initial qubit [5].

of spin diffusion in NMR experiments [36, 37]. Rather than using radio-frequency pulses to flip spins [27, 28], electric field pulses toggle the spin-orbit coupling to perform a series of rapid NOT operations on the qubit, erasing the slow acquisition of environmental phase noise. The NOT operation,

$$U_{NOT} = \begin{bmatrix} 0 & 1 \\ 1 & 0 \end{bmatrix}, \tag{3.7}$$

flips the state vector of the qubit as shown in figure 3.5(a). The NOT gate implementation is similar to that of the $\sqrt{NOT}$ gate, except the qubit is left in the J basis for one-half the spin-orbit period ($\Delta \sim 160$ ns) before the final Hadamard step projects the qubit back onto the m_ℓ basis.

A single NOT operation is used to determine to what degree the macroscopic dephasing in the m_ℓ basis is due to time independent interactions. At $t_{m_\ell} = 0$, the qubit $[1/\sqrt{2}, 1/\sqrt{2}]_{m_\ell}$ is created, and after a time T, a NOT gate is applied giving

$$U_{NOT} \begin{bmatrix} 1/\sqrt{2} \\ e^{-i\varphi_k(T)}/\sqrt{2} \end{bmatrix} = \begin{bmatrix} e^{-i\varphi_k(T)}/\sqrt{2} \\ 1/\sqrt{2} \end{bmatrix} = \begin{bmatrix} 1/\sqrt{2} \\ e^{i\varphi_k(T)}/\sqrt{2} \end{bmatrix}. \tag{3.8}$$

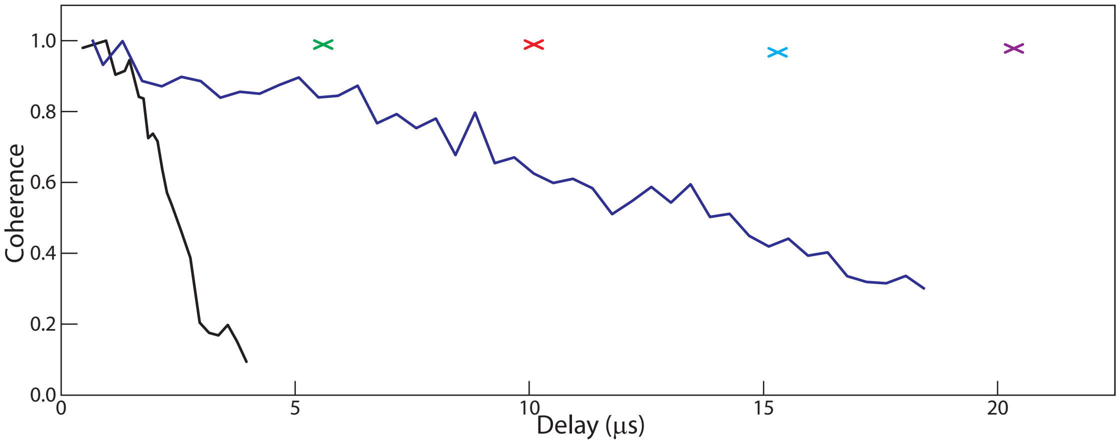

Figure 3.6: Plot of the coherence as a function of delay for a qubit $1/\sqrt{2}[1, e^{-i\varphi}]$: stored in m_ℓ using a single NOT gate and measured following a $\sqrt{NOT}$ (black line); stored in J (blue line); measured following a $\sqrt{NOT}$ gate after the application of 17 (green x), 31 (red x), 41 (cyan x) and 63 (purple x) NOT gates temporally separated by $\tau_{BB} = 160$ ns [5].

Thus, the NOT operation effectively reverses the sign of the qubit phase in each atom. If the dephasing is due only to time independent interactions, the initial qubit ensemble will rephase at a time $2T$. This quantum state "echo" can be characterized by the delay-dependent modulations in $\langle P_0 \rangle$ and $\langle P_1 \rangle$ when a $\sqrt{NOT}$ gate is applied at delays near $2T$ as shown in figure 3.5(c) [35, 94]. In analogy with spin and photon echoes, the modulation amplitude, $C(t)$, is equal to twice the magnitude of the off diagonal terms in the qubit density matrix, and is a direct measure of the coherence.

The black line in figure 3.6 shows the coherence after a single NOT operation. Notably, it does not decrease exponentially with T. It remains instead essentially constant for a characteristic coherence time $\tau_c \sim 700$ ns, and then decreases rapidly with a functional dependence which is similar to that observed in NMR experiments for spins moving through a spatially varying magnetic field [36]. τ_c defines a "phase-memory" time for individual atoms during which the qubit energy splitting is essentially constant and nearly perfect coherence is maintained.

Interestingly, the application of additional electric field pulses can dramatically extend this phase memory time without any explicit knowledge of the decoherence mechanism.

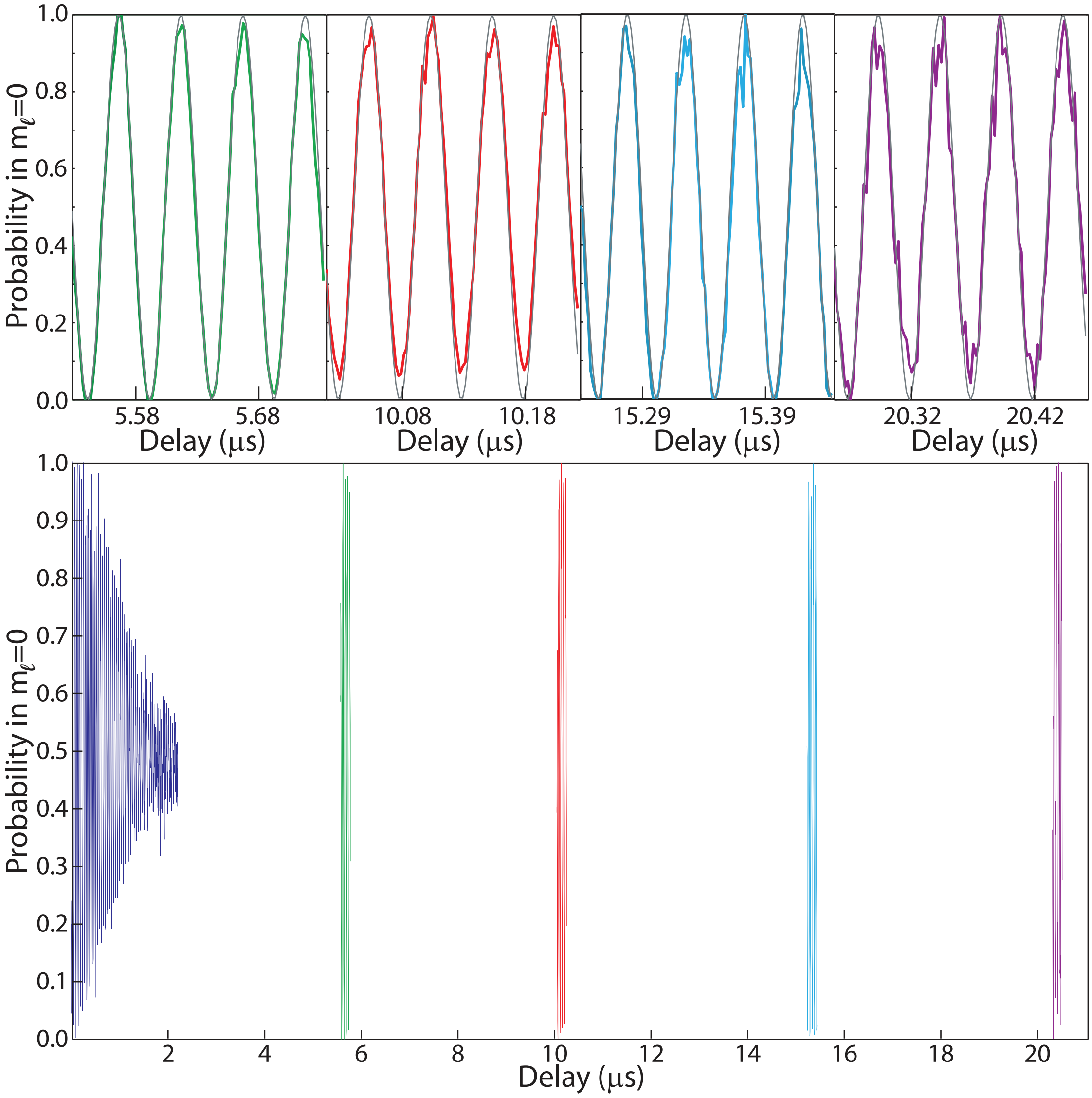

Figure 3.7: Plots of the probability in $m_\ell = 0$ with and without bang-bang control sequences. In the lower figure, the oscillations of the $m_\ell = 0$ probability decay when the qubit is left in the m_ℓ basis. The oscillations are preserved by 17 (green), 31 (red), 47 (cyan) and 63 (purple) *NOT* gates separated by 160 ns. The plots above show good agreement between the measured and predicted (grey) oscillations for all the echo pulse sequences [5].

Specifically, by applying a series of NOT gates, separated by a time τ_{BB} between the final field step of one gate and the initial field step of the next, good qubit coherence is maintained for times much greater than τ_c provided $\tau_{BB} \ll \tau c$. Figure 3.7 shows the echo signals formed by sequences of NOT gates with $\tau_{BB} = 160$ ns. These pulse sequences maintain excellent coherence ($> 95\%$) with predictable qubit phase (see upper plots in figure 3.7) for as long as there are detectable Rydberg atoms in the interaction region. The measured coherence levels for these pulse sequences are denoted with Xs in figure 3.6.

As previously noted, in the frequency domain the approximate decoherence-free subspace in J is the result of the field independence of the fine structure states at the center of the avoided-level crossing. This avoided crossing is due to the spin-orbit interaction. In the time domain, the decoherence-free subspace can be attributed to the rapid Rabi flopping of the qubit amplitudes due to this same interaction. Since the spin-orbit coupling is also the interaction that flips the qubits in the bang-bang pulse sequence, one might expect that leaving the qubits in the J basis where the spin-orbit coupling continuously flips the m_ℓ state vector at a rate which is always greater than that in the pulse sequence would better preserve the coherence of the qubit [13–16]. To understand why the bang-bang control is more effective despite the lower flip rate, we examine a range of pulse intervals, τ_{BB} and energy splittings, ϵ_0. We find that bang-bang control works best when $\epsilon_0\tau_{BB} \simeq (2*N+1)\pi$ and is least effective, with coherence times less than that observed for static encoding in J, when $\epsilon_0\tau_{BB} \simeq 2*N\pi$ where N is an integer. For $\epsilon_0\tau_{BB} \simeq (2*N+1)\pi$, the bang-bang control sequence flips the J state vector during each cycle, thus performing a NOT operation in both the m_ℓ and J bases, erasing the slow acquisition of phase noise in both. This dual suppression obviates the need for more rapid flips and is responsible for the surprisingly long coherence observed. In the latter case, in the absence of decoherence, the $2N\pi$ phase advance in the m_ℓ basis during each bang-bang cycle leaves the J state vector unchanged. Given the rapid decoherence in m_ℓ, it is perhaps not surprising that qubits subjected to a bang-bang sequence with $\epsilon_0\tau_{BB} \simeq 2*N\pi$ have shorter coherence times than those statically stored in J [5].

Thus, we have demonstrated that this bang-bang control scheme of periodically flipping the qubit state vector in both bases effectively decouples the qubits from the environment even when the precise interactions causing the decoherence are unknown. The next chapter will present an equally effective scheme for preventing decoherence that utilizes continuous dynamic decoupling.

Chapter 4

Continuous Dynamic Decoupling

The previous chapter described a pulsed dynamic decoupling scheme which extended the coherence time of an ensemble of single qubits by repeatedly flipping the qubit state vector via time dependent control fields in a method analogous to spin-flip narrowing in NMR. The experiments discussed here demonstrate an alternative dynamic decoupling scheme in which an applied resonant radio frequency field creates a robust decoherence-free subspace, effectively suppressing decoherence in analogy with spin-locking in NMR [37]. Similar continuous dynamic decoupling schemes have been discussed theoretically [30, 95] and demonstrated with modest success on qubits based on superconducting Josephson junction circuits [96]. In our scheme, the resonant radio-frequency field applied to the ensemble of qubits encoded on the fine-structure states of lithium Rydberg atoms effectively frequency-locks the component states, creating a more robust decoherence-free subspace [4, 97].

4.1 Experiment and Results

Ensembles of single qubits are encoded on the np fine structure states of lithium in the same experimental apparatus and via the same procedure as that used in the experiments discussed in chapter 3, and again, we focus on $n = 28$. In the experiments discussed in this chapter, we apply radio frequency pulses with constant amplitude F_{rf}, frequency ω

and duration T_{rf} to the top capacitor plate via a coaxial transmission line. To quantitatively assess how these control pulses influence the coherent evolution of the qubits in the ensemble, we determine the transition dipole moment, $z_0 = \langle +|\, z\, |-\rangle$, by measuring the population transfer between the qubit states as a function of the pulse area, $\Theta = F_{rf} z_0 T_{rf}$, at resonance $\omega = E_0$. Although single-photon transitions between the 28p eigenstates are strictly prohibited in the dipole approximation, rf coupling between the qubit levels is facilitated by the small static electric field in which the qubits are produced. The static field mixes approximately 0.2% of the $28d$ state amplitude into the predominately $28p$ eigenstates so that the matrix element $z_0 = \langle +|\, z\, |-\rangle$ is non-zero.

For the population transfer measurements, the atoms are prepared in the $|-\rangle$ state before they are exposed to the rf field. Recall that the laser excitation creates a linear combination $(|+\rangle + |-\rangle)/\sqrt{2}$ at $t = 0$. All of the population is then transferred to the $|-\rangle$ state by preforming a $\sqrt{NOT}$ operation on the qubits (ie. they are projected onto the m_ℓ-basis by a fast rising electric field step performing a Hadamard transformation, left for a time $T = \pi/2\epsilon_0 \simeq 11$ ns and then projected back onto the J-basis) at $t = 3\pi/2E_0 \simeq 240$ ns (three quarters of the spin orbit period after excitation)[5]. The atoms are then exposed to the rf field pulse which rotates the state-vector according to a two-level Rabi transformation,

$$U_{Rabi} = \begin{bmatrix} \cos\frac{\Theta}{2} & \sin\frac{\Theta}{2} \\ -\sin\frac{\Theta}{2} e^{-i\phi(T_{rf})} & \cos\frac{\Theta}{2} e^{-i\phi(T_{rf})} \end{bmatrix} \tag{4.1}$$

[97]. Following the rf pulse, an extremely slow rising electric field ramp adiabatically transfers population from the $|-\rangle$ and $|+\rangle$ states to the $|0\rangle$ and $|1\rangle$ states, respectively. The populations in the $|-\rangle$ and $|+\rangle$ states are then given by $\langle P_0\rangle$ and $\langle P_1\rangle$ as measured by state selective field ionization. We determine z_0 by comparing the measured Rabi oscillations as a function of F_{rf} and T_{rf} with the predictions of the two-level Rabi formula, $\langle P_1\rangle = \langle P_+\rangle = \sin^2(1/2F_{rf} + z_{rf}T_{rf})$ [97].

As in the preceding chapter, the coherence of the qubits in the J basis is measured

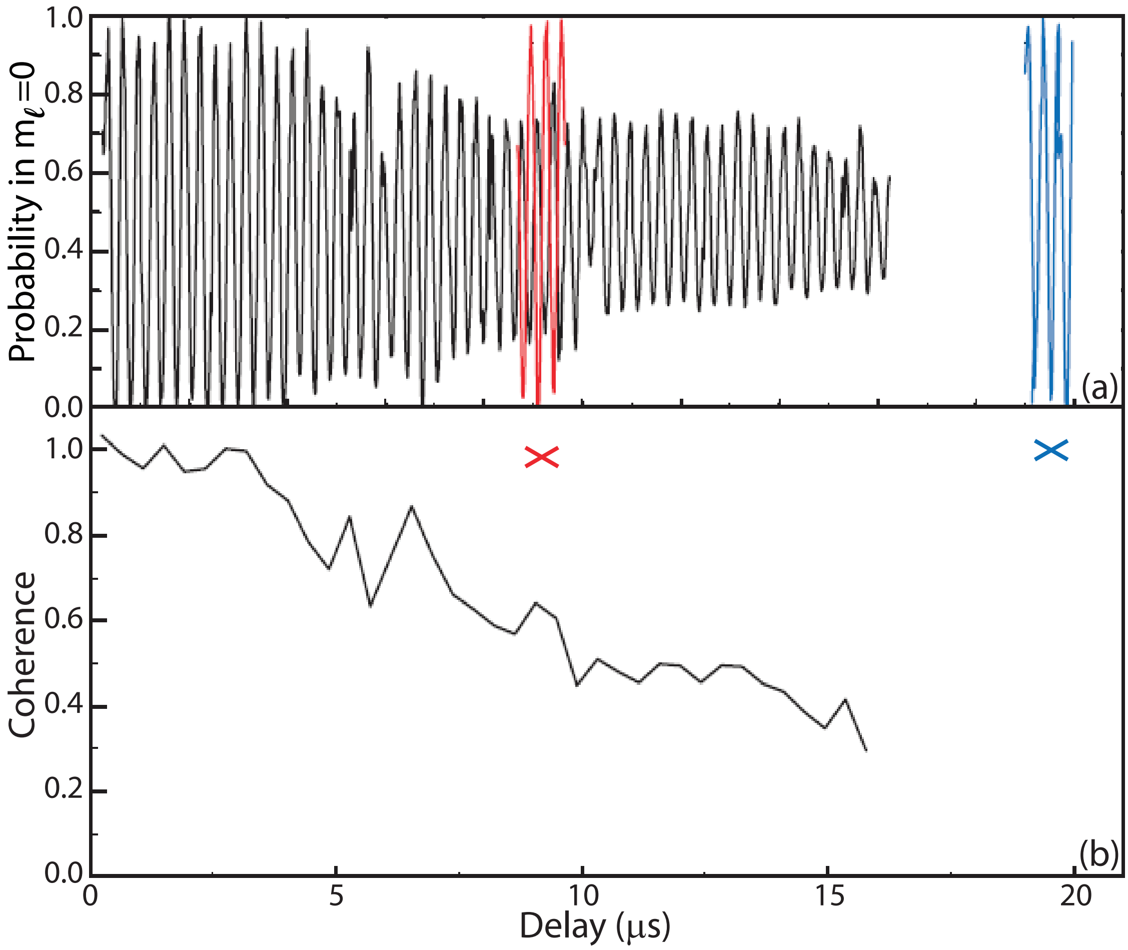

Figure 4.1: (a) Plot of the measured $\langle P_0 \rangle$ oscillates as the delay (δ) between excitation and projection onto the m_ℓ basis is increased in the absence of an rf field (black), approximately 2 μs after the applications of a resonant 3.2 MHz rf pulse with amplitude of 0.035 V/cm and a duration of 6.25 μs (red) and immediately following a resonant, 3.2 MHz rf pulse with amplitude of 0.045 V/cm and a duration of 18.8 μs (blue). In the absence of an rf pulse, the amplitude of the modulations decreases indicating dephasing in the ensemble. Applying an rf pulse with an area of about π (red) or about 4π (blue) preserves the coherence of the ensemble as indicated by the full modulation amplitude. (b) Plot of the coherence indicated by the modulation amplitudes of the curves in (a) when no rf is applied (black line) and when the resonant rf pulse is applied for 6.25 μs (red X) and 18.8 μs (blue X) [4].

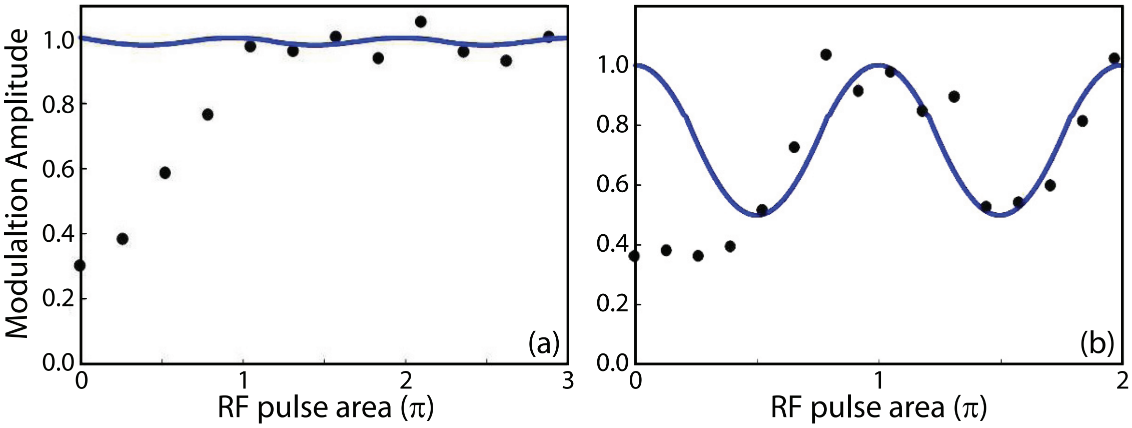

Figure 4.2: Plots of measured (black points) and calculated (blue line) modulation amplitude, $C(\delta)$ as a function of the rf pulse area, Θ for qubit phases (a) $\phi = 0.47\pi$ and (b) $\phi = 0.74\pi$ at the start of the rf pulse. The rf pulse duration is $T_{rf} = 6.25$ μs (20 rf cycles) and $\Gamma_0 \sim \pi/\tau_c$ for $\Theta \sim \pi$. The good agreement between the measured and calculated values of $C(\delta)$ for large pulse areas confirms the prediction that the control pulse substantially reduces environmental interactions for Rabi frequencies $2\Gamma_0 \gg 1/\tau_c$ [4].

by varying the delay (δ) before projecting the qubits onto the m_ℓ basis with a Hadamard field step and observing the modulation amplitude of $\langle P_0 \rangle$. The black curve in figure 4.1(a) shows a typical decline in the modulation amplitude of $\langle P_0 \rangle$ over about ten microseconds, corresponding to the loss of coherence across the ensemble, as was observed in chapter 3 (see figure 3.4). The colored curves in figure 4.1(a) show that applying a weak resonant rf pulse with constant amplitude $F_{rf} < 0.23$ V/cm and frequency $\omega = E_0$ during the time interval $0 < t < \delta$ maintains essentially perfect qubit coherence for much longer times.

Not surprisingly, the effectiveness of the rf control pulse depends on the coupling strength (ie. the resonant Rabi frequency), $\Gamma_0 = F_{rf} z_0$. Figure 4.2 shows the measured modulation amplitude, $C(\delta)$, as a function of the pulse area, $\Theta = \Gamma_0 T_{rf}$, for a fixed pulse duration $T_{rf} = 6.25$ μs (20 rf cycles). For these data sets, in the absence of the rf control pulse, $C(\delta)$ decays in a time $\tau_c \simeq T_{rf}$. Each data point in figure 4.2 is the average value of $C(\delta)$ computed over a small range of delays immediately following the rf pulse. Figures 4.2(a) and (b) show the results obtained when the qubit is allowed to evolve for different times prior to the start of the rf pulse. As described in the next section, the solid curves plotted with the data show the expected modulation amplitudes if perfect coherence is maintained over the ensemble. Apparently, following an rf control pulse, unity amplitude modulations in $\langle P_{0,1} \rangle$ are not a necessary signature of ensemble coherence because $C(\delta)$ depends critically on the phase of the qubit (ϕ) when the rf pulse begins. Instead, coherence is confirmed by good agreement between the measured and predicted values of $C(\delta)$. Figure 4.2 indicates that excellent coherence is maintained provided $\Theta \gtrsim \pi$, ie. $\Gamma_0 \gtrsim \pi/\tau_c$. This observation is consistent with the predictions of the theoretical model presented in the next section. Importantly, we find that by using the correct rf pulse parameters, the coherence of the qubits can be preserved by the rf field without altering them in any detectable way. In particular, for $\Theta = 2N\pi$ where N is an integer, the qubit amplitude and phase (modulo 2π) at the end of the rf control pulse is indistinguishable from an identical, coherently evolving qubit with no rf field present.

4.2 Analysis

As discussed in section 3.2, the decoherence in the J-basis is likely due to time-dependent adiabatic energy shifts due to long-range collisions and the energy uncertainties due to the hyperfine interaction. The data in figure 4.1 show that the coherence of the wavepacket can be preserved by applying a resonant rf field during the time-interval between the wavepacket excitation and detection. The field couples the qubit levels, producing dressed-states whose energy splitting is dominated by the resonant Rabi frequency, thereby suppressing the deleterious effects caused by the uncontrolled environmental energy shifts and energy uncertainties.

Consider an atom in our ensemble in the presence of an rf field with a constant amplitude F_{rf} and frequency $\omega = E_0 + \delta\omega$ where $\delta\omega \ll E_0$ is the rf detuning from the unperturbed atomic resonance frequency. Without the rf field, the energy splitting between the qubit levels is $E = E_0 + \delta E$, where $\delta E \ll E_0$ is an energy shift (or uncertainty) and $\delta E \sim 1/\tau_c$. In accord with our adiabatic assumption, changes in δE are negligible during any time interval $\delta t = 2\pi/E_0$, and the qubit phase error is

$$\delta\phi(r) = \phi(t) - \phi_0(t) = \int_0^t \delta E dt'. \tag{4.2}$$

Provided the rf field is relatively weak, the resonant Rabi frequency $\Gamma_0 = F_{rf} z_0 \ll E_0$, and the rotating wave approximation is valid. In this case, the relevant energy spectrum of the atom-field system is composed of identical pairs of Floquet states, with each pair separated by the rf photon energy [98]. For $F_{rf} = 0$, each state is a direct product of an atomic eigenstate and a photon number state. For example $|+\rangle |N-1\rangle$ and $|-\rangle |N\rangle$ form a pair. The states in each pair are coupled through the interaction potential F_{rf}. By diagonalizing the two-state Hamiltonian [98], we obtain the splitting between the dressed-states as a function of the rf detuning from the atomic resonance and the resonant Rabi frequency,

$$\varepsilon = \sqrt{(\delta E - \delta\omega)^2 + 4\Gamma_0}. \tag{4.3}$$

Accordingly, the energy splitting between the atomic states is $E_{rf} = \omega \pm \varepsilon$, where the $+(-)$ signs correspond to $\delta\omega < (>) \delta E$.

We first note that, for large rf detunings ($|\delta\omega| \gg \Gamma_0$ and $|\delta\omega| \gg \delta E$), $E_{rf} \simeq E_0 + \delta E = E$ and the phase error is identical to that in the absence of the rf field, $\delta\phi = \int_0^t \delta E dt'$. In this case, the rf field should have no effect on the ensemble coherence. Indeed, for detunings $\delta\omega$ much larger than $1/\tau_c$ and Γ_0, we find that the presence of the rf field does not reduce the decoherence rate. Therefore, we will consider only resonant rf fields with $\omega = E_0$.

For a strong resonant field ($\Gamma_0 \gg |\delta E|$), to lowest order, the energy splitting between the dressed-states becomes independent of δE

$$\varepsilon = \sqrt{(\delta E - \delta\omega)^2 + 4\Gamma_0} \simeq 2\Gamma_0 + \frac{\delta E^2}{4\Gamma_0}. \tag{4.4}$$

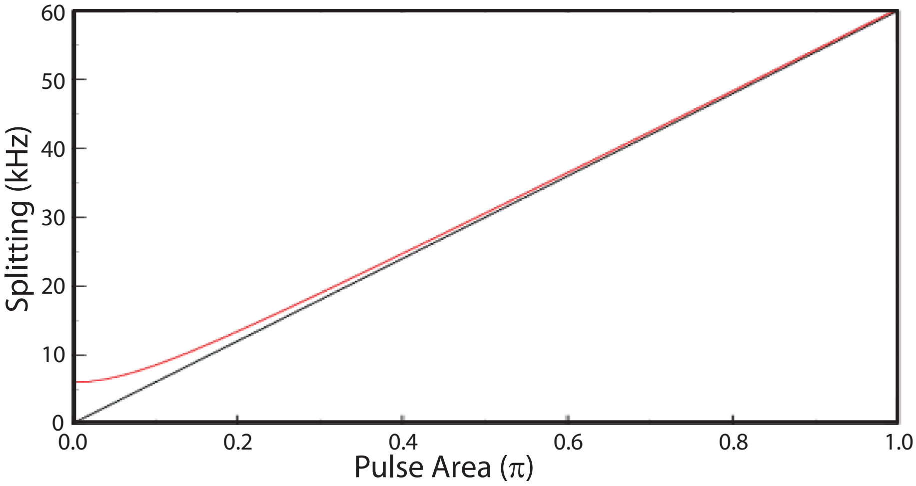

Figure 4.3: Plot of the energy splitting between the fine structure states in the dressed basis for the resonant case (black) and with a patch field of 0.02 V/cm (red). It is clear that the energy shift induced by the field becomes negligible once a strong enough rf pulse is applied.

and the qubit phase becomes

$$\phi(t) = (E_0 + \Gamma_0)t + \int_0^t \frac{\delta E^2}{4\Gamma_0} dt' . \tag{4.5}$$

Within the rotating wave approximation, the phase error can be made arbitrarily small by increasing Γ_0 through the rf field as shown in figure 4.3. Apparently, by coupling the two qubit levels, the rf field creates a more robust decoherence-free subspace in which the Rydberg atoms are immune to a broader class of interactions than they are in the J basis.

It should be noted that the atoms acquire an additional rf-dependent phase-shift which is equal to the pulse area, Θ. For example a π-phase shift is clearly visible in the red curve in figure 4.1a for which $\Theta = \pi$. For a spatially uniform field, Θ has the same definite value for all atoms and, therefore, does not contribute to ensemble dephasing. Moreover, the qubits can remain functional since Θ can be experimentally determined through population transfer measurements. In particular, following a "$2N\pi$-pulse" with $\Theta = 2N\pi$, the qubit's coherence has been preserved, but it is otherwise unaffected by the control field.

Equation 4.4 predicts that the decoherence suppression should "turn-on" for $\Gamma_0 \approx 1/\tau_c$, and should become increasingly more effective for larger Rabi frequencies, as shown in figure 4.2. In the time-domain, we can interpret the increase in the coherence time as the result of dynamic decoupling [15]. The rf field coherently drives probability amplitude between the qubit levels, flipping the qubit at a rate equal to the Rabi frequency. When the Rabi flopping period is short compared to the coherence time, phase errors acquired during each half Rabi cycle are canceled during the next half cycle.

Assuming the qubit maintains perfect coherence, the evolution of the qubit can be modeled using a unitary matrix. From excitation to detection, the qubit goes through four distinct transformations: phase evolution before the rf pulse, rotation and phase evolution during the rf pulse, phase evolution after the rf pulse and finally a Hadamard transformation prior to state selective field ionization. For a resonant rf field, the net transformation matrix which propagates the initial qubit through the rf control pulse,and into the measurement basis is

$$U_{Tot} = U_H U_{\phi_2} U_{Rabi} U_{\phi_1}, \tag{4.6}$$

where

$$U_{\phi_i} = \begin{pmatrix} 1 & 0 \\ 0 & e^{-i\phi_i} \end{pmatrix}, \tag{4.7}$$

$\phi_1 = E_0 t_1$ and $\phi_2 = E_0 t_2$ where t_1 is the delay between excitation and the start of the rf pulse, and t_2 is the time between the rf pulse and the Hadamard projection.

To simulate the experiment, we use equation 4.6 to compute the oscillations in $\langle P_{0,1} \rangle$ as a function of t_2 for fixed values of F_{rf}, T_{rf}, and t_1. The predicted oscillation amplitude $C(\delta)$ for T=6.25 μs (20 cycles) is plotted as a function of the rf pulse area, Θ, and ϕ_1 in figure 4.4. The solid curves in figures 4.2(a) and (b) are line-outs from figure 4.4, and show the predicted modulation amplitude as a function of Θ for the respective experimental conditions. These curves are in good agreement with the experimental data once the Rabi frequency passes a threshold, $\Gamma_0 \sim \pi/\tau_c$. Above this threshold, the control field apparently

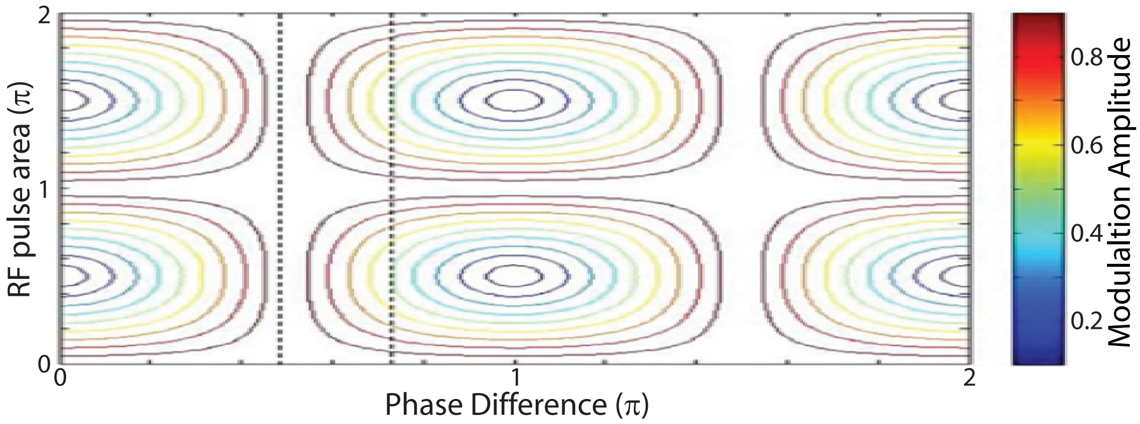

Figure 4.4: Plot of the calculated $\langle P_0 \rangle$ modulation amplitude as a function of the phase at the start of the rf pulse and of the rf pulse area. Perfectly coherent evolution before, during and after the rf control field is assumed. Cuts through the contour plots at the dashed lines are shown as solid lines in figure 4.2 [4].

preserves the ensemble coherence. The residual error after the threshold is in most cases less than 10%. For the appropriate choice of rf field conditions, the qubit remains fully functional following its storage in the rf field. Specifically, for $\Theta = 2N\pi$, the rf field has no measurable effect other than preserving the ensemble coherence.

We have demonstrated that continuous decoherence suppression can be achieved by driving a quantum system with a resonant field. By combining active coherence control with the inherent stability of an approximate decoherence-free subspace we have created a Rydberg qubit system which is immune to phase errors over times approaching the spontaneous emission lifetime of the constituent states. Provided the Rabi frequency is much greater than the inverse of the coherence time in the undriven system, the control field dresses the relevant electronic states, locking their energy separation to the rf frequency. In principle, this frequency locking can be accomplished via any coherent coupling. In the present work, Stark mixing of a small amount of d-character into the nominal p-states enables the coupling. Multiphoton couplings in ladder or lambda configurations, even at optical wavelengths, could be effective in some cases. The ideas presented are, therefore, quite general and might be applicable for a wide range of quantum systems [4].

Chapter 5

Transform Limited Resonant Energy Exchange

Resonant energy transfer can occur when two atoms exchange energy via a dipole-dipole interaction, with one excited to a higher state and the other deexcited to a lower state, thereby conserving the total energy of the pair. In Rydberg atoms, applied electric fields can be used to continuously tune the atomic energy separation via the Stark effect, thus sweeping over such Förster resonances [52]. For interactions between atoms with substantial velocities, like those in an atomic beam or room-temperature gas cell, the duration of the interaction is typically dictated by the transit time of the atoms past one another which depends on the velocity and distances between interacting atoms. Reducing the relative velocity of the atoms can extend the interaction time so that the 2-body dynamics can be probed using applied electric fields. In 1987, Stoneman *et al.* used a chopper wheel to reduce the relative velocity of a thermal atomic beam [99]. Three years later Thomson *et al.* used a similar chopper wheel and reduced the on-resonance time by applying a detuning electric field pulse. Reducing the time on-resonance below the interaction time normally allowed by the atom transit time forced the energy exchange between all atom pairs to begin and end at the same time [54]. Knowing when the exchange process began and ended allowed

Renn *et al.* to probe the interaction with phase locked microwaves, allowing them to observe coherence in the form of Ramsey interference [100, 101]. This chapter will discuss a method for achieving such control in a thermal beam without the use of a chopper wheel. Velocity reduction is achieved by focusing the exciting lasers across a thermal beam as shown in figure 5.1. The cylinder of excited Rydberg atoms spreads longitudinally due to its thermal velocity distribution. The relative velocity of the neighboring Rydberg atoms decreases as the distribution spreads, effectively cooling the atoms prior to Stark tuning onto the resonance.

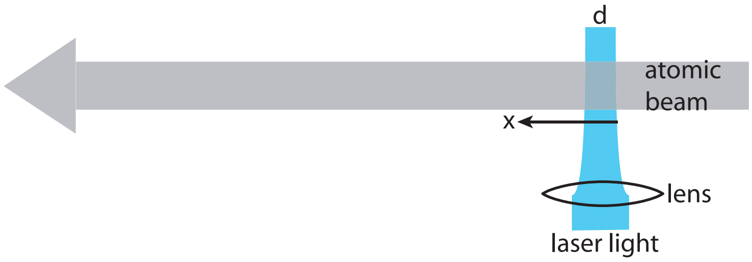

Figure 5.1: Schematic of laser light focused into the potassium atomic beam exciting a cylinder of Rydberg atoms with a Gaussian profile. The atoms spread due to their thermal velocity distribution, so the average relative speed between neighboring Rydberg atoms is reduced.

Specifically, we examine the $29s_{1/2} + 27d_{3/2} \rightarrow 29p_{1/2} + 28p_{1/2}$ resonance in potassium that occurs in an externally applied electric field of 6.43 V/cm. Two degenerate energy exchange processes underlie this resonance. A $29s_{1/2}$ atom can deexcite to the $28p_{1/2}$ state, exciting a $27d_{3/2}$ atom to the $29p_{1/2}$ state. Alternatively, the $29s_{1/2}$ atom can be excited to the $29p_{1/2}$ state while the $27d_{3/2}$ atom is deexcited to the $28p_{1/2}$. Both processes occur at similar rates and are indistinguishable.

5.1 Experiment and Results

These experiments are performed in the vacuum system shown in figure 2.6. Vertically polarized light from three pulsed dye lasers, driving the transitions show in figure 5.2, is

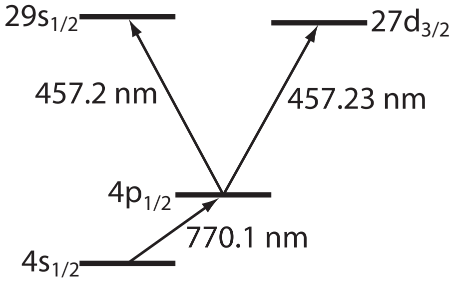

Figure 5.2: Schematic of the excitation scheme for s and d Rydberg states in potassium. 770.1 nm light from a Littman style LDS 765 dye laser populates the $4p_{1/2}$ state. 457.2 nm light from two Coumarin 460 dye lasers transfer population from the $4p_{1/2}$ state to the $29s_{1/2}$ and $27d_{3/2}$ Rydberg states. All three lasers are polarized parallel to the applied electric field, thereby exciting only the $27d_{3/2}$ $|m_j| = 1/2$ resonance [6].

focused into the potassium atomic beam by a 350 mm focal length lens, exciting a cylinder of Rydberg atoms between two parallel conducting plates. After the atoms are excited, the energy exchange interaction is tuned into resonance by a square two-volt pulse with a one to two nanosecond rise time (from the arbitrary waveform generator described in section 2.6) applied to the top parallel plate. To scan over the resonance, a triangle wave sweeps the voltage on the bottom plate at about eight millihertz, slowly varying the electric field with every shot. This method tunes over the resonance more rapidly than scanning the voltage with the AWG allowing for better statistics. Ramped field ionization leaves the $29p_{1/2}$ signal well separated from the $29s_{1/2}$ and $27d_{3/2}$ signal. The $29p_{1/2}$ and initial states ($29s_{1/2}$ and $27d_{3/2}$) ionization peaks are gated and their sizes recorded using an oscilloscope and LabView as described in section 2.5.3. Typically, twelve shots are averaged for every data point.

Delaying the application of the tuning electric field pulse allows the cylinder of Rydberg atoms to expand, reducing the relative velocity between the atoms and extending the interaction time, which results in the narrowing of the resonances shown in figure 5.3. For all the velocity-reduced resonances in figure 5.3, the tuning electric field pulse is 1 μs long. A quantitative determination of each resonance width is made using a least-squares fit to the data via the Marquardt method [102]. For resonances where the velocity has been reduced,

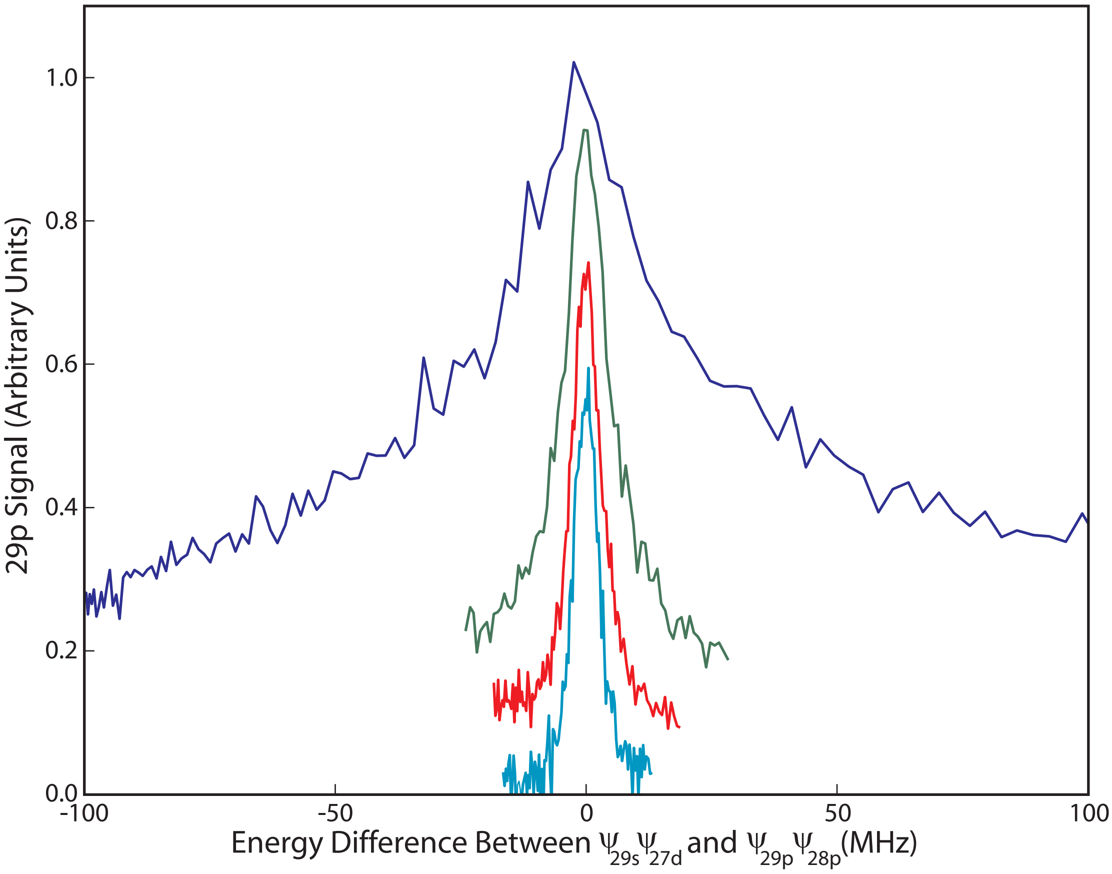

Figure 5.3: Plots of the resonance for different delays of the interaction time. The resonance narrows as the electric field pulse which tunes the dipole-dipole interaction onto resonance for a time t_R is delayed because the average relative velocity between the atoms is reduced, extending the transit time of the atoms. The size of the $29p_{1/2}$ signal is proportional to the density of Rydberg atoms, so the size of the signal drops as the delay between excitation and tuning electric field increases. For clarity, the signal at a delay of 0.5 μs has been multiplied by 3 (green), the signal at a delay of 1 μs has been multiplied by 4 (red), and the signal at a delay of 1.5 μs has been multiplied by 6 (purple) and the peaks have been vertically offset. The thermal resonance (blue) is taken without a tuning field pulse and so $t_R = 3$ μs unlike the other resonances for which $t_R = 1$ μs. The thermal resonance has a width of 40 ± 10 MHz. For 0.5 μs delay (green), the width is 10.2 ± 0.2 MHz. For 1 μs delay (red), the width is 6.54 ± 0.09 MHz, while the width is 5.40 ± 0.09 MHz for a delay of 1.5 μs (purple).

the form of fit is

$$S_c = \frac{A}{(E - E_{off}).^2 + (\lambda/2)^2} + (y_{Eoff} + mE)(y_{Toff} + mS_T) \tag{5.1}$$

where S_c is the $29p$ signal, S_T is the total Rydberg signal, E is the energy difference between the two molecular states ($E = F^2 \times 2.46$ MHz cm^2/V^2 where F is the electric field [99]), and all of the other variables are parameters of the fit. The fit describes a Lorentzian of width λ centered at E_{off} on a background that depends linearly on E and S_T. The background is present because the tuning electric field pulse is too small to completely detune from the thermal resonance. For the data taken without a delay, no tuning pulse was applied. Unlike the velocity reduced resonances, the thermal resonance does not have a Lorentzian lineshape, but is rather a cusp [65]. After the data is fit, the background is subtracted, and the data are binned according to energy such that each bin contains the same number of points.

When the on-resonance time is reduced below the interaction time dictated by the relative velocity of the atoms (ie. the transit time), the resonance broadens as shown in figure 5.4 where the tuning pulse is applied 1.5 μs after excitation. Within the limited interaction time, resonant energy transfer between each atom pair begins and ends at the same time. The broadening is in accord with the uncertainty principle and demonstrates the coherence of the Rydberg-Rydberg interactions over these short time-scales.

To explain quantitatively the narrowing of the resonances at increasing delays and their broadening with reduced on-resonance times, we develop an approximate two-level description of the dipole-dipole interaction. We consider the effect that the delayed interaction has on the effective temperature and density of the interacting atoms. We then use the measured resonance lineshapes to determine the Rydberg density and effective temperature. These parameters allow us to predict quantitatively the degree of broadening that is observed as the allowed interaction time is reduced.

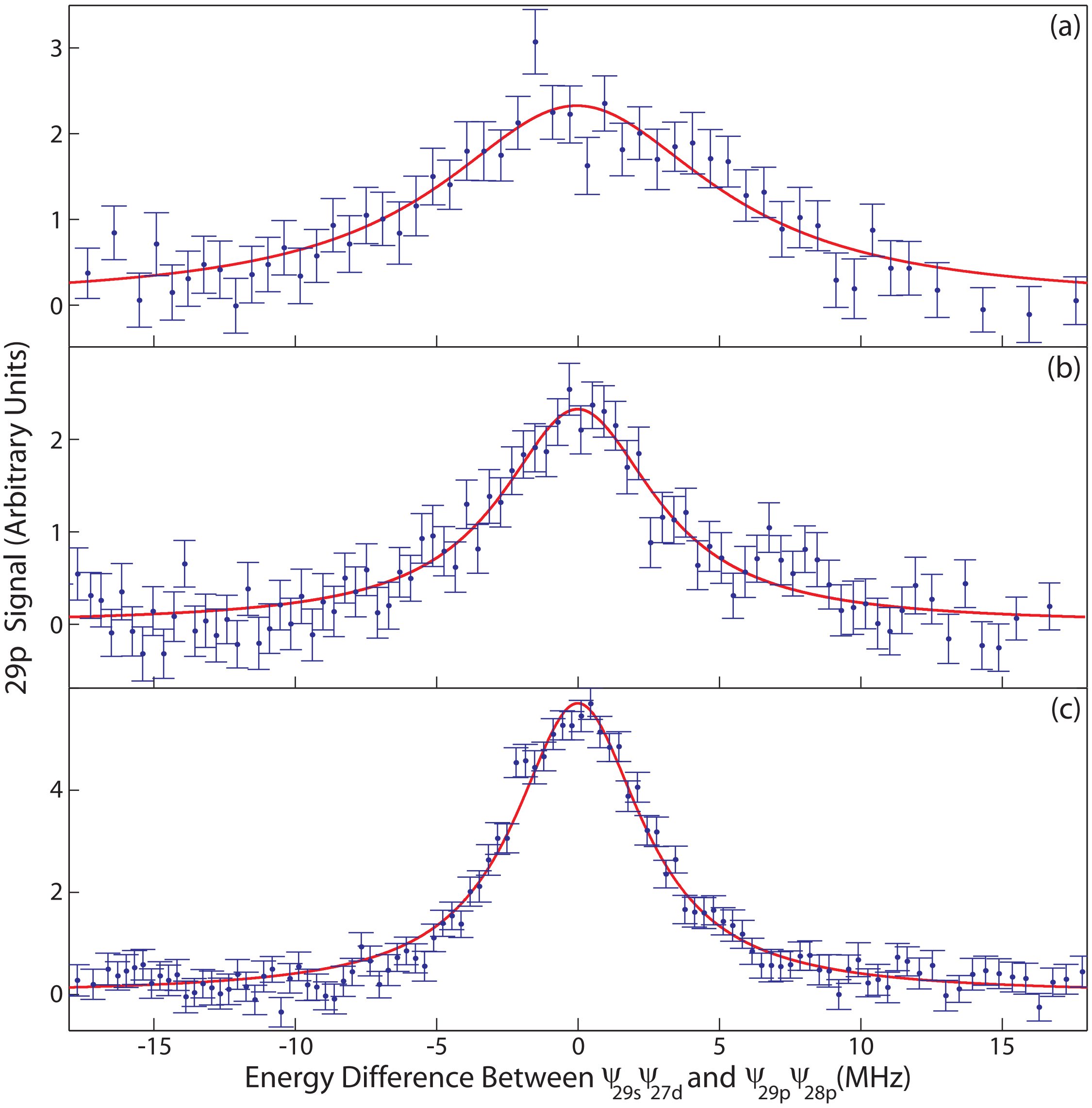

Figure 5.4: Plots of the resonance for different on-resonance times, t_R. The resonance broadens as the on-resonance time is decreased below the transit time of the atoms. In (c) $t_R = 1$ μs is about twice atom transit time for $\bar{v}_c = 40.1$ m/s and the resonance is 5.54 ± 0.17 MHz wide. In (b) $t_R = 200$ ns and the resonance is 6.67 ± 0.57 MHz wide. In (a) $t_R = 100$ ns and the peak is transform broadened to 11.76 ± 1.18 MHz. For all three the blue dots and error bars correspond to the binned data and the red lines are the Lorentzian fits.

5.2 Resonant Dipole-Dipole Energy Transfer

A quantitative understanding of the experimental results can be obtained by considering two interacting Rydberg atoms. In the rest frame of atom 1, atom 2 travels with velocity $\vec{v}$, passing atom 1 at a point of closet approach (or impact parameter) $\vec{b}$ as shown in figure 5.5. Provided the amount of angular momentum in the translational motion is sufficiently large, the deflection of atom 2 due to its interaction with atom 1 can be neglected (ie. when $mv^2/2 \gg V$) [41]. The Hamiltonian for the atom pair is

$$H = H_1 + H_2 + V_p \tag{5.2}$$

where H_1 and H_2 are the Hamiltonians for single atoms in a static electric field and V_p is the atom-atom interaction. Assuming the distance between the atoms, R, is much greater than the diameter of the atoms, V_p can be approximated as a dipole-dipole interaction,

$$V_D = \frac{\vec{r}_1 \cdot \vec{r}_2}{R^3} - \frac{3(\vec{r}_1 \cdot \vec{R})(\vec{r}_2 \cdot \vec{R})}{R^5}. \tag{5.3}$$

where $\vec{r}_1$ and $\vec{r}_2$ are the position of the Rydberg electrons relative to their respective nuclei and $\vec{R}$ is the position of atom 2 relative to atom 1. Following the procedure laid out by Robicheaux *et al.* [103], we define $\hat{z}$ to be parallel to $\vec{R}$, and express the position of the electron on atom j as $\vec{r}_j = x_j\hat{x} + y_j\hat{y} + z_j\hat{z}$. The potential becomes

$$V_D = \frac{x_1x_2 + y_1y_2 - 2z_1z_2}{R^3} = \frac{r_1r_2}{R^3}\left(C^1_{1,1}C^2_{2,-1} + C^1_{1,-1}C^2_{2,1} - 2C^1_{1,0}C^2_{2,0}\right) \tag{5.4}$$

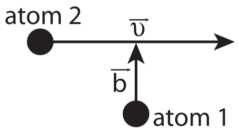

Figure 5.5: Schematic of atom 2 passing atom 1 with a velocity $\vec{v}$ with an impact parameter $\vec{b}$

where $C^j_{k,q}$ is a spherical tensor acting on atom j ($C_{k,q} = \sqrt{4\pi/(2k+1)}Y_{k,q}$ where $Y_{k,q}$ are the spherical harmonics). Ignoring spin, the potential couples each possible initial molecular pair state, $|A_{m_2}\rangle = |29s, m_1 = 0\rangle|27d, m_2\rangle$ where $m_2 = 0$, ± 1, or ± 2, to several degenerate final states, $|F_i\rangle = |29p, m_1'\rangle|28p, m_2'\rangle$ or $|28p, m_1'\rangle|29p, m_2'\rangle$ with one, two or three combinations of m_1' and m_2' for $|m_2| = 2$, 1 or 0 respectively. Diagonalizing the Hamiltonian for a given m_2, reveals that the initial state $|A_{m_2}\rangle$ is coupled to a single final state $|B_{m_2}\rangle$ which is a linear combination of the $|F_i\rangle$ states. The coupling between $|A_{m_2}\rangle$ and $|B_{m_2}\rangle$ is

$$V_{m_2} = \frac{\sqrt{\sum\limits_i |\langle A_{m_2}| V_D |F_i\rangle|^2}}{R^3} . \tag{5.5}$$

Since $\vec{r}_2$ is randomly oriented relative to $\hat{z}$, we average over the five possible values of m_2 to define an average interaction strength

$$V = \frac{1}{5}\sum_{m_2} V_{m_2} = \frac{\mu_1\mu_2}{R^3} . \tag{5.6}$$

The molecular states, $|A\rangle$ and $|B\rangle$, have energies $E_A = E_{29s_{1/2}} + E_{27d_{3/2}}$ and $E_B = E_{29p_{1/2}} + E_{28p_{1/2}}$. In this basis, the waveform of the atomic pair can be written as

$$\Psi(t) = C_A(t)|A\rangle + C_B(t)|B\rangle. \tag{5.7}$$

Applying the time-dependent Schrodinger equation ($H\Psi = i\frac{\partial\Psi}{\partial t}$) yields two coupled differential equations:

$$E_A C_A(t) + V_{AB}(t)C_B(t) + V_{AA}(t)C_A(t) = i\dot{C_A}(t) \tag{5.8a}$$

and

$$E_B C_B(t) + V_{BA}(t)C_A(t) + V_{BB}(t)C_{B(t)} = i\dot{C_B}(t), \tag{5.8b}$$

where $V_{AB}(t)$ is the matrix element of $V(t)$ between two spatial wave functions. Because

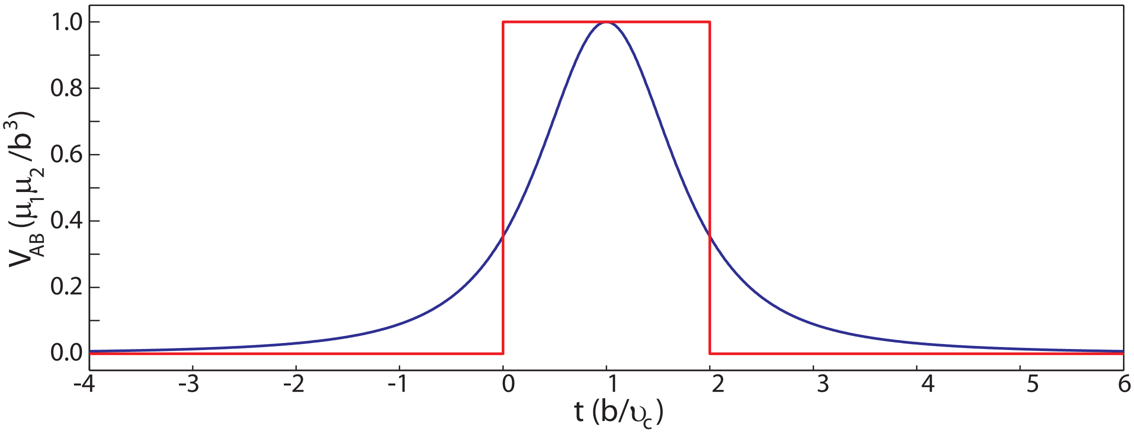

Figure 5.6: Plot of the dipole-dipole potential seen by atom 2 passing atom 1 perpendicular to the electric field (blue) is approximated by a step potential (red) which is $\mu_1\mu_2/b^3$ while $r \leq \sqrt{2}b$ and 0 at all other times.

$V(t)$ is time-dependent, there is not a general analytic solution to these coupled differential equation. However, insight can be gained by making an approximation [41, 104].

Consider $V(t)$ to be a constant while $R \leq \sqrt{2}b$ and 0 at all other times. So,

$$\begin{aligned} &V_{AA} = V_{BB} = 0 \\ &V_{AB} = V_{BA} = V_0 = \frac{\mu_1\mu_2}{b^3} \text{ for } 0 \leq t \leq 2b/\upsilon_c \\ &V_{AB} = V_{BA} = 0 \text{ for } t < 0 \text{ or } t > 2b/\upsilon_c \end{aligned} \tag{5.9}$$

where $t = 0$ when $R = \sqrt{2}b$ for the first time and V_0 is chosen such that the integral over the potential is the same as it is for the dipole-dipole potential where $\vec{\upsilon}$ is perpendicular to the applied electric field. Since the pair is initially in $|A\rangle$, $C_A(t_0) = 1$ and $C_B(t_0) = 0$ for $t_0 < 0$ and equations 5.8a and 5.8b are satisfied for $0 < t < b/\upsilon_c$ by

$$C_A(t) = \left(\cos\Omega t - \frac{i(E_A - E_B)}{2\Omega}\sin\Omega t\right) \tag{5.10a}$$

and

$$C_B(t) = -\frac{\imath V_0}{\Omega}\sin\Omega t, \tag{5.10b}$$

where $\Omega = \sqrt{(E_A - E_B)^2 + 4V_0^2}/2$ [104]. After interacting for a time $t_c \leq b/\upsilon_c$, the probability of finding the system in $|B\rangle$ is given by the standard Rabi formula,

$$P(t_2) = |C_B(t_2)|^2 = \frac{V_0^2}{\Omega^2} \sin^2 \Omega t_c. \tag{5.11}$$

From this expression it is straightforward to derive the basic velocity dependence of the line width by first rewriting the probability in terms of the energy difference between the two states ($E = E_A - E_B$) which is tuned by varying the applied electric field, so

$$P(t_c) = |C_B(t_c)|^2 = \frac{4V_0^2}{E^2 + 4V_0^2} \sin^2 \frac{\sqrt{E^2 + 4V_0^2} t_c}{2} . \tag{5.12}$$

For $t_c \gg 1/V_0$, the sine squared term in equation 5.12 results in a rapid modulation of the Lorentzian lineshape as a function of E. These rapid modulations average out over the experimental ensemble due to the distribution of impact parameters and the associated range of V_0. This yields a cusp-like excitation lineshape with a full width at half maximum of $\Delta E = 4\bar{V}_0$ where $\bar{V}_0$ is the most probable interaction strength for the ensemble. For a random 3D distribution, $\bar{V}_0 \cong 3\pi\mu_1\mu_2\rho$, where ρ is the atom density. Conversely, for $t_c \ll 1/V_0$, the lineshape is broadened in analogy to transit time broadening in laser spectroscopy. The lineshape has the form of a sinc function whose width is independent of $\bar{V}_0$ but inversely proportional to t_c, $\Delta E = \sqrt{32}/t_c$. Simulations show that in the intermediate case, $t_c \sim 1/\bar{V}_0$, the lineshape appears as a modulated cusp. As a result of the modulations, the width is difficult to define. However, the average linewidth is well represented by adding the cusp contribution and sinc contribution in quadrature,

$$\Delta E = 4\sqrt{2/t_c^2 + \bar{V}_0^2}. \tag{5.13}$$

Although this approximation accurately predicts the resonance width, it may not reflect the experimentally observed lineshape which is determined by the shape of the real potential and the velocity distribution of the interacting atoms [41, 65, 104].

In the experiments, the interaction time, t_c, is limited either by the transit time of the interacting atoms or by the duration of the tuning electric field pulse, t_R. The first case, $t_c = 2b/\upsilon_c$, corresponds to the long tuning pulse regime. In order to determine the velocity dependence of the linewidth, we define the optimal impact parameter, b_0, for which the transition probability on-resonance is a maximum ($P = 1$). This implies that the argument of the sine in equation 5.11 is $\pi/2$ on resonance,

$$\frac{4\mu_1\mu_2}{b_0^3}\frac{2b_0}{\upsilon_c} = \frac{\pi}{2}, \tag{5.14}$$

and therefore,

$$b_0^2 = \frac{4\mu_1\mu_2}{\pi\upsilon_c} \tag{5.15}$$

[41, 104]. Atom pairs with $b \sim b_0$ are the predominant contributors to the resonant energy transfer signal. Therefore, in the long pulse regime, the relevant interaction time is $t_c = 2b_0/\upsilon_c$. In contrast to the measurements made in the next chapter where the atoms are nearly frozen in a MOT, for these experiments, $\upsilon_c/2b_0 \gg \bar{V}_0$. Thus, the contribution of "natural" linewidth $\bar{V}_0$ to the resonance lineshape is negligible, so $\Delta E = \sqrt{32}/t_c$.

In the long pulse regime the resonance linewidth can also be expressed in terms of the relative velocity of the Rydberg atoms. Setting $t_c = 2b_0/\upsilon_c$ and substituting for b_0 from equation 5.15 yields,

$$\Delta E = \sqrt{\frac{2\pi}{\mu_1\mu_2}}\upsilon_c^{3/2}. \tag{5.16}$$

Therefore, the linewidth decreases with the relative velocity of the atoms in the beam. The $\upsilon_c^{3/2}$ dependence can also be seen by considering the transition probability directly,

$$P(t) = |C_B(t)|^2 = \frac{4V_0^2}{\Delta E^2 + 4V_0^2}\sin^2\frac{\sqrt{\Delta E^2 + 4V_0^2}b}{2\upsilon_c}. \tag{5.17}$$

The term in front of the sine is a Lorentzian with a width of $4V_0 = 4\mu_1\mu_2/b^3$. The sine term contributes a scaling factor, but does not change the dependence of the line width on b [104]. Substituting for b_0 for b, shows that the line width scales as $\upsilon_c^{3/2}$ [41, 104].

The experiments discussed in this chapter take place in ensembles of atoms with different relative velocities and impact parameters, and therefore in most of the experiments, t_c is limited by υ_c for some atom pairs and by t_R for others. However, the latter case dominates when $t_R \leq 2b_0/\bar{\upsilon}_c$, where $\bar{\upsilon}_c$ is the average relative speed. It is in this short pulse regime that the interactions are termed transformed limited, and all interactions begin and end at the same time. In this case, atom pairs with smaller impact parameters contribute more to the signal, but the transition linewidth for all pairs are identical.

5.3 Relative Velocity Reduction Via Thermal Expansion

As shown in the previous section, the observed widths of the resonances are dependent on the relative velocities of the colliding atoms. In the experiments, the atoms interact with a range of velocities. Therefore, the most accurate way to simulate the measurements is to use the relative velocity distribution within the beam and compute a weighted average of the transition probabilities for the different relative velocities within the experimental sample. However, for computing the resonance linewidths, it is sufficiently accurate to use the average relative speed, $\bar{\upsilon}_c$ and equation 5.16 [104]. Nevertheless, the relative velocity distribution must be determined to find $\bar{\upsilon}_c$. For an effusive thermal beam, the velocity distribution in the beam direction is

$$\Phi(\upsilon) = \frac{\upsilon^3}{2}\left(\frac{m}{kT}\right)^2 e^{-\frac{m\upsilon^2}{2kT}} \tag{5.18}$$

which is normalized so $\int_0^\infty \Phi(\upsilon)d\upsilon = 1$ and where m is the atomic mass, k is Boltzmann's constant, and T is the temperature of the beam [64, 65]. The relative velocity distribution is the autocorrelation of $\Phi(v)$,

$$\Phi(v_R) = \int_0^\infty \Phi(v)\Phi(v+v_R)dv = \frac{1}{4}\left(\frac{m}{kT}\right)^4 \int_0^\infty v^3(v+v_R)^3 e^{-\frac{m}{2kT}\left(v^2+(v+v_R)^2\right)}dv. \quad (5.19)$$

Integration yields a complicated function which is well approximated in a simpler analytic form by the velocity distribution of a one dimensional ideal gas at a temperature $T' = T/1.08$,

$$\Phi(v_R) \cong \sqrt{\frac{m}{2\pi kT'}}e^{-\frac{mv_R^2}{2kT'}}. \quad (5.20)$$

Clearly, the average relative velocity is zero, however we are really interested in the average relative speed, $\bar{v}_c$,

$$\bar{v}_c = \frac{\int_{-\infty}^{\infty}\Phi(v_R)|v_R|dv_R}{\int_{-\infty}^{\infty}\Phi(v_R)dv_R} \approx \sqrt{\frac{2kT'}{\pi m}}. \quad (5.21)$$

To reduce $\bar{v}_c$, the exciting lasers are focused into the potassium beam as shown in figure 5.1. As the cylinder of excited atoms expands along the direction of the beam, the relative velocity distribution of neighboring Rydberg atoms narrows, effectively cooling them. The atoms initial spatial distribution along the beam reflects the laser profile along that coordinate. Assuming a Gaussian distribution,

$$\mathbb{D}(x,\tau=0) = \mathbb{D}_0(x) = \frac{1}{\sqrt{\pi}d}e^{-\frac{x^2}{d^2}} \quad (5.22)$$

where the laser spot size, $d_0 = 2\sqrt{\ln 2}d$, is the full width at half the maximum of the distribution. The distribution is normalized such that $\int_{-\infty}^{\infty}\mathbb{D}(x,\tau=0)dx = 1$. After a time τ, the probability of finding an atom at position x with velocity v is

$$\mathbb{P}(x,v,\tau) = \Phi(v)\mathbb{D}_0(x-v\tau). \quad (5.23)$$

The probability that two atoms with relative velocity $v_R = v_1 - v_2$ are within an interaction distance $\Delta x = x_1 - x_2$ of each other at a time τ is

$$\mathbb{P}(\Delta x, \upsilon_R, \tau) = \int_{\infty}^{\infty} dx_1 \int_0^{\infty} d\upsilon_1 \mathbb{P}(x_1, \upsilon_1, \tau)\mathbb{P}(x_2 = x_1 + \Delta x, \upsilon_2 = \upsilon_1 + \upsilon_R, \tau). \tag{5.24}$$

Integrating $\mathbb{P}(\Delta x, \upsilon_R, \tau)$ over the values of Δx for which interactions occur gives the probability of an atomic pair capable of interacting having a relative velocity υ_R. In these experiments, the distance over which interactions can occur ($\Delta x \sim b_0$) is much smaller than the distance the atoms travel in the time τ. Therefore, integrating over Δx from $-b_0/2$ to $b_0/2$ is equivalent to setting $\Delta x = 0$ and multiplying by b_0, so

$$\mathbb{P}(\upsilon_R, \tau) = b_0 \int_{\infty}^{\infty} dx_1 \int_0^{\infty} d\upsilon_1 \mathbb{D}_0(x_1 - \upsilon_1 \tau)\mathbb{D}_0\left(x_1 - (\upsilon_1 + \upsilon_R)\tau\right) \Phi(\upsilon_1)\Phi(\upsilon_1 + \upsilon_R). \tag{5.25}$$

Integrating over x_1, leaves

$$\mathbb{P}(\upsilon_R, \tau) = \frac{1}{d}\frac{b_0^2}{\sqrt{2\pi}} e^{-\frac{\Delta\upsilon^2\tau^2}{2d^2}} \int_0^{\infty} \Phi(\upsilon_1)\Phi(\upsilon_1 + \Delta\upsilon) d\upsilon_{1,} \tag{5.26}$$

where the remaining integral is the same autocorrelation function as equation 5.19. Therefore, making the same approximation as that in equation 5.20,

$$\mathbb{P}(\upsilon_R, \tau) \cong \frac{1}{2\pi d}\sqrt{\frac{b_0^2 m}{kT'}} e^{-\left(\frac{m}{2kT'} + \frac{\tau^2}{2d^2}\right)\upsilon_R^2}. \tag{5.27}$$

This can be readily expressed in terms of an effective temperature as

$$\Phi(\upsilon_R, \tau) \approx \sqrt{\frac{m}{2\pi k T_{eff}}} e^{-\frac{m\vec{\upsilon}_R^2}{2kT_{eff}}} \tag{5.28}$$

where

$$T_{eff} = \frac{T'}{1 + \frac{kT'\tau^2}{md^2}}. \tag{5.29}$$

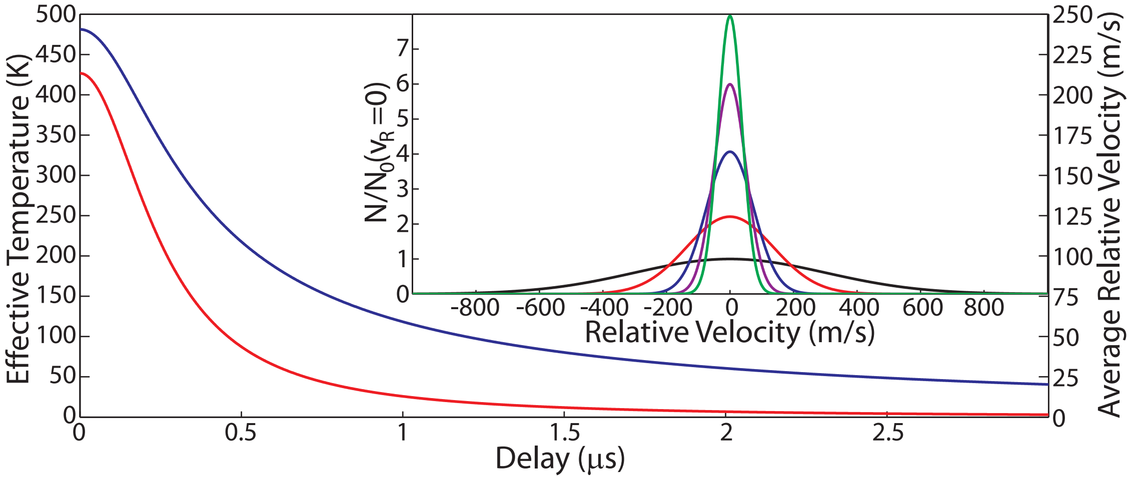

Figure 5.7: Plot of the reduction in the average relative speed of the interacting atoms as the interaction time is delayed. The red line shows the reduction in the effective temperature and the blue line shows the reduction in the average relative speed as a function delay. The insert shows the relative velocity immediately following excitation (black), after 0.5 μs (red), 1 μs (blue), 1.5 μs (purple) and 2 μs(green).

Accordingly, the average relative speed is reduced to

$$\bar{v}_c = \sqrt{\frac{2kT_{eff}}{\pi m}}\ . \tag{5.30}$$

Figure 5.7 shows the decline in the average relative velocity and in effective temperature as a function of delay. This can also be seen in the narrowing of the relative velocity distribution shown in the insert.

5.4 Rydberg Density Reduction During Thermal Expansion

Although this technique is an effective method of reducing the average relative velocity, it has the side effect of reducing the Rydberg atom density (ρ) as shown in figure 5.8. The spatial distribution at a time τ is found by integrating $\mathbb{P}(x, v, \tau)$ (equation 5.23) over v. This integral cannot be done in closed form. However, by taking advantage of the same approximate form for the autocorrelation of the velocity distribution of the atomic beam, we can derive an accurate closed form expression for the delay-dependent Rydberg spatial distribution function,

$$\mathbb{D}(x,\tau) \cong \frac{1}{\sqrt{\pi}d(\tau)} e^{-\frac{(x-\upsilon_{mp}\tau)^2}{d(\tau)^2}} \tag{5.31}$$

where $\upsilon_{mp} = \sqrt{3kT/m}$ is the most probable velocity in the atomic beam and where $d(\tau) = \sqrt{d_0^2 + \upsilon_{wide}^2\tau^2}/2\sqrt{\ln 2}$, $\upsilon_{wide} = \sqrt{8kT/3m}$ is the full width at half the maximum of the beam's velocity distribution. Qualitatively this is what we should expect. The center of the Rydberg distribution moves at the peak speed of the velocity distribution. At short delays, $\tau \ll d_0/\upsilon_{wide}$, the spatial distribution remains unchanged. However, for long delays, $\tau \gg d_0/\upsilon_{wide}$, the spatial distribution spreads at a rate which is proportional to the width of the velocity distribution. At intermediate delays, the extent of the distribution is given by the initial width and the width due to the velocity spread added in quadrature. Assuming there is no transverse spreading of the beam, the Rydberg density drops in inverse proportion to $d(\tau)$,

$$\rho(\tau) = \frac{d_0\rho_0}{\sqrt{d_0^2 + \upsilon_{wide}^2\tau^2}} = \frac{\rho_0}{\sqrt{1 + \upsilon_{wide}^2\tau^2/d_0^2}} \tag{5.32}$$

where ρ_0 is the initial Rydberg density.

Figure 5.8(a) shows the results of numerical integration for different delays τ given the experimental parameters. The numerical results are indistinguishable from those obtained from the approximate closed form expression. The blue curve in figure 5.8(b) shows how the width of the spacial distribution changes with τ. Again the numerical and analytic results are indistinguishable.

5.5 Dependence of Resonant Energy Transfer on Rydberg Atom Density

The delay dependent decrease in the Rydberg density is shown by the green line in figure 5.8(b). This density reduction is undesirable because the resonant energy transfer probability per atom pair depends linearly on the density. This dependence can be un-

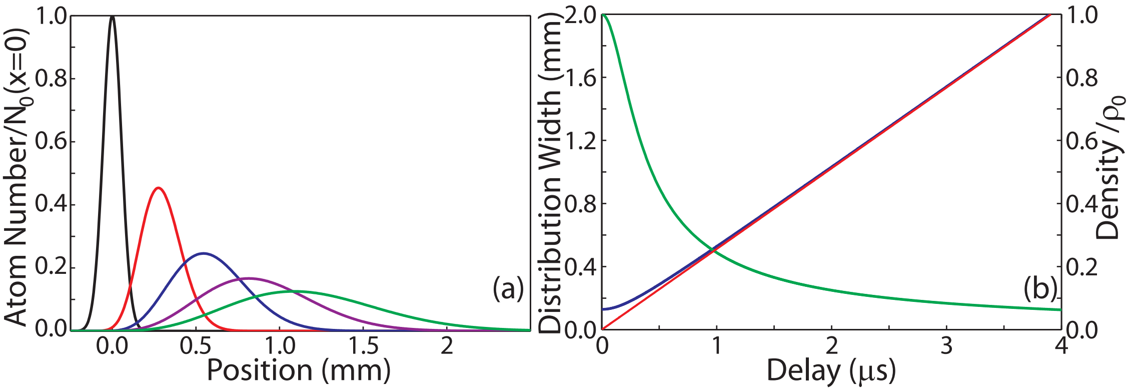

Figure 5.8: Plots showing the decrease in the Rydberg atom density as the interaction time is delayed. (a) The spatial distributions at excitation (black), after 0.5 μs (red), 1 μs (blue), 1.5 μs (purple) and 2 μs (green) for the experimental parameters (T = 460.8 K, d_0 = .129 mm). The peak of the distribution moves with the most probably velocity of the beam velocity distribution, $\upsilon_{mp} = \sqrt{3kT/m}$. (b) The width of the distribution (blue) expands linearly at a rate of υ_{wide} after about 0.5 μs. The red line has a slope equal to the width of the velocity distribution of the beam $\upsilon_{wide} = \sqrt{8kT/3m}$. The green line shows the drop in the density as a function of delay where we assume that the density is proportional to the number of atoms divided by the width of the distribution (ie. there is no significant expansion in the transverse directions).

derstood by considering the on-resonance transition probability. On resonance, in the long pulse regime,

$$P\left(t_c = \frac{2b}{\upsilon_c}\right) = \sin^2\left(\frac{2\mu_1\mu 2}{\upsilon_c b}\right). \tag{5.33}$$

The average transition probability is then

$$\langle P\rangle = \int_{-\infty}^{\infty} d\upsilon_c \int_0^{\infty} dbP(t_c = 2b/\upsilon_c)\Phi(\vec{\upsilon}_c)\mathbb{G}(b) \tag{5.34}$$

where $\Phi(\vec{\upsilon}_c)$ is the relative velocity distribution from equation 5.28 and $\mathbb{G}(b)$ is the nearest neighbor distribution for the ensemble,

$$\mathbb{G}(R) = 4\pi\rho R^2 e^{-\frac{4}{3}\pi\rho R^3}. \tag{5.35}$$

The integral in equation 5.34 cannot be done analytically, but insight is gained by making the following approximation. First, we set

$$\begin{aligned} P\left(t_c = \frac{2b}{v_c}\right) &= \frac{1}{2} \text{ for } b < b_1 = 2\sqrt{\frac{2\mu_1\mu_2}{v_c}} \\ P\left(t_c = \frac{2b}{v_c}\right) &= 0 \text{ for } b > b_1. \end{aligned} \tag{5.36}$$

This approximation is reasonable because the sine term oscillates about an average value of 1/2 for $|2\mu_1\mu_2/v_c b| > 1$ and drops rapidly to zero for $|2\mu_1\mu_2/v_c b| < 1$. Therefore,

$$\langle P\rangle = \frac{1}{2}\int_{-\infty}^{\infty} dv_c \int_0^{b_1} db\Phi(\vec{v}_c)\mathbb{G}(b) = \frac{1}{2}\left(1 - \int_{-\infty}^{\infty} \Phi(\vec{v}_c) e^{-\frac{4\pi\rho}{3}\left|\frac{2\mu_1\mu_2}{v_c}\right|^{3/2}} dv_c\right). \tag{5.37}$$

Approximating the exponential term as a box where

$$e^{-\frac{4\pi\rho}{3}\left|\frac{2\mu_1\mu_2}{v_c}\right|^{3/2}} = 1 \text{ for } \frac{4\pi\rho}{3}\left|\frac{2\mu_1\mu_2}{v_c}\right|^{3/2} < 1 \tag{5.38a}$$

$$e^{-\frac{4\pi\rho}{3}\left|\frac{2\mu_1\mu_2}{v_c}\right|^{3/2}} = 0 \text{ for } \frac{4\pi\rho}{3}\left|\frac{2\mu_1\mu_2}{v_c}\right|^{3/2} > 1, \tag{5.38b}$$

the average transition probability becomes

$$\langle P\rangle = \frac{1}{2}\int_{-v_0}^{v_0} \Phi(v_c) dv_c \tag{5.39}$$

where $v_0 = 2\mu_1\mu_2(4\pi\rho/3)^{2/3}$. When $v_0 \gg v_{rms} \sim 1.2\sqrt{kT_{eff}/m}$, $\langle P\rangle \cong 1/2$, while $\langle P\rangle \cong v_0\sqrt{m/2\pi kT_{eff}}$ when $v_0 \ll 1.2\sqrt{kT_{eff}/m}$ as is the case in these experiments ($1.2v_{rms}$ is the half width of the velocity distribution). To find the transition probability for an on-resonance time t_R, the average probability is multiplied by the number of interactions per atom during the time t_R. This factor is equal to the distance traveled by the atoms in a time t_R divided by the separation between the atoms. So the transition probability per atom pair is

$$P(t_R) = \langle P\rangle \frac{v_{rms}t_R}{(2\pi\rho)^{1/3}} = 2\sqrt{2\pi}\left(\frac{2}{3}\right)^{2/3} \rho\mu_1\mu_2 t_R. \tag{5.40}$$

The number of pairs making a transition (N_c) during the time t_R is

$$N_c = N_{Ryd} 2\sqrt{2\pi} \left(\frac{2}{3}\right)^{2/3} \rho \mu_1 \mu_2 t_R \approx 3.8 N_{Ryd} \rho \mu_1 \mu_2 t_R, \tag{5.41}$$

where N_{Ryd} is the number of Rydberg atoms originally in either the $29s$ or $27d$ state. This approximation is consistent with the result obtained from considering the energy exchange process as a collision [41] where

$$N_c = N_{Ryd} \rho \sigma \bar{v}_c t_R \approx 4 N_{Ryd} \rho \mu_1 \mu_2 t_R. \tag{5.42}$$

In deriving equation 5.42, we assume that the cross section $\sigma \approx \pi b_0^2 = 4\mu_1\mu_2/\bar{v}_c$ where b_0 is defined by equation 5.15.

5.6 Extracting Delay Dependent Beam Temperature and Density from Long Pulse Data

No direct measurement was made of the oven temperature or beam density and measurements of the laser spot size were inconsistent. However, these numbers can be determined as fit parameters to the data, and are shown to be self consistent. First, we use Numerov integration to compute the radial matrix elements between the states and angular momentum algebra to calculate $\mu_1\mu_2 = 4.9 \times 10^5$ atomic units in equation 5.6. The approximate spotsize is determined by fitting the delay dependence of the resonance widths (figure 5.9) to a function which adds the homogeneous (ΔE_h) and inhomogeneous widths (ΔE_i) as for a Voigt profile

$$\Delta E = \Delta E_h/2 + \sqrt{\Delta E_h^2/4 + \Delta E_i^2}. \tag{5.43}$$

To account for the change in relative velocity during the one microsecond on-resonance time, we average the homogeneous widths,

$$\Delta E_h = \frac{\sum_n \frac{\Delta E_h(\tau+n\Delta t_{step})}{\sqrt{d_0^2+v_{wide}^2(\tau+n\Delta t_{step})^2}}}{\sum_n \frac{1}{\sqrt{d_0^2+v_{wide}^2(\tau+n\Delta t_{step})^2}}} \tag{5.44}$$

where ΔE_h is given by equation 5.16, $n = 0$ to 1000 and $\Delta t_{step} = 1$ ns. The fit parameters are the spotsize, $d_0 = 2\sqrt{\ln 2}d$, and the inhomogeneous width ΔE_i. For time delays $\tau > 500$ ns, the effective temperature, relative velocities and resonance width are nearly independent of the initial oven temperature and depend primarily instead upon d_0 and τ. We find $d_0 \simeq 128 \pm 3$ μm and $\Delta E_i \simeq 4.5$ MHz ±50 kHz over the range of likely oven temperatures (T=400 K to 600 K). This values for d_0 is then used to estimate the initial beam density and oven temperature.

The beam density and oven temperature are determined by fitting the decrease in the fraction of atom pairs in the $29p28p$ state according to equation 5.41. It is first necessary to determine the fraction of the excitation volume in which the lasers are overlapped, as some Rydberg signal is likely coming from a volume where only $27d$ or $29s$ Rydberg atoms are present, and where no energy transfer occurs. To accomplish this, the thermal resonance at zero delay is fit with cusp on a constant background having the form

$$S_c = \frac{Qa}{2}\left(Ci(a)\sin(a) + \left(\frac{\pi}{2} - Si(a)\right)\cos(a)\right) + y_{off} \tag{5.45}$$

where $a = A/(E - E_{off})$, E is the spacing between the $29s27d$ and $29p28p$ molecular states, S_c is the signal in the $29p$ state, A, E_{off}, Q and y_{off} are fit parameters determining the width, peak position, height and baseline respectively and where

$$Si(z) = \int_0^z \frac{\sin t}{t}dt \tag{5.46a}$$

$$Ci(z) = \gamma + \ln z + \int_0^z \frac{\cos t - 1}{t}dt \text{ where } |\arg z| < \pi \tag{5.46b}$$

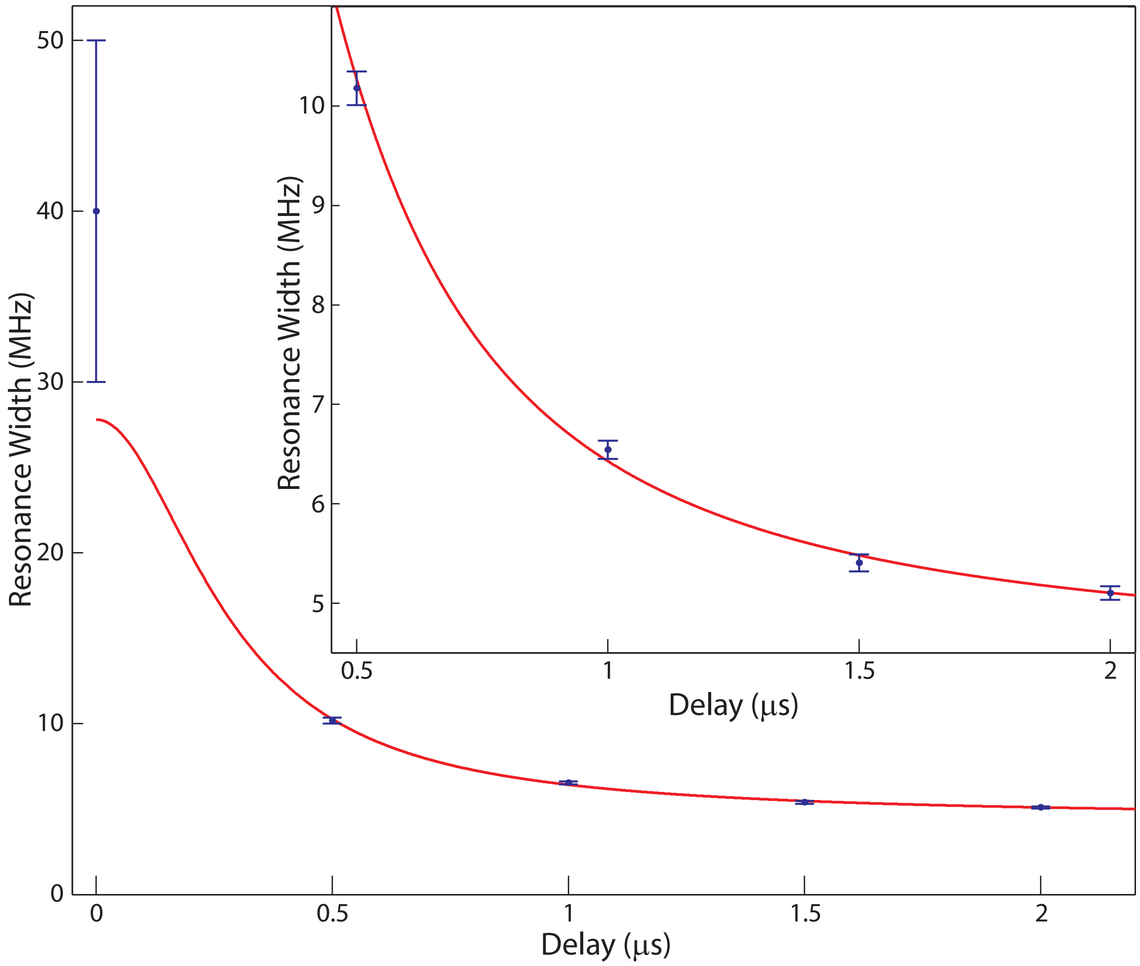

Figure 5.9: Plot of the decrease in the width of the resonance as the average relative speed between the atoms is reduced. The points are the widths of the fits to the resonances shown in figure 5.3. The insert shows an enlarged view of points for the relative velocity-reduced resonances. In both, the red line marks the least squared fit to the widths assuming the spatial distribution is expanding according to equation 5.32 where the laser spotsize, d_0, and the inhomogeneous width, ΔE_i, are parameters of the fit. For a temperature of 461 K, the fit gives $d_0 = 129$ μm and $\Delta E_i = 4.45$ MHz. At a delay of 2 μs, velocity reduction scheme has reduced the average relative velocity from $\bar{v}_c = \sqrt{2kT'/\pi m} = 240.6$ m/s to 30.3 m/s (corresponding to an effective temperature of 7 K).

as defined by Abramowitz and Stegun [105]. This function describes the cusp lineshape for resonant dipole-dipole interactions in a frozen Rydberg gas, similar to that predicted for resonant energy transfer in a beam [65, 106]. We assume that the thermal resonance is saturated at its peak because increasing the on-resonance time does not change the peak height. At saturation, in the region of overlap a quarter of the Rydberg atoms are in each of the four state, $29s$, $27d$, $29p$ and $28p$. Therefore at the peak of the resonance, we define the $S_c = S_o/4$ where S_c is the $29p$ signal and S_o is the total Rydberg signal from *the region of overlap* where both $29s$ and $27d$ Rydberg atoms are present. However, on resonance we measure $S_c/S_T = 0.15$, where $S_T = S_o + S_n$ is the total Rydberg signal and S_n is the signal due to $29s$ and $27d$ Rydberg atoms outside the volume where the three lasers are overlapped. Substituting for S_c and S_T,

$$\frac{1/4S_o}{(S_o + S_n)} = .15 \text{ or } S_n = \frac{2}{3}S_o. \tag{5.47}$$

Thus, $S_o = 3/5S_T$ and the transition probability is given by the measured values

$$P = \frac{S_c}{0.3S_T} \tag{5.48}$$

for any delay or detuning from resonance.

With this calibration, we can fit the decrease in the height of the resonance peaks using equation 5.41 and can determine the initial Rydberg density and oven temperature. The density of atoms in an effusive beam a distance L directly in front of the hole the oven is

$$\rho_{atom} = 1.118 \times 10^{24} \frac{pA_o}{L^2\sqrt{MT}\upsilon_{ave}} \text{ cm}^{-3} \tag{5.49}$$

where p is the pressure inside the oven in torr, $A_o = .002$ cm^2 is the area of the hole in the oven, $L = 26$ cm, $\upsilon_{ave} = 3/4\sqrt{2\pi kT/m}$ is the average beam velocity in m/s, $M = 39$ is the atomic weight and T is the absolute temperature of the oven in Kelvin [66, 67]. The vapor pressure p as a function of temperature is found using reference [107]. Assuming all three dye lasers saturate their respective transitions, the density of Rydberg atoms in each of the two initial states is one quarter of the total atomic density. Equation 5.49 gives a temperature-dependent single-state Rydberg density in the temperature range of interest,

$$\rho_0 = e^{-1.3422e5/T^2 - 9432/T + 38.839}. \tag{5.50}$$

Using this expression and equation 5.41 we find an expression for the fraction of atomic pairs in the $29p28p$ state from the overlap region,

$$P = \sum_n \frac{3.8\rho_0\mu_1\mu_2}{\sqrt{1 + \frac{v_{wide}^2(\tau + n\Delta t_{step})^2}{d_0^2}}} \tag{5.51}$$

as long as $P \ll 1/2$. This expression breaks down as the system approaches saturation (ie. $P = 1/2$) because, in the incoherent ensemble, additional interactions are as likely to drive population back into the initial $29s27d$ state as they are to drive population into the $29p28p$ state. Fitting equation 5.51 to the data points shown in figure 5.10, gives a temperature of 460.8 K. Using this temperature to fit the decline in the resonance widths provides small corrections to the initial estimates of d_0 and ΔE_i. Specifically we find $d_0 = 129$ μm and $\Delta E_i = 4.45$ MHz.

5.7 Analysis

Figure 5.9 shows good agreement between the fit and the measured widths for the velocity reduced resonances. This indicates that our assumption that $\bar{V}_0$ does not contribute substantially to the width is reasonable. Indeed, at the initial density, $\rho_0 = 5.05 \times 10^7$ cm^{-3}, $4\bar{V}_0 = 608$ kHz while for the thermal velocity ($\bar{v}_c = 241$ m/s), $\sqrt{32}/t_c = 27.1$ MHz. This is true for all of the reduced velocities considered here. For example, at the maximum delay of 2 μs, $\rho = 8.32 \times 10^6$ cm^{-3} and $4\bar{V}_0 = 20$ kHz while $\sqrt{32}/t_c = 1.23$ MHz ($\bar{v}_c = 30.3$ m/s).

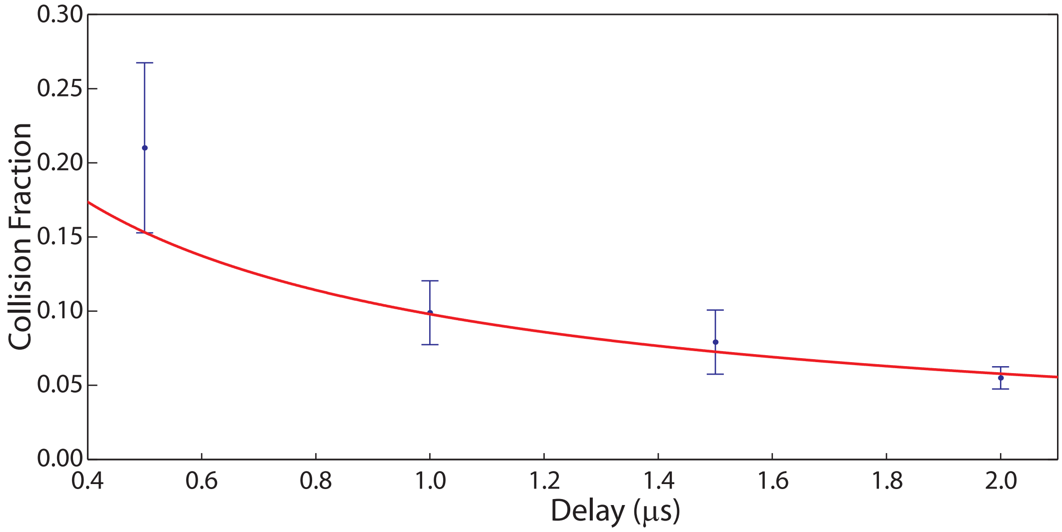

Figure 5.10: Plot of the decrease in the transition probability with the density. The blue points are the transition probabilities ($P(\tau)$) at different delays. The red line is the least squared fit of equation 5.41 to the data where the fit parameter $T = 460.8$ K corresponds to an initial density of $\rho_0 = 5.05 \times 10^7$ cm^{-3}.

The predicted width of thermal resonance ($\Delta E = 28$ MHz for $\bar{v}_c = 241$ m/s) in figure 5.9 is less than the measured width. This likely results from the resonant energy transfer being saturated on-resonance as we assumed for the probability calibration.

The fit suggests that an inhomogeneous broadening of 4.45 MHz is incorporated in the resonance widths. The majority of the inhomogeneous width is likely due to inhomogeneity in the electric field. This level of broadening corresponds to a field inhomogeneity of 141 mV/cm which is not unreasonable. The small field plate separation (0.635 cm) magnifies the effects of patch fields and inhomogeneity due to the extraction slit as compared to the electric field homogeneity of the experiments in chapters 3 and 4. The electric field homogeneity is further degraded by the tendency of the potassium to stick to the field plates. Although the plates were coated with a graphite film lubricant (Aerodag G) to reduce the effect of the potassium coating, it is likely that the field homogeneity is somewhat compromised. Hyperfine structure contributes only slightly to the inhomogeneous broadening. The $29s_{1/2}$ state is split by 270 kHz, while the $29p_{1/2}$ and $28p_{1/2}$ states have hyperfine splittings of 200 kHz and 220 kHz respectively and the 27d$_{3/2}$ state is split by 30 kHz [93]. Stray magnetic fields do not likely contribute to the inhomogeneous broadening. The interaction region is surrounded by a μ-metal shield similar to that which is used in the experiments discussed in chapters 3 and 4. Results from those experiments indicate that the μ-metal shield reduced the magnetic field in the interaction region to less than 100 mGauss. Without the μ-metal shield, the magnetic field in the interaction region is sufficiently large to mix the angular momentum eigenstates so that when the tuning pulse is delayed a second peak appears at about 8 V/cm corresponding to the resonance for $29s_{1/2}+27d_{5/2} \rightarrow 29p_{1/2}+28p_{1/2}$. This second peak is eliminated by the magnetic shield.

Figure 5.11 shows the broadening of the resonance as the time on-resonance (t_R) is reduced below the average transit time of the atoms, $4\sqrt{\mu_1\mu_2/\pi\bar{v}_c}^{-3/2} = 488$ ns at 1.5 μs delay, and $t_c = t_R$. The data for $t_R \gg 488$ ns shows good agreement with the expected width for $t_c = 4\sqrt{\mu_1\mu_2/\pi\bar{v}_c}^{-3/2}$ (green line). As expected for $t_R \ll 488$ ns, the data shows good agreement with $t_c = t_R$. It is in this short pulse regime where the interactions are termed transform limited. All interactions begin and end at the same time. Therefore, the coherence can be exploited and the interactions can be perturbed in a predictable way [100, 101]. The small size of the signal at the low Rydberg densities and short interaction times necessary to achieve transform limited interactions made perusing further investigations with this system impractical, and we moved on to investigate resonant energy transfer in a magneto-optical trap as described in the following chapter.

The issue of the small signal size could be remedied in future implementations of this experiment by moving the interaction region closer to the oven where the atomic beam density would be greater. It would also be extremely desirable to use a different style of oven. Potassium has a tendency to spray liquid metal into the hole that should allow the vapor to effuse from the oven, resulting in a very unstable beam density. Once this occurs, the oven must be replaced. D. S. Thomson and M. J. Renn used an oven composed of a main cylinder body with a small tube as the gas outlet. The tube helped collimate the atomic

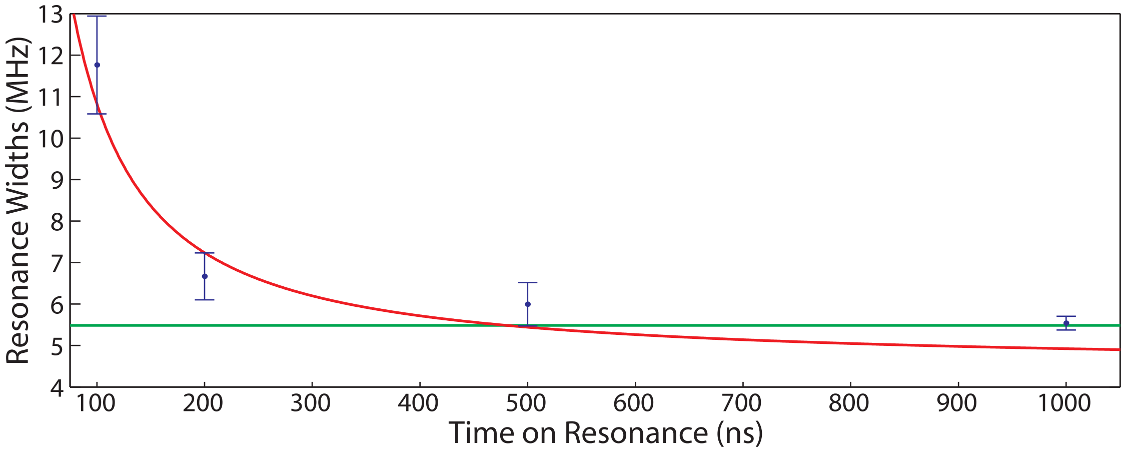

Figure 5.11: Plot of the increase in the resonance widths as the on-resonance time is reduced below the atom transit time. The blue points are the widths of the fits to the resonances shown in figure 5.4. The green line marks the predicted widths in the long pulse regime for $t_c = 4\sqrt{\mu_1\mu_2/\pi}\bar{v}_c^{-3/2} = 488$. The red line marks the predicted widths in the short pulse regime where $t_c = t_R$. As expected in accordance with the uncertainty principle, the resonance broadens as the time on-resonance is reduced below the average transit time of the atoms.

beam and prevented the liquid metal from obstructing the flow of the beam [100, 101, 104]. Such an oven can be run at a higher temperature without clogging, resulting in a denser atomic beam. It would also be desirable to use a larger voltage pulse to tune the interaction. This would allow for the plate separation to be increased which should reduce the field inhomogeneity and decrease the inhomogeneous broadening. The search for a source of larger voltage pulses which are sufficiently flat on the time scale of 100 ns proved futile when this experiment was ongoing, but the lab has since acquired an amplifier from Avtech Electro Systems which is able to amplify pulses from the AWG up to 10 Vpp.

Despite these difficulties, this technique offers a straightforward method for achieving transform limited interactions. Moreover, if used in conjunction with a supersonic expansion effective temperatures well below 1 K might be produced. In general, the method might be effective for studying interactions between cold atoms or molecules excited to metastable or stable neutral or ionic states.

Chapter 6

The Coherence of Resonant Energy Exchange in a Nearly Frozen Rydberg Gas

Proposals to use dipole-dipole interactions between cold Rydberg atoms for quantum information processing [42, 45] have generated considerable interest in understanding coherence in these systems. Coherence in cold Rydberg gasses has been modeled theoretically [108, 109], and echo sequences for measuring dephasing and decoherence have been proposed [40]. Dephasing rates have been measured using Ramsey interference [110] and rotary echo techniques [38, 39]. This chapter discusses a novel technique for measuring the coherence of resonant dipole-dipole energy exchange that allows us to confirm coherence over times much longer than those previously measured for dipole-dipole processes in a cold Rydberg gas [38, 39, 110].

We focus on the resonance in which a $25s_{1/2}$ Rydberg atom dexcites to the $24p_{1/2}$ state giving energy to a $33s_{1/2}$ atom which is excited to the $34p_{3/2}$ state ($25s_{1/2} + 33s_{1/2} \rightarrow 24p_{1/2} + 34p_{3/2}$). This resonant energy transfer process was first investigated by Anderson, Veale and Gallagher in 1998 [111]. Two resonances occur for different values of $|m_j|$, at an electric field of 3 V/cm for $|m_j| = 1/2$ and 3.4 V/cm for $|m_j| = 3/2$. In a cold Rydberg gas, an atom pair in dipole-dipole resonance can, in principle, oscillate many times between the coupled $25s33s$ and $24p34p$ configurations before moving out of interaction range. Therefore, we are in the regime where the transition probability of the pair is dictated by the interatomic spacing rather than by the relative atom velocity, as was the case in the beam experiments discussed in the previous chapter. The widths initially observed by Anderson, Veale and Gallagher [111] as well as those in a follow up investigation [110] were more than an order of magnitude larger than they had predicted for binary energy exchange. They proposed that this discrepancy was due to many-body effects in which the p character from a pair of atoms undergoing the $25s_{1/2} + 33s_{1/2} \rightarrow 24p_{1/2} + 34p_{3/2}$ interaction moves to other neighboring atoms via the always-resonant energy exchange processes $24p_{1/2} + 25s_{1/2} \rightarrow 25s_{1/2} + 24p_{1/2}$ and $34p_{3/2} + 33s_{1/2} \rightarrow 33s_{1/2} + 34p_{3/2}$ [111]. A similar many-body process was suspected of causing broadening of analogous dipole-dipole energy exchange resonances of cesium [112].

In 2004, Mourachko, Li and Gallagher [113] proved that many-body effects can play an important role in Rydberg-Rydberg interactions by introducing $34s_{1/2}$ atoms into a cold Rydberg gas where the $25s_{1/2} + 33s_{1/2} \rightarrow 24p_{1/2} + 34p_{3/2}$ energy exchange process was enabled. The $34s_{1/2}$ atoms are strongly coupled to the $34p_{3/2}$ atoms via the always-resonant energy exchange process $34s_{1/2} + 34p_{3/2} \rightarrow 34p_{3/2} + 34s_{1/2}$. They found that the $25s_{1/2} + 33s_{1/2} \rightarrow 24p_{1/2} + 34p_{3/2}$ resonances broadened as the $34s_{1/2}$ density was increased, indicating that many-body interactions can indeed affect the resonant two-body interaction [113].

In 2002, Anderson *et al.* [110] probed the effect of many-body interactions on resonant energy exchange using a Ramsey interference technique. The $25s_{1/2}+33s_{1/2} \rightarrow 24p_{1/2}+34p_{3/2}$ coupling was tuned to resonance for a short time, t_r, detuned for a variable time, T_r and then tuned back onto resonance for a second short time, t_r. The probability amplitude transferred to the $24p34p$ molecular state during the first on-resonance time interfered with that which was transferred during the second interaction period. Whether this interference was constructive or destructive depended on the phase acquired off-resonance, resulting in oscillations in the population of the $24p34p$ state. The decay in the oscillation amplitude reflects the loss of macroscopic phase coherence between the $25s33s$ and $24p34p$ contributions to the pair states over the ensemble. Their measurements found typical dephasing times on the order of 100 ns and were inversely proportional to the Rydberg atom density. This dephasing was attributed to many-body effects, primarily the always resonant $25s_{1/2} + 24p_{1/2} \rightarrow 24p_{1/2} + 25s_{1/2}$ hopping interaction. [110].

These previous measurements do not directly address the coherence of the $25s_{1/2} + 33s_{1/2} \rightarrow 24p_{1/2} + 34p_{3/2}$ interaction between individual pairs of atoms. To probe this coherence, we have developed a novel time domain spectroscopic technique. Like the Ramsey method, this technique involves two interaction periods of equal duration. Specifically, following laser excitation, an electric field step tunes the atoms to one wing of the resonance profile for a time $t_e/2$. A second field step then rapidly shifts the system to a detuning that is equidistant on the other side of the resonance, where the atoms remain for an equivalent time, $t_e/2$. As long as coherence is maintained, the time and energy separated interactions lead to an enhancement in the $24p34p$ signal as compared to that resulting from remaining on either side of the resonance for the total time t_e. We find that the enhancement persists for more than 10 μs indicating that the atoms remain coherent for times which are much longer than the previously measured dephasing times in cold Rydberg gases [38, 39, 110]. The long coherence time indicates that beyond-nearest-neighbor interactions do not quickly destroy the coherence of the nearest-neighbor energy exchange, at least while the resonant process is active. Rather, the effect of the many-body interactions appears to be similar to that of an inhomogeneous field that causes the energy between the molecular states to vary from one atom pair to another. The strong, resonant, nearest-neighbor interactions may actually suppress population transfer due to the weaker next-nearest-neighbor coupling as has been proposed by Sun and Robicheaux [109]. This phenomena is a manifestation of frequency locking similar to that which is used in chapter 4 to suppress the decoherence in lithium qubits with a resonant rf driving field.

6.1 Experiment and Results

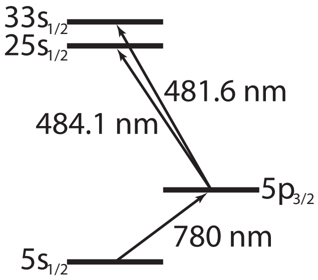

Figure 6.1: Diagram of laser excitation scheme for s Rydberg atoms in a rubidium MOT. 780 nm light from the MOT trapping lasers excites population from the $5s_{1/2}$ state to the $5p_{3/2}$ state. Population is then transferred to the Rydberg states by horizontally polarized light from two approximately 480 nm, 5 ns pulsed dye lasers.

These experiments are performed in the Rb^{85} magneto-optical trap (MOT) discussed in section 2.4. The trapping diode laser (780 nm) excites the ground state ($5s_{1/2}$) atoms to the trapped state ($5p_{3/2}$). The atoms are excited from the trapped state to the Rydberg states by horizontally polarized light (at approximately 480 nm) from two 5 ns dye lasers as shown in figure 6.1. The light from both dye lasers is focused into the MOT by a single 350 mm focal length lens. To achieve better overlap localization within the center of the MOT, the laser beams are crossed at a small angle by separating them as much as possible (about 50 mm) on the lens. Initially two Littman-style Coumarin 480 dye lasers drove the Rydberg transition. Although these lasers had the narrow line width necessary to selectively excite the desired states, they also produced a considerable amount of amplified spontaneous emission (ASE) which excited additional Rydberg and continuum states. Attempts to separate the ASE from the laser beam met with little success. Additionally, the lasers caused a significant amount of shot to shot excitation fluctuations due to the frequency instability of the multi-mode lasers. To resolve these issues, a more complex dye laser system was implemented.

To drive each Rydberg transition, light at about 960 nm from a Hansch-style dye laser (LDS 925 dye) is frequency-doubled in a Potassium Dihydrogen Phosphate (KDP) crystal and amplified in a dilute solution of Coumarin 480. To achieve the narrow line width necessary to select a single Rydberg state, an etalon (2 mm thick for the $33s$ transition and 1 mm thick for the $25s$ transition) is placed between the doubling crystal and the amplifier. The laser color is coarse tuned by adjusting the angle of the grating, while fine tuning is achieved by adjusting the angle of the etalon. This scheme virtually eliminates all of the blue ASE because the ASE from the infrared laser is too weak to be frequency-doubled. The spectrum of the doubled light is proportional to the autocorrelation of the spectrum of the infrared laser. Thus, there is some light at all frequencies within the doubled laser bandwidth. The etalon selects the correct color for excitation and the saturated amplifier reduces shot to shot intensity fluctuations. A Schott BG39 (blue bandpass 350 nm to 630 nm) filter [114] after the amplifier and aluminum mirrors eliminate most of the IR light remaining after the doubling process. Some shot to shot noise in the Rydberg signal remains even with the improved laser system, which is likely due to residual power fluctuations after amplification or to some jitter in the relative pulse arrival times.

We begin by repeating the resonance width measurements made by Anderson *el al.* [110, 111] in order to assess the similarity between our experimental setup and the original. The Rydberg energy levels are tuned into resonance by a fast-falling (2 ns) electric field pulse from the arbitrary wave form generator (AWG, see section 2.6) that is applied to the pair of vertical field rods closest to the microchannel plate detector (MCP). To determine the widths of the resonances, the tuning pulse is applied 500 ns prior to the arrival of the exciting laser pulses, and then, the interaction is detuned by a fast-rising field pulse 10 ns before the ramped ionization pulse is applied to the other set of field rods. An 8 mHz, 6 V triangle wave is applied to the same set of rods as the ionization pulse, slowly varying the electric field with every shot. The height and duration of the tuning pulse is dictated by the measurements to be made following the determination of the resonances widths. The pulse

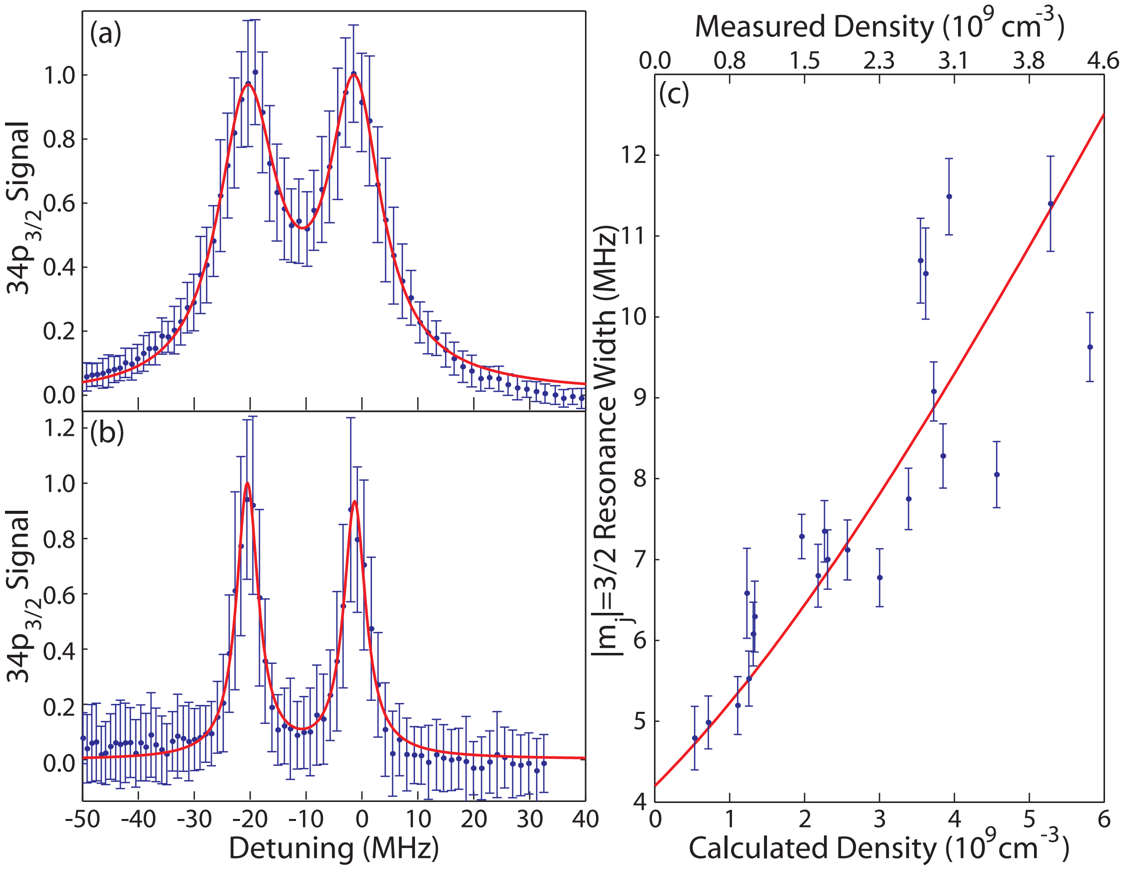

Figure 6.2: (a) and (b) Measured resonance energy transfer lineshapes as a function of detuning from the center of the $|m_j| = 3/2$ resonance. The $25s_{1/2}+33s_{1/2} \rightarrow 24p_{1/2}+34p_{3/2}$ $|m_j| = 1/2$ (3.0 V) and $|m_j| = 3/2$ (3.4 V) resonances broaden as the Rydberg atom density increases as shown for densities of 3.9×10^9 cm^{-3} (a) and 4.3×10^8 cm^{-3} (b). The $|m_j| = 3/2$ resonance broadens from 4.8 MHz in (b) to 11.5 MHz in (a). In (a) and (b) the blue points are the binned data and the red lines are the Lorentzian fits (equation 6.1). (c) Measured and calculated resonance width as a function of density. The measured resonance widths are shown in blue. We predict that the $|m_j| = 3/2$ resonance broadens linearly with the density such that $\Delta E_h = 1.8$ MHz/10^9 cm^{-3} when taking into account only the two body interactions and as $\Delta E_h = 1.85$ MHz/10^9 cm^{-3} when including the 3-body interactions. The red line shows the predicted resonance widths, according to the lower axis, assuming inhomogeneous broadening of $\Delta E_i = 4.2$ MHz which is added to the homogeneous width as for a Voigt profile (equation 5.43). The calculated widths are 1.3 times larger than the measured widths for the same density. This discrepancy is well within the experimental uncertainty of approximately 1.5× in the density.

directly from the AWG is 2 V in amplitude, but amplified pulses of up to 9 V are used in some experiments. The pulse duration varies between 1.9 μs and 16 μs depending on the subsequent measurement. The measured widths of the resonances show no dependence on the tuning pulse amplitude, nor is there a difference between the 1.9 μs and 16 μs pulse durations. The $34p_{3/2}$ and $33s_{1/2}$ ionization peaks are gated, and their sizes are recorded using Labview as in chapter 5 (see also section 2.5.3).

To determine the widths quantitatively, the data is fit as a function of the applied triangle wave voltage. The function is comprised of two Lorentzians on a constant background,

$$S_c = \frac{A_{1/2}}{(\mathbb{V} - \mathbb{V}_{1/2}).^2 + (\lambda_{1/2}/2)^2} + \frac{A_{3/2}}{(\mathbb{V} - \mathbb{V}_{3/2}).^2 + (\lambda_{3/2}/2)^2} + y_{off} \tag{6.1}$$

where S_c is the $34p$ signal, $\mathbb{V}$ is the triangle wave voltage, y_{off} is the fit parameter determining the constant background, and where A_{m_j}, λ_{m_j} and $\mathbb{V}_{m_j}$ with $m_j = 1/2$ or $3/2$ are the fit parameters determining the $|m_j|$ resonance's amplitude, width, and position. The electric field seen by the atoms is $F = (\mathbb{V} + \mathbb{V}_{off})/d_{eff}$ where $\mathbb{V}_{off}$ is an offset voltage that depends on the size of the applied tuning pulse and the voltage on the MCP. (Despite a grounded screen between the MCP and the interaction region there is some electric field, typically about 2 V/cm, in the interaction region due to the voltage, typically -2 kV, placed on the front MCP) d_{eff} is the effective plate separation which varies slightly day to day due to changes in the position of the MOT, but generally is about 3.55 cm. $\mathbb{V}_{off}$ and d_{eff} are determined from the fit by

$$d_{eff} = \frac{\mathbb{V}_{3/2} - \mathbb{V}_{1/2}}{.4 \text{ V/cm}} \tag{6.2a}$$

and

$$\mathbb{V}_{off} = 3.4 d_{eff} - \mathbb{V}_{3/2}. \tag{6.2b}$$

Anderson *et al.* determined that the energy difference between the $25s33s$ and $24p34p$ states varies quadratically with field such that $E = F^2 \times 7.5$ MHz cm^2/V^2 $- 88$ MHz [110]. Near the $|m_j| = 3/2$ resonance, the energy difference varies approximately linearly with the field, so the width of the resonance is given by $\Delta E_{3/2} = \lambda_{3/2}/d_{eff} \times 51$ MHz cm/V.

Figure 6.2(c) shows that resonance widths increase with the density. Our measured resonance widths as a function of density are very similar to those of Anderson *el al.* [110], including an offset of about 4 MHz at low density, if their density is rescaled by about a factor of 2. As will be discussed in detail in the analysis section, our results agree to within experimental uncertainty with our prediction for the widths when including about 4 MHz of inhomogeneous broadening and are also consistent with the calculations of Sun and Robicheaux [109]. We do not predict a significant contribution to the widths from the many-body interactions.

We also repeat the Ramsey interference measurements made by Anderson *et al.* [110] to determine if the dephasing rates in our system are comparable to those measured previously. To make these measurements, the electric field sequence shown in figure 6.3(a) is generated by the AWG and is amplified by the Avtech pulse amplifier, allowing for peak to peak voltage swings of up to 10 V. Immediately following excitation, the energy spacing is tuned to the peak of the $25s_{1/2} + 33s_{1/2} \rightarrow 24p_{1/2} + 34p_{3/2}$, $|m_j| = 3/2$ resonance by a negative field step with 12 ns rise and fall times. The longer rise and fall times were intentionally used to prevent voltage ring on the rods which, for faster rise and fall times, had amplitudes larger than the resonance width. After a time $t_r = 100$ ns on-resonance, a rising field step of height F_r detunes the molecular state energy levels for a time T_r before tuning back into resonance for an additional $t_r = 100$ ns with a falling field step. The energy levels are detuned again prior to detection of the final state composition via ramped field ionization. Typically, a detuning field of $F_r = 1.3$ V/cm (splitting of 66 MHz) was used because larger detunings resulted in unresolvable oscillations in the $34p_{3/2}$ signal. The ionization peaks are gated and integrated using boxcar integrators and are recorded using the data acquisition program Shaper5 (see section 2.5). Typically, 30 shots were averaged for every data point

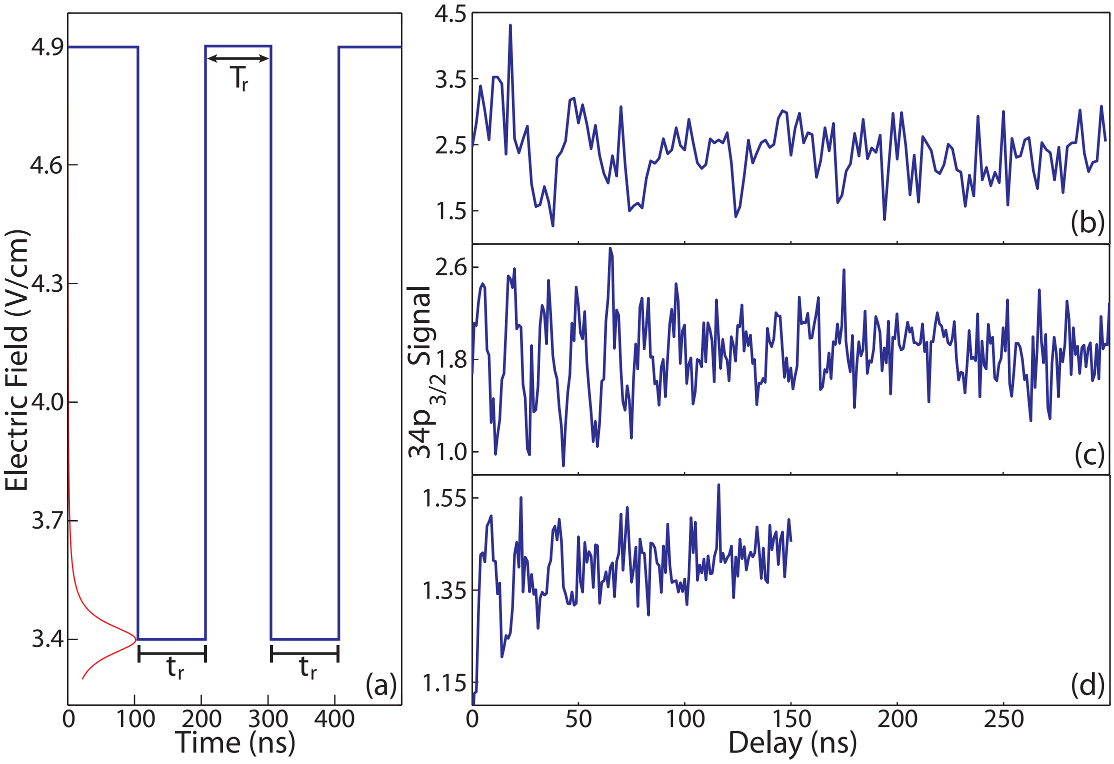

Figure 6.3: (a) Schematic of the electric field sequence used to observe a Ramsey interferogram. The energy exchange is tuned to resonance for $t_r = 100$ ns, detuned for a variable time T_r and then tuned back to resonance for an additional $t_r = 100$ ns. The electric field is shown in blue while the resonance is shown in red. The frequency of the observed oscillations is determined by the detuning from resonance. (b) Ramsey interferogram in the $34p_{3/2}$ signal for a detuning field of .5 V/cm corresponding to a splitting of 22 MHz and an oscillation period of $\tau = 1/22$ MHz $= 45$ ns. In (c) and (d) the detuning field is 1.3 V/cm corresponding to a detuning of 66 MHz and an expected Ramsey oscillation period of $\tau = 1/66$ MHz $= 15$ ns. The decay rate of the oscillations depends on the Rydberg atom density. In (c) the density is 5.3×10^8 cm^{-3} while it is 4.5×10^9 cm^{-3} in (d). In (d) the oscillations begin at a minimum. Numerical simulation shows that this likely results from the tuning field not being properly centered on the resonance. As discussed in chapter 5, the resonance broadens as the on resonance time is decreased. The broadened width of a 100 ns pulse is about 10 MHz, making it difficult to accurately determine the correct pulse voltage that places the system precisely at the center of the resonance.

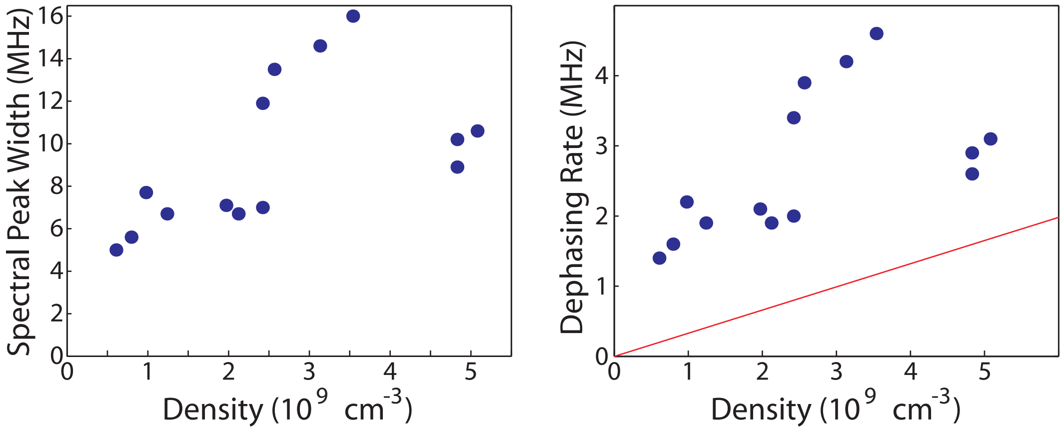

Figure 6.4: (a) The FWHM of the spectral peaks in the Fourier transforms of the Ramsey interferograms as a function of density. (b) Scaled dephasing rates associated with the spectral widths shown in (a). Assuming the dephasing of the interferogram is exponential, the dephasing rate is obtained by dividing the width of the spectral peak by $2\sqrt{3}$. The red curve is the dephasing rate predicted for short on resonance times and large detunings.

in a sweep and 5 to 10 sweeps are averaged for each run.

We find that the $34p_{3/2}$ signal oscillates as a function of T_r as the phase between the amplitudes acquired during the two interaction periods varies. The amplitude of the oscillations diminishes in about 100 ns. The frequency of the oscillations is dictated by the energy splitting between the $25s33s$ and $24p34p$ molecular states at the field, F_r, while the rate at which they decay depends on the density of the Rydberg atoms as shown in figure 6.3(b)-(d).

To determine the dephasing rate associated with each Ramsey interferogram, we take its Fourier transform and record the full width at half maximum of the resulting spectral peak. Figure 6.4(a) shows that these raw spectral widths tend to grow with increasing density. However, this density dependence requires some interpretation due to the finite duration of the on-resonance times and to the expected presence of inhomogeneous, as well as homogeneous, contributions to the dephasing. We will return to this in the analysis section. However, if we follow the example of Anderson *et al.*, and assume an exponential decay, the dephasing rate is $\Delta\nu_r = \Delta\nu_F/2\sqrt{3}$, as shown in figure 6.4(b), where $\Delta\nu_r$ is the

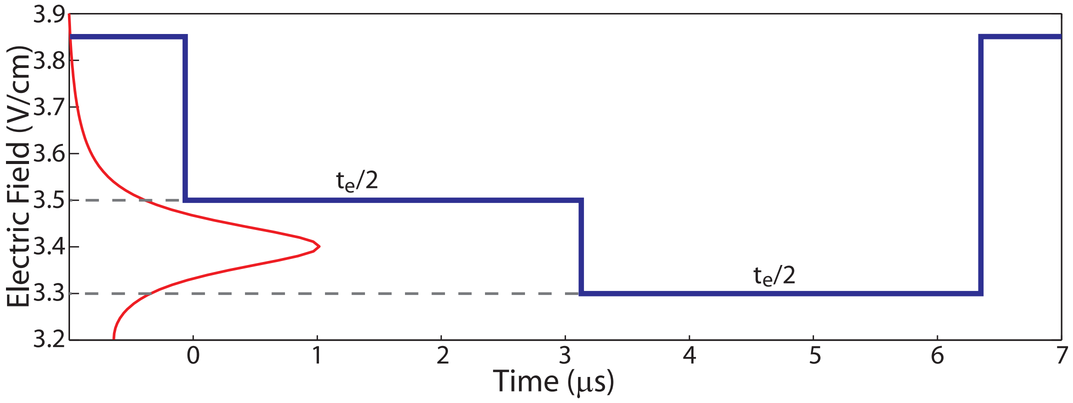

Figure 6.5: Schematic of the electric field sequence (blue) used to probe the coherence of the nearest-neighbor interactions. The field first tunes the atomic energy levels to the high field side of the $25s_{1/2} + 33s_{1/2} \rightarrow 24p_{1/2} + 34p_{3/2}$, $|m_j| = 3/2$ resonance (red), outside the inhomogeneous width. After a variable time $t_e/2$, a falling field step shifts the energy levels to the other side of the resonance such that $S_c(F_l) = S_c(F_h)$ where F_l and F_h are the electric fields on the low and high field sides of the resonance, respectively. After a time $t_e/2$, the states are completely detuned from resonance and the state distribution is measured by ramped field ionization. The electric field sequence creates a coherent enhancement in the $34p_{3/2}$ signal compared to remaining on either the high or low side of the resonance for a time t_e.

dephasing rate and $\Delta\nu_F$ is the spectral width from the Fourier transform. The rates in figure 6.4(b) are in reasonable agreement with those of Anderson *et al.* [110]. Interestingly, as shown in figure 6.4(b), there is little indication of dephasing at low-density. However, dephasing would be expected from the 4 MHz low density resonance width (assumed to be the result of inhomogeneous broadening).

Having established that our apparatus gives results similar to those perviously observed, we probe the time-dependent coherence of the $25s_{1/2}+33s_{1/2} \rightarrow 24p_{1/2}+34p_{3/2}$ interaction. To accomplish this, we increase the MOT density such that the resonances are broader than the inhomogeneous width by about a factor of $\sqrt{2}$ (ie. $\Delta E \gtrsim 6$ MHz) and apply the electric field sequence shown in figure 6.5. The atoms are excited to the Rydberg states in an electric field $F_h \approx F_{3/2}+3\Delta F_{3/2}/4$ (where $\Delta F_{3/2}$ is the field width of the $|m_j| = 3/2$ resonance) on the high-field side of the resonance. After a time $t_e/2$, a fast falling (2 ns) field step reduces the electric field to F_l, such that $S_c(F_l) = S_c(F_h)$, where the atoms remain for a time $t_e/2$.

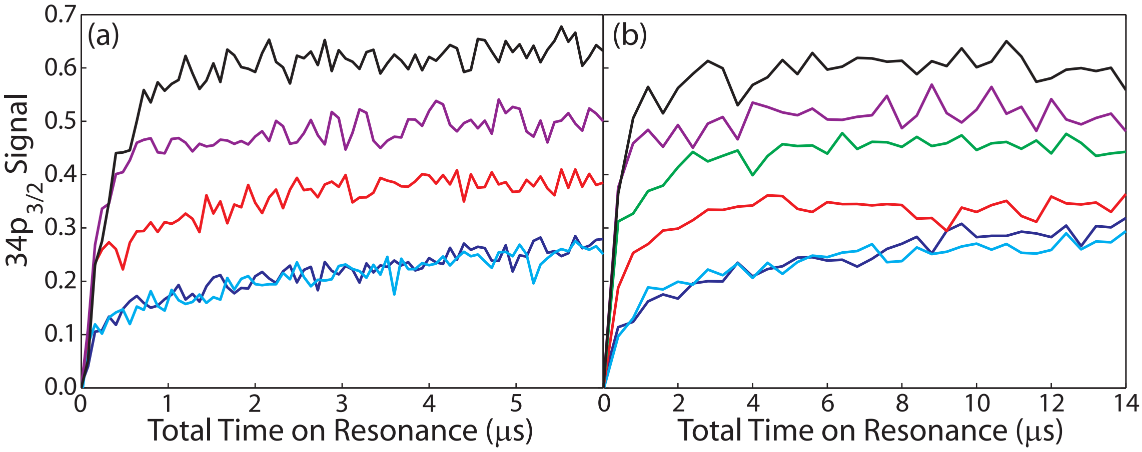

Figure 6.6: (a) and (b) $34p_{3/2}$ signal as a function of the on resonance time for several pulse sequences. Enhancement in the $24p34p$ signal results if the probability amplitudes transferred at detunings on the high and low field sides of the resonance add coherently. Traversing the 6.5 MHz wide resonance once (red), at half the on-resonance time ($t_e/2$), shows significant enhancement compared to remaining on either the high (blue) or low (cyan) side for t_e. Traversing the resonance more than once leads to additional enhancement (3 times (green), 7 times (purple), and 15 time (black) at $t_e/4$, $t_e/8$ and $t_e/16$ respectively). The additional enhancement indicates that the effect is not due to excitation of different atoms within the inhomogenously broadened resonance width. All curves are normalized to the signal obtained on resonance for a 14 μs interaction time. In (a), points are separated by $\Delta t_e = 80$ ns and in (b) $\Delta t_e = 400$ ns.

Then, the atoms are detuned off resonance as far as the AWG will allow (generally about .4 V/cm $\approx$ 22 MHz) by a fast rising field step, and the state distribution is measured in the same manner as for the Ramsey experiment. As shown in figures 6.6 and 6.7, jumping across the resonance after a time $t_e/2$ leads to an enhancement in the $34p_{3/2}$ signal compared to the signal obtained by remaining on either the high or low side of the resonance for the full interaction time, t_e. The enhancement is also observed when the atoms start out on the low field side of the resonance and jump to the high field side. The enhancement is not an effect of resonant excitation as the atoms traverse the resonance. If the atoms are left on the low field side for only 10 ns while the time on the high field side is $t_e - 10$ ns, no enhancement is observed.

One might conclude that the enhancement is due to a hole-burning effect in which we observe population transfer from atoms at different locations in the MOT on the high

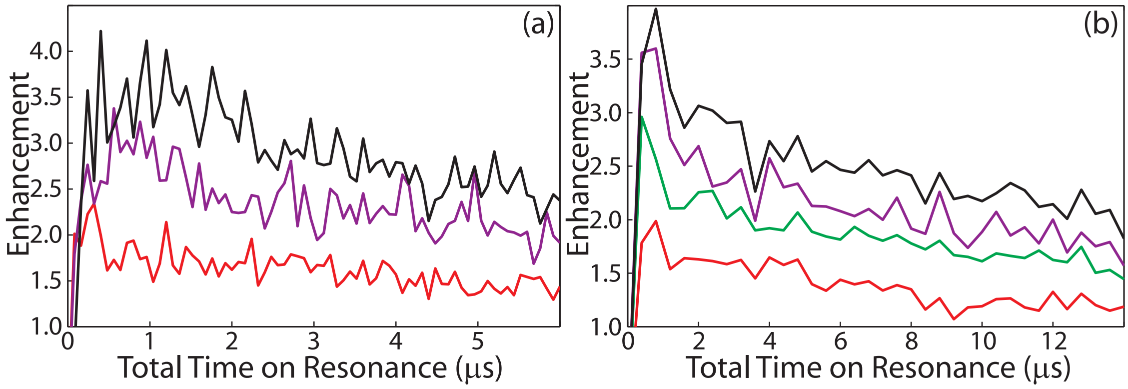

Figure 6.7: (a) and (b) enhancement in the $34p_{3/2}$ signal obtained form various jump sequences relative to that obtained when remaining on one side of the resonance for the total interaction time. The enhancement in the signal after jumping across the 6.5 MHz wide resonance once (red), thrice (green), seven times (purple) and fifteen times (black) compared to remaining on one side of the resonance from figure 6.6. (a) shows the enhancement at early times while (b) shows the long term decay of the enhancement.

and low field sides of the resonance, due to the inhomogeneity of the electric or magnetic fields. We intentionally reduce such effects by working in the wings of resonances which are substantially broader than the 4 MHz inhomogeneous width. Furthermore, jumping more frequently (eg. 3 traverses with one jump every $t_e/4$) does not access more atoms, yet leads to additional enhancement as shown in figure 6.6. Instead, the enhancement is due to the coherent addition of probability amplitudes transferred during the two interaction periods at different detunings. This enhancement survives averaging over nearest and next-nearest-neighbor distributions in the ensemble. However, it does not persist if the coherence time within isolated atom pairs is less than the interaction time on each side of resonance ($t_e/2$ for one jump, $t_e/4$ for 3 jumps, etc.). In that case, the population transfers from each interaction period is independent, and the combined result of multiple interactions is identical to that of a single interaction period at F_h or F_l (ie. the enhancement factor is 1).

To determine if the enhancement in the $34p_{3/2}$ signal shown in figure 6.6 changes with time, we divide the signal resulting from the various jump sequences by the average value of the signal that results from sitting on the high and low field sides for a time t_e. The time dependent enhancement is shown in figure 6.7 for a 6.5 MHz wide resonance. We find that enhancement decays exponentially with increasing interaction times with a time constant $\tau \approx 12.5$ μs. As discussed further in the analysis section, the persistence of the enhancement indicates that coherence is maintained in the ensemble for a time comparable to the 13 μs radiative lifetime of the 25s state, (ie. about two orders of magnitude longer than the dephasing times observed in the Ramsey interference measurement).

6.2 Analysis

To quantitatively assess the data for the three types of measurements, we first calculate coupling strengths for the three different energy exchange processes as was done for potassium in section 5.2. For the tunable interaction, $25s_{1/2} + 33s_{1/2} \rightarrow 24p_{1/2} + 34p_{3/2}$, we add the interaction strengths of the different allowed final states, m_ℓ-sublevels in quadrature to find $V_{sspp} = \sqrt{2/3}u_{25s24p}u_{33s34p}/R^3$. We use Numerov integration to calculate $u_{33s34p} = \langle\mathcal{R}_{33s}|\, r\, |\mathcal{R}_{34p}\rangle = 125$ atomic units and $u_{25s24p} = \langle\mathcal{R}_{25s}|\, r\, |\mathcal{R}_{24p}\rangle = 490$ atomic units where $|\mathcal{R}_{nl}\rangle$ is the radial portion of the Rydberg electron wavefunction and r is the radial position of the electron. One might initially expect u_{33s34p} to be larger than u_{25s24p} since the dipole matrix elements between adjacent states scale with n^{*2} [41]. This apparent discrepancy is simply explained, as the $34p_{3/2}$ state is not the next highest lying p state to the $33s_{1/2}$ state. (Specifically, the $33p$ states are the next highest lying p states with $n^* = 30.4$, while $n^* = 29.9$ for $33s_{1/2}$ and $n^* = 31.4$ for $34p_{2/3}$.) For the always resonant interactions, $25s_{1/2} + 24p_{1/2} \rightarrow 24p_{1/2} + 25s_{1/2}$ and $33s_{1/2} + 34p_{3/2} \rightarrow 34p_{3/2} + 33s_{1/2}$, we assume the orientation of the third atom is random relative to the pair of atoms undergoing the tunable interaction, and hence, the p state has equal probability of being in $m_\ell = 0, \pm 1$ along the axis defined by the pair. Therefore, we average the interaction strengths for the different m_ℓ values and find that $V_{spps} = 4u^2_{nsn'p}/9R^3$ where $n = 25$ and $n' = 24$ or $n = 33$ and $n' = 34$.

6.2.1 Resonance Widths

In analogy with the previous chapter, we begin by considering only the contribution of the nearest-neighbor interactions to the width. We can express the pair states in the molecular basis, $|A\rangle = |25s\rangle\,|33s\rangle$ and $|B\rangle = |24p\rangle\,|34p\rangle$ and make the box approximation. The transition probability after a time t_c is given by equation 5.12,

$$P(t_c) = |C_B(t_c)|^2 = \frac{4V_0^2}{E^2+4V_0^2}\sin^2\frac{\sqrt{E^2+4V_0^2}t_c}{2}, \tag{6.3}$$

where V_0 is the two-body dipole potential ($V_0 = \sqrt{2/3}u_{25s24p}u_{33s24p}/R^3$) and E is the detuning from resonance. In the previous chapter, we were in the regime where $t_c \ll 1/V_0$; however,in the experiments performed in a cold Rydberg gas, the atoms move only a small fraction of the interatomic spacing during the on-resonance time, so $t_c \gg 1/V_0$. The homogeneous lineshape is determined by averaging over the nearest-neighbor distribution given by equation 5.35 assuming that at long times the $\sin^2$ term averages to 1/2 and has the form of a cusp (see equation 5.45). The homogeneous linewidth is proportional to the most probable interaction strength, $\Delta E_h = 4\bar{V}_0$, where $\bar{V}_0 \approx \sqrt{6}u_{25s24p}u_{33s34p}\pi\rho$ where ρ is the density of Rydberg atoms in a single initial state.

To model the three-body interaction, we consider a system of three atoms (a, b and c) initially in the same s state. Each atom has three possible states, $|s\rangle$, $|p_1\rangle$ and $|p_2\rangle$, where $2E_s \sim E_{p_1} + E_{p_2}$. The s and p states are coupled by $u_{1s} = \langle s|\,r\,|p_1\rangle$ and $u_{2s} = \langle s|\,r\,|p_2\rangle$. In the molecular basis there are seven possible states:

$$\begin{gathered} |I\rangle = |s\rangle\,|s\rangle\,|s\rangle\,,\ |J\rangle = |p_1\rangle\,|p_2\rangle\,|s\rangle\,,\ |K\rangle = |p_2\rangle\,|p_1\rangle\,|s\rangle\,,\ |L\rangle = |p_1\rangle\,|s\rangle\,|p_2\rangle\,, \\ |M\rangle = |p_2\rangle\,|s\rangle\,|p_1\rangle\,,\ |N\rangle = |s\rangle\,|p_1\rangle\,|p_2\rangle\ \text{ and }\ |O\rangle = |s\rangle\,|p_2\rangle\,|p_1\rangle \end{gathered} \tag{6.4}$$

and where $E_I = 0$ and $E_J = E_K = E_L = E_M = E_N = E_O = E$. We assume the distance, R_{ab}, between atoms a and b is less than the distances between atoms a and c (R_{ac}) and between b and c (R_{bc}) (ie. we assume atoms a and b are nearest neighbors and atom c

is the next-nearest neighbor). We make the approximation that $R_{ac} = \sqrt{R_{bc}^2 + R_{ab}^2}$ as a compromise between the linear and isosceles triangle configurations for the three atoms. The Hamiltonian in this basis is

$$H_3 = \begin{pmatrix} 0 & V_1 & V_1 & V_2 & V_2 & V_3 & V_3 \\ V_1 & E & 0 & V_4 & 0 & 0 & V_5 \\ V_1 & 0 & E & 0 & V_6 & V_7 & 0 \\ V_2 & V_4 & 0 & E & 0 & V_8 & 0 \\ V_2 & 0 & V_6 & 0 & E & 0 & V_9 \\ V_3 & 0 & V_7 & V_8 & 0 & E & 0 \\ V_3 & V_5 & 0 & 0 & V_9 & 0 & E \end{pmatrix} \tag{6.5}$$

where

$$V_1 = \sqrt{\frac{2}{3}}\frac{u_{1s}u_{2s}}{R_{ab}^3},\; V_2 = \sqrt{\frac{2}{3}}\frac{u_{1s}u_{2s}}{R_{ac}^3},\; V_3 = \sqrt{\frac{2}{3}}\frac{u_{1s}u_{2s}}{R_{bc}^3},\; V_4 = \frac{4}{9}\frac{u_{1s}u_{1s}}{R_{bc}^3},\; V_5 = \frac{4}{9}\frac{u_{2s}u_{2s}}{R_{ac}^3},$$

$$V_6 = \frac{4}{9}\frac{u_{2s}u_{2s}}{R_{bc}^3},\; V_7 = \frac{4}{9}\frac{u_{1s}u_{1s}}{R_{ac}^3},\; V_8 = \frac{4}{9}\frac{u_{2s}u_{2s}}{R_{ab}^3} \text{ and } V_9 = \frac{4}{9}\frac{u_{1s}u_{1s}}{R_{ab}^3}.$$

To compute the resonant energy transfer for a single atom pair in a pulsed field, we calculate the field dependent eigenstates and eigenvalues of H_3. We then determine the time-dependent probability that the system remains in the initial state, P_I, by rotating the initial state vector from the uncoupled basis into the eigenbasis of H_3, propagating for a time t, and then projecting back onto the initial basis. The probability that the system is in any state where one atom is in $|s\rangle$ and the other two atoms are in $|p_1\rangle$ and $|p_2\rangle$ is $P_{pp} = 1 - P_I$. We simulate the measured transition probability by averaging R_{ab} over the nearest-neighbor distribution (equation 5.35) and R_{bc} over the approximate next-nearest-neighbor distribution,

$$\mathbb{F}(R_n) = 4\pi\rho\left(R_n - \frac{R_0}{2}\right)^2 e^{-\frac{4\pi\rho}{3}\left(R_n - \frac{R_0}{2}\right)^3} \tag{6.6}$$

where $R_0 = 1/(2\pi\rho)^{1/3}$. The width of the resonance is determined directly from the field

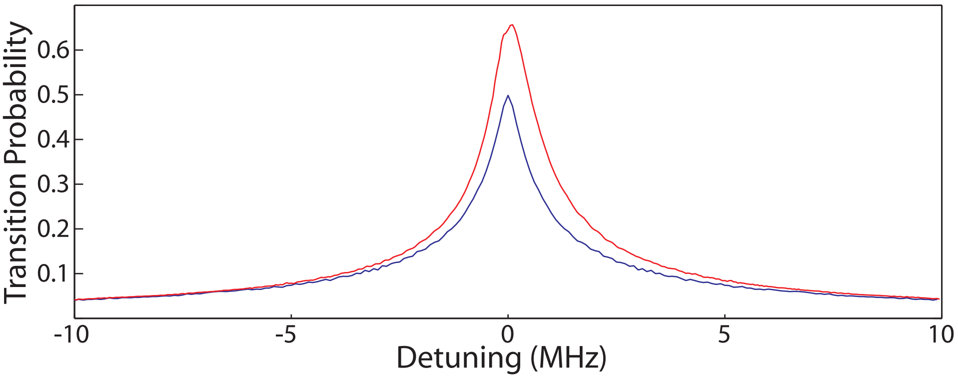

Figure 6.8: The calculated resonances due to pairwise interactions (blue) and three body interactions (red).

dependence of P_{pp}.

To compare the three-body and two-body interaction, we set $V_i = 0$ for $i = 2$ through 9. Using this method, we find that, when considering only the pairwise interactions, the homogeneous width of the $25s_{1/2} + 33s_{1/2} \rightarrow 24p_{1/2} + 34p_{3/2}$, $|m_j| = 3/2$ resonance scales linearly with the density of the Rydberg atoms such that $\Delta E_h = \rho \times 1.8\ \mathrm{MHz}/10^9\ \mathrm{cm}^{-3}$. When including the three-body interaction, $\Delta E_h = \rho \times 1.85\ \mathrm{MHz}/10^9\ \mathrm{cm}^{-3}$. The slight width difference between the two models is undetectable in our measurements. As shown in figure 6.8, although the three body interactions do not significantly affect the width of the resonances, they do result in a noticeable enhancement in the transition probability due to the increased number of states involving two p atoms.

The red line in figure 6.2(c) shows the predicted widths as a function of density assuming an inhomogeneous broadening component of $\Delta E_i = 4.2$ MHz. The measured and computed widths are in good agreement if the measured densities are scaled by a factor of 1.3. This discrepancy is well within the experimental error in the density measurement, indicating that the measured widths are dominated by two-body nearest-neighbor interactions.

Much of the inhomogeneous width appears to be due to the trapping magnetic field gradient. As discussed in section 2.4.2, the on-axis field gradient is about 15 Gauss/cm, so for a 0.5 mm MOT diameter, the variation in the magnetic field across the MOT is

750 mGauss, putting the energy shifts associated with the field in the Paschen-Back regime over most of the MOT. We note that, in general, the electric and magnetic field axes are not parallel. If we assume that the magnetic field facilitates transitions such that $\Delta m = 0, \pm 1$, the MOT field gradient results in broadening of about 3.8 MHz for the $m_j = 3/2$ resonance [115]. If the non-collinear magnetic field does not result in transitions where $\Delta m = \pm 1$, we would expect different magnetic contributions to the inhomogeneous width of the $|m_j| = 1/2$ and $|m_j| = 3/2$ resonances, 4.4 MHz and 1.4 MHz, respectively. Yet, we observe that the resonances are approximately the same width. The predicted broadening of 3.8 MHz is in good agreement with the minimum resonance widths observed in the MOT. Running with a high rubidium background pressure for a few days resulted in an increase in the minimum observed resonance width to 4.2 MHz, likely due to rubidium building up on the field rods which results in electric field inhomogeneity. We calculate that the geometry of the rods results in an electric field inhomogeneity of 0.15% across the MOT. Near the $|m_j| = 3/2$ resonance this would lead to an inhomogeneous width of 260 kHz. Patch fields resulting in a field variation of 40 mV/cm in the electric field would result in 2 MHz of inhomogeneous broadening which, when added in quadrature with the magnetic field term, results in $\Delta E_i = 4.3$ MHz. Such a 1% variation in the electric field does not seem unreasonable. The hyperfine structure of the s-state (1.7 MHz for $25s_{1/2}$) is not expected to play a significant role as the intermediate $5p_{3/2}$ state is optically pumped to $F = 4$. The hyperfine splittings for the p-states are much smaller, only tens of kilohertz for $24p$ [93].

6.2.2 Ramsey Interference

To quantitatively determine the decay rates of the Ramsey oscillations shown in figure 6.3, we take the Fourier transform of each interferogram and determine the width of the resulting spectral peak, $\Delta\nu_F$. As noted in section 6.1, interpreting this spectral width requires some care. If the amplitude of the interferogram decays exponen-

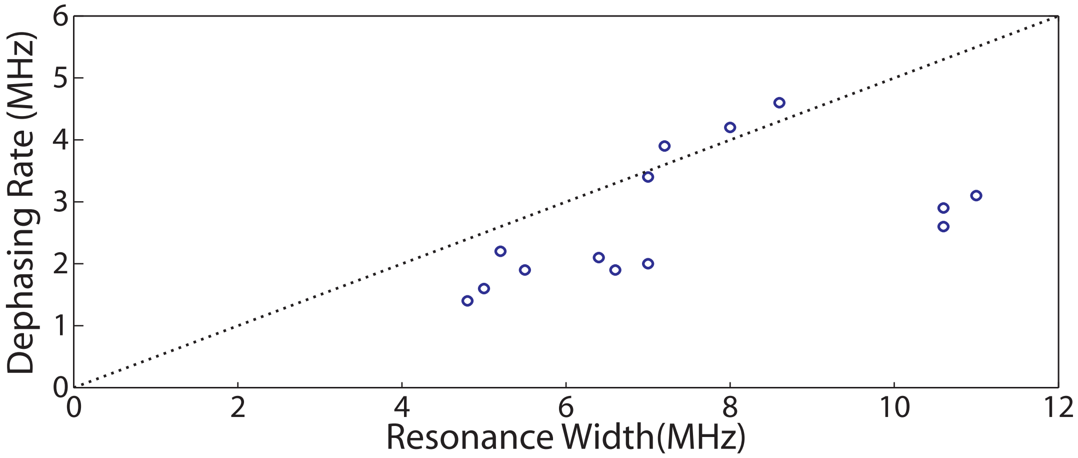

Figure 6.9: The dephasing rates (ν_r, blue circles) measured from the Ramsey interferograms assuming exponential decay are plotted as a function of the resonance width (ΔE). The dotted line is $\nu_r = \Delta E/2$.

tially, $S(t) = S_0 e^{-\Gamma t}\cos\omega t$, where ω is the detuning, the full width at half the maximum of the peak in the Fourier transform is $\Delta\nu_F = \sqrt{3}\Gamma/\pi$. Thus, the dephasing rate $\Gamma/2\pi = \Delta\nu_F/2\sqrt{3}$. Figure 6.4(b) shows the dephasing rate of the Ramsey oscillations as a function the resonance width if we assume the decay is exponential [110]. Like the resonance widths, the dephasing rate increases with the density. However, as shown in figure 6.9, the decay rate is generally less than half the resonance width for a given density and appears to show no signs of inhomogeneous broadening (as indicated by the zero intercept). These results are in good agreement with those of Anderson *et al.* [110], with characteristic decay times on the order of 100 ns.

If the interferogram amplitude is Gaussian (as would be expected for a Gaussian inhomogeneous field distribution) extracting a dephasing rate from the Fourier transform is more difficult due to the non-zero interaction time, t_r, used in the experiments. If $t_r = 0$, the amplitude of the interferogram is a Gaussian with its maximum at $T_r = 0$. The full width at half the maximum of the spectral peak ($\Delta\nu_F$) obtained by Fourier transforming the interferogram for $T_r \geq 0$ is approximately 1.8 times greater than the actual spectral width ($\Delta\nu_r$) associated with the inhomogeneous broadening. If $t_r > 0$, as in the experiments, the interferogram amplitude as a function of T_r is a Gaussian whose maximum has been translated to $T_r = -t_r$. Thus, the measured portion of the interferogram is effectively truncated, resulting in additional broadening of the spectral width. For example, if $t_r = 100$ ns and dephasing is caused by 4 MHz of inhomogeneous Gaussian broadening, the full width at half the maximum of the spectral peak obtained by Fourier transforming the interferogram is approximately 11.6 MHz, roughly 2.9 times larger than the actual value. The situation is more complicated at intermediate densities where Gaussian and exponential decays may contribute equally to the dephasing.

However, in spite of the uncertainty in the actual form of the interferogram's amplitude, an exponential decay is a reasonable approximation. For example, if we assume that the dephasing is due to Gaussian broadening at low densities and exponential decay at high densities, then the slope of the decay rates in figure 6.9 will be reduced by about 20%. A similar decrease in slope is expected if we assume that the interferogram decay has a Gaussian form at all densities.

If the density dependence of the measured dephasing rate is primarily due to beyond-nearest-neighbor interactions, we might expect the ratio of the dephasing rate to the resonance linewidth to be proportional to the ratio V_{spps}/V_{sspp}, since the resonance linewidth is determined almost solely by the pairwise interaction. If we assume Lorentzian lineshapes, then the constant of proportionality is 1.

To compare the coupling strengths for the nearest-neighbor (V_{sspp}) and next-nearest-neighbor (V_{spps}) interactions for average interatomic spacings, we consider only the $|25s\rangle\,|24p\rangle \rightarrow |24p\rangle\,|25s\rangle$ next-nearest-neighbor interaction since u_{25s24p} is four times greater than u_{33s34p}. The most probable nearest-neighbor separation is $R_0 = (2\pi\rho)^{1/3} \approx 0.54\rho^{-1/3}$ while the most probable next-nearest-neighbor separation is approximately $R_{n0} \simeq 3R_0/2 \approx 0.81\rho^{-1/3}$. So for the most probable interatomic spacings,

$$\frac{V_{spps}}{V_{sspp}} = \frac{4}{9}\sqrt{\frac{3}{2}}\frac{u_{25s24p}u_{25s24p}}{u_{25s24p}u_{33s34p}}\frac{R_0^3}{R_{n0}^3} \approx \frac{1}{2}. \tag{6.7}$$

Thus, we estimate that the dephasing due to always-resonant interactions is roughly 1/2 the resonance width at a given density. As shown in figure 6.9, this estimate serves as an upper limit for the measured dephasing rates.

We can also compute the effects of next-nearest-neighbor interactions on the dephasing rate by simulating the Ramsey interference experiment using the three atom model described in the preceding section. Assuming the population in each of the three atoms is initially in the s-state, we compute the probability amplitude in each of the seven available molecular states after a time t_r on resonance, followed by projection off resonance in a field F_r for a time T_r and a final time t_r back on resonance. For very short interaction times ($t_r \cong 5$ ns) and large detuning fields ($F_r \cong 6$ V/cm), the simulation predicts a dephasing rate which increases approximately linearly with density, with a slope of 0.33 MHz/1×10^9 cm^{-3} (assuming exponential decay of the interferogram). As shown in figure 6.4(b), this prediction slightly underestimates the slope of the measured dephasing rates.

It is worth noting that for $t_r = 100$ ns, as in the experiments, the simulation predicts dephasing rates which are a factor of two to three smaller at low density and exhibit a sub-linear increase with density. The differences between the $t_r = 5$ ns and $t_r = 100$ ns calculations stem from the large two-body probability amplitude transfer rates that are predicted for a significant fraction of the atom separations at the densities studied. In addition, for large values of T_r (about 1 μs) the simulation indicates that non-negligible probability amplitude can be transferred at the experimental detuning of 66 MHz. Thus, it appears that, in the regime in which the experiments were performed, the simple perturbative Ramsey interference picture does not fully apply. Even so, it is unclear why the simulation, which is non-perturbative, fails to reproduce the experimental results. Unfortunately, this means that the simulation has not shed any light on the apparent absence of any inhomogeneous broadening contribution to the measured dephasing rate at low densities.

Regardless of the accuracy of the simulation model, our experimental results are consistent with those of Anderson *et al.* [110] and indicate dephasing when atom pairs are detuned from resonance which results in the damping of the Ramsey interference over short times, comparable to 100 ns.

6.2.3 Coherent Spectroscopy

As discussed briefly in section 6.1, the signal enhancement obtained in the single jump sequence should decay to 1 when the interaction time $t_e/2$ is extended beyond the pair coherence time within the ensemble. Thus, the decay of the enhancement provides a measure of this coherence time. To determine the decay rate of the enhancement in the $34p_{3/2}$ signal shown in figure 6.7(b), we fit exponentials to the data as shown in figure 6.10(a) for all of the jump sequences. Figure 6.10(b) shows the exponential decay rates for the fits in 6.10(a). These correspond to enhancement decay times of about 10 μs, much longer than the dephasing times associated with either the resonance line widths or with the Ramsey interference. From inspection of figures 6.6(a) and (b) it is clear that the decay in the enhancement results from the slow increase in the signal when the system remains on one side of the resonance. Since the spontaneous emission lifetime of the $25s$ state is 13 μs [41], it is possible that the increase in the $34p$ signal would be greater if not limited by the loss of $25s$ atoms. However, the rate of spontaneous emission is likely somewhat reduced because on resonance the atoms are of mixed $25s$ and $24p$ character, and the lifetime of the $24p$ state is 30 μs. Figure 6.10 suggests that there may be a decrease in the enhancement decay rate as additional jumps are applied. This may be an indication that the electric field sequence can suppress dephasing in a method similar to that discussed in chapter 3. However, further investigation is necessary to confirm this.

To understand the enhancement in the signal acquired from the time and frequency-separated interactions, we first consider the two-body interactions (neglecting inhomogeneous effects) in a two level system in the rotating wave approximation. The transfer

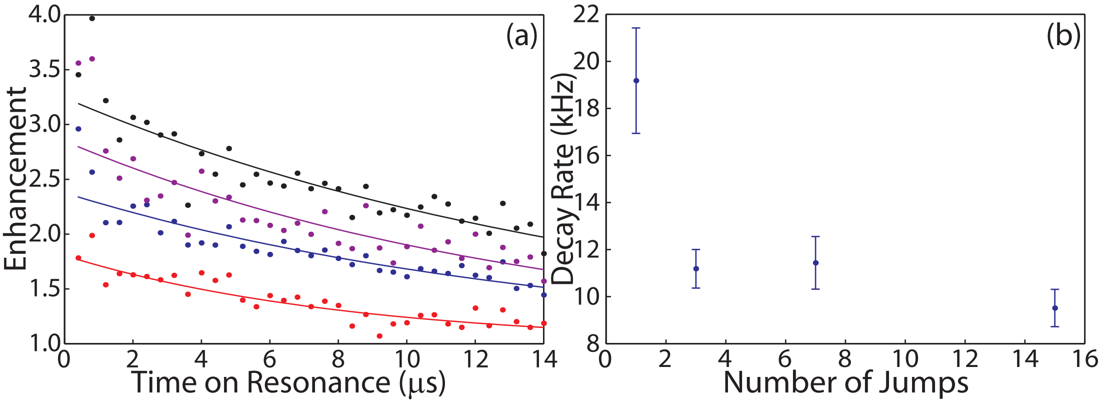

Figure 6.10: (a) Exponential fits to the measured enhancement verses total interaction time data for several different jump sequences. The decays in the enhancement shown in figure 6.7(b) (1 jump = red, 3 jumps = green, 7 jumps = purple and 15 jumps = black) are fit with exponentials (solid lines). (b) The decay rates from the fits in (a) are plotted as a function of the number of jumps across the resonance. The decays take about 10 μs, much longer that the time scales associated with the Ramsey dephasing or with the resonance widths.

matrix at a detuning E from resonance is

$$U_\phi = \begin{pmatrix} \cos\phi - i\eta\sin\phi & i\xi\sin\phi \\ i\xi\sin\phi & \cos\phi + i\eta\sin\phi \end{pmatrix} \tag{6.8}$$

where $\phi = \gamma t/2$ is the Rabi flopping phase, $\gamma = \sqrt{4V^2 + E^2}$ is the Rabi frequency, V is the dipole coupling between the molecular states, $\xi = 2V/\gamma$ and $\eta = E/\gamma$ so $\eta^2 + \xi^2 = 1$ [116]. In the following, we assume perfect coherence is maintained. The atom pair begins in state $|A\rangle = |25s\rangle\,|33s\rangle$ and evolves at a detuning ε for a time $t_e/2$, which is described by the transfer matrix U_{ϕ_+}, where $\phi_+ = \gamma t_e/4$, $\gamma = \sqrt{4V^2 + \varepsilon^2}$ and $\eta_+ = \varepsilon/\gamma$. Detuning to $-\varepsilon$ and allowing the system to evolve for an additional time $t_e/2$ is described by U_{ϕ_-} which is identical to U_{ϕ_+} except $\eta_- = -\eta_+ = -\varepsilon/\gamma$. Thus, letting $\phi = \phi_+ = \phi_-$ and $\eta = \eta_+ = -\eta_-$

the transfer matrix for the electric field sequence shown in figure 6.5 is

$$\begin{aligned} U_j &= U_{\phi_-} U_{\phi_+} \\ &= \begin{pmatrix} \cos\phi + i\eta\sin\phi & i\xi\sin\phi \\ i\xi\sin\phi & \cos\phi - i\eta\sin\phi \end{pmatrix} \begin{pmatrix} \cos\phi - i\eta\sin\phi & i\xi\sin\phi \\ i\xi\sin\phi & \cos\phi + i\eta\sin\phi \end{pmatrix} \\ &= \begin{pmatrix} 1 - 2\xi^2\sin^2\phi & 2i\xi\sin\phi\cos\phi - 2\xi\eta\sin^2\phi \\ 2i\xi\sin\phi\cos\phi - 2\xi\eta\sin^2\phi & 1 - 2\xi^2\sin^2\phi \end{pmatrix}. \end{aligned} \tag{6.9}$$

Since the atom pair starts out in $|A\rangle$, the probability that the atoms will be found in $|B\rangle$ after the electric field sequence is

$$P_{Bj}(t_e) = |\langle B| U_j |A\rangle|^2 = 4\xi^2 \sin^2\phi \left(\cos^2\phi + \eta^2\sin^2\phi\right). \tag{6.10}$$

If the system remains detuned at $\pm\varepsilon$ for a time t_e with no field step,

$$U_{2\phi_\pm} = \begin{pmatrix} \cos 2\phi \mp i\eta\sin 2\phi & i\xi\sin 2\phi \\ i\xi\sin 2\phi & \cos\phi \pm i\eta\sin 2\phi \end{pmatrix} \tag{6.11}$$

and

$$P_{B\pm}(t_e) = \left|\langle B| U_{2\phi_\pm} |A\rangle\right|^2 = 4\xi^2\sin^2\phi\cos^2\phi. \tag{6.12}$$

As long as coherence is maintained within the atom pair, the enhancement in the B-state probability due to jumping across the resonance at $t_e/2$ is

$$\frac{P_{Bj}(t_e)}{P_{B\pm}(t_e)} = 1 + \eta^2\tan^2\phi. \tag{6.13}$$

Thus, we see that $P_{Bj}(t_e)/P_{B\pm}(t_e) \geq 1$ for all values of ϕ. When we average over the distribution of pair spacings (ie. average over the range of V) for the ensemble, we observe enhancement in the B state probability when jumping across the resonance as compared to remaining on one side of the resonance. If there is no phase coherence between the time

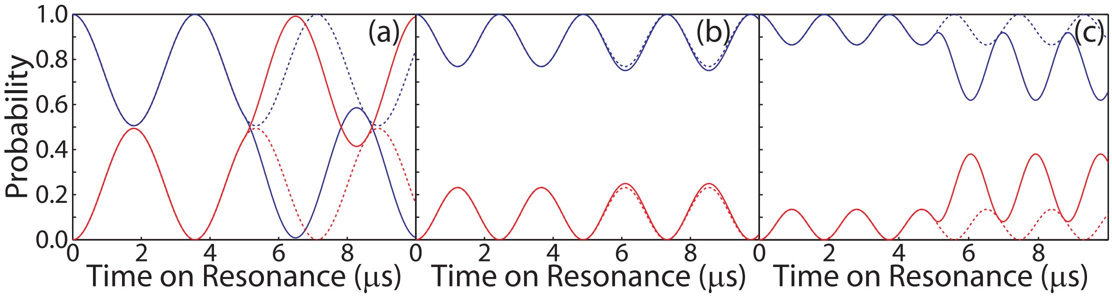

Figure 6.11: The probability of the atom pair at the average interatomic spacing being in state A (blue) and B (red) with (solid line) and without (dashed line) a jump occurring after 5 μs for different detunings. Varying the detuning has a similar effect on the transition probability as varying the interatomic spacing. Experimentally, the interatomic spacing varies between atom pairs, resulting in a distribution of detunings and Rabi frequencies over the ensemble. (a) Detuned to 0.2 MHz, the jump occurs near a maximum in P_B which leads to a large enhancement in P_B from an average of 0.25 to an average of 0.70. (b) Detuned to 0.36 MHz, the jump occurs near a minimum in P_B which leads to a small enhancement in P_B from an average of 0.116 to an average of 0.125. (c) Detuned to 0.5 MHz, the jump occurs at an intermediate value of P_B leading to a moderate enhancement in the average value of P_B from 0.07 to 0.23.

periods spent at ε and $-\varepsilon$, then transporting the system to an equidistant point across the resonance will have no effect, and there will be no enhancement.

Figure 6.11 shows the probability of an atom pair with average spacing being in states A and B with and without a single jump for different detunings. The enhancement in the average value of P_B in each pair of atoms depends on the phase of the Rabi oscillation at the time of the jump. If the amplitude in state B is small, there is little enhancement while if the amplitude is at a maximum the enhancement will be greater. In the experiment, jumps occur at all values of the Rabi phase because the variations in atom spacings across the ensemble result in a distribution of Rabi frequencies. Therefore, we measure an average enhancement for the ensemble.

Provided coherence is maintained, we can more explicitly see the increase in P_B by rewriting the state vector after the echo in terms of the state probabilities and amplitudes at the time of the jump. After propagating for a time $t_e/2$ at a detuning ε, the state vector is

$$\begin{aligned} U_{\phi_+}\begin{pmatrix} 1 \\ 0 \end{pmatrix} &= \begin{pmatrix} \cos\phi - i\eta\sin\phi & i\xi\sin\phi \\ i\xi\sin\phi & \cos\phi + i\eta\sin\phi \end{pmatrix}\begin{pmatrix} 1 \\ 0 \end{pmatrix} \\ &= \begin{pmatrix} \cos\phi - i\eta\sin\phi \\ i\xi\sin\phi \end{pmatrix} = \begin{pmatrix} C_{A0} \\ C_{B0} \end{pmatrix} \end{aligned} \tag{6.14}$$

and we can rewrite the transfer matrix in terms of the state vector coefficients

$$U_{\phi_+} = \begin{pmatrix} \cos\phi - i\eta\sin\phi & i\xi\sin\phi \\ i\xi\sin\phi & \cos\phi + i\eta\sin\phi \end{pmatrix} = \begin{pmatrix} C_{A0} & C_{B0} \\ C_{B0} & C_{A0}^* \end{pmatrix}. \tag{6.15}$$

Similarly,

$$U_{\phi_-} = \begin{pmatrix} \cos\phi + i\eta\sin\phi & i\xi\sin\phi \\ i\xi\sin\phi & \cos\phi - i\eta\sin\phi \end{pmatrix} = \begin{pmatrix} C_{A0}^* & C_{B0} \\ C_{B0} & C_{A0} \end{pmatrix}. \tag{6.16}$$

After a single jump sequence,

$$\begin{aligned} U_j\begin{pmatrix} 1 \\ 0 \end{pmatrix} &= U_{\phi_-}U_{\phi_+}\begin{pmatrix} 1 \\ 0 \end{pmatrix} = \begin{pmatrix} C_{A0}^* & C_{B0} \\ C_{B0} & C_{A0} \end{pmatrix}\begin{pmatrix} C_{A0} & C_{B0} \\ C_{B0} & C_{A0}^* \end{pmatrix}\begin{pmatrix} 1 \\ 0 \end{pmatrix} \\ &= \begin{pmatrix} |C_{A0}|^2 - |C_{B0}|^2 & 2C_{B0}C_{A0}^* \\ 2C_{B0}C_{A0} & |C_{A0}|^2 - |C_{B0}|^2 \end{pmatrix}\begin{pmatrix} 1 \\ 0 \end{pmatrix} \\ &= \begin{pmatrix} |C_{A0}|^2 - |C_{B0}|^2 \\ 2C_{B0}C_{A0} \end{pmatrix} = \begin{pmatrix} C_A \\ C_B \end{pmatrix}, \end{aligned} \tag{6.17}$$

where we have simplified the expressions using the fact that $C_{B0} = -C_{B0}^*$. Interestingly, the amplitude in state A is the difference in the probabilities for finding the systems in states A and B when the jump occurred, while the probability for being in state B is four times the product of the probabilities of being in state A and state B when the jump occurs.

Thus, P_A will decrease after the jump (ie. more population is transferred to $|B\rangle$) as long as $|P_A(t_e/2) - P_B(t_e/2)|^2 < P_A(t_e/2)$ which is the case for detunings outside the half width at half maximum.

This pattern is repeated for sequences of $2N-1$ jumps across the resonance, where N is a power of 2, as is the case in our experiments. In general, $P_{A,2N} = |P_{A,N} - P_{B,N}|^2$ where $P_{A,N}$ and $P_{B,N}$ are the probabilities that the system is in $|A\rangle$ and $|B\rangle$ after $N-1$ jumps. In addition, we find $P_{B,2N} = 4P_{A,N}P_{B,N}$. Therefore as long as the average value of P_B remains sufficiently small after $2N-1$ jumps, we expect additional signal enhancement if additional jumps are applied.

If coherence is maintained, we can also reexpress the transfer matrix for a single jump in terms of the density matrix at the time of the jump,

$$U_j = \begin{pmatrix} \rho_{AA} - \rho_{BB} & 2\rho_{BA} \\ -2\rho_{BA} & \rho_{AA} - \rho_{BB} \end{pmatrix} \tag{6.18}$$

where

$$\rho = \begin{pmatrix} C_{A0}C_{A0}^* & C_{A0}C_{B0}^* \\ C_{B0}C_{A0}^* & C_{B0}C_{B0}^* \end{pmatrix} = \begin{pmatrix} \rho_{AA} & \rho_{AB} \\ \rho_{BA} & \rho_{BB} \end{pmatrix} \tag{6.19}$$

is the density matrix [116], and where we have exploited the fact that $C_{A0}C_{B0} = -C_{A0}^*C_{B0} = -\rho_{AB} = -\rho_{BA}^*$. The state vector after the single jump is

$$\begin{pmatrix} C_A \\ C_B \end{pmatrix} = \begin{pmatrix} \rho_{AA} - \rho_{BB} \\ -2\rho_{BA} \end{pmatrix}. \tag{6.20}$$

Jumping across the resonance $2N-1$ times is described by the transfer matrix

$$U_{(2N-1)j} = \begin{pmatrix} \rho_{AA} - \rho_{BB} & 2\rho_{BA} \\ -2\rho_{BA} & \rho_{AA} - \rho_{BB} \end{pmatrix}^N = (\rho_{AA} - \rho_{BB})^N \begin{pmatrix} 1 & \beta \\ -\beta^* & 1 \end{pmatrix}^N \tag{6.21}$$

where $\beta = 2\rho_{BA}/(\rho_{AA} - \rho_{BB})$. If N is a power of 2, the amplitudes in states A and B will repeat the pattern for a single jump. Following multiple jump sequences, $P_{B,2N}$ increases relative to $P_{B,N}$ as long as $|P_{A,N} - P_{B,N}|^2 < P_{A,N}$. Once the average value of P_A is sufficiently small, we no longer expect to observe an increase in the enhancement with additional jumps. This is not surprising, as we do not expect additional enhancement once the transition is saturated.

To model the effects of the jump sequence applied to atoms in the experimental ensemble, we diagonalize the three-body Hamiltonian for detunings of ε and $-\varepsilon$, propagate the initial state through the electric field sequence, and average the transition probabilities over the nearest and next-nearest-neighbor distributions, as in section 6.2.1. The simulation predicts that for detuning greater than $3\Delta E/4$, additional jumps across the resonance lead to additional enhancement as shown in figure 6.12. For a detuning of $\Delta E/2$, the transition probability saturates after two jumps, and no additional enhancement is observed. This agrees with our experimental observation that the enhancement works best when the detuning is larger than $3\Delta E/4$. The inhomogeneous broadening likely makes larger detunings even more important because we can only observe enhancement when the detuning is larger than the inhomogeneous width. This restricts experiments to densities at which the resonances are broader than the inhomogeneous width by a factor of about $\sqrt{2}$. In practice, this corresponds to a density of about 1.7×10^9 cm^{-3}, where we can observe a non-negligible signal for detunings greater than 4 MHz.

At early times, the simulations for the jump electric field sequences show large amplitude oscillations in the transition probability which decay with increasing interaction duration. The duration of these prompt oscillations increases with the number of jumps and decreases as the detuning is increased. The oscillations persist for much longer times if interactions beyond nearest neighbors are suppressed. They are also strongly damped in the two-body case if 4 MHz of inhomogeneous linewidth broadening is added to the simulation. Others have observed similar oscillations in simulations of resonant energy transfer in cold Rydberg

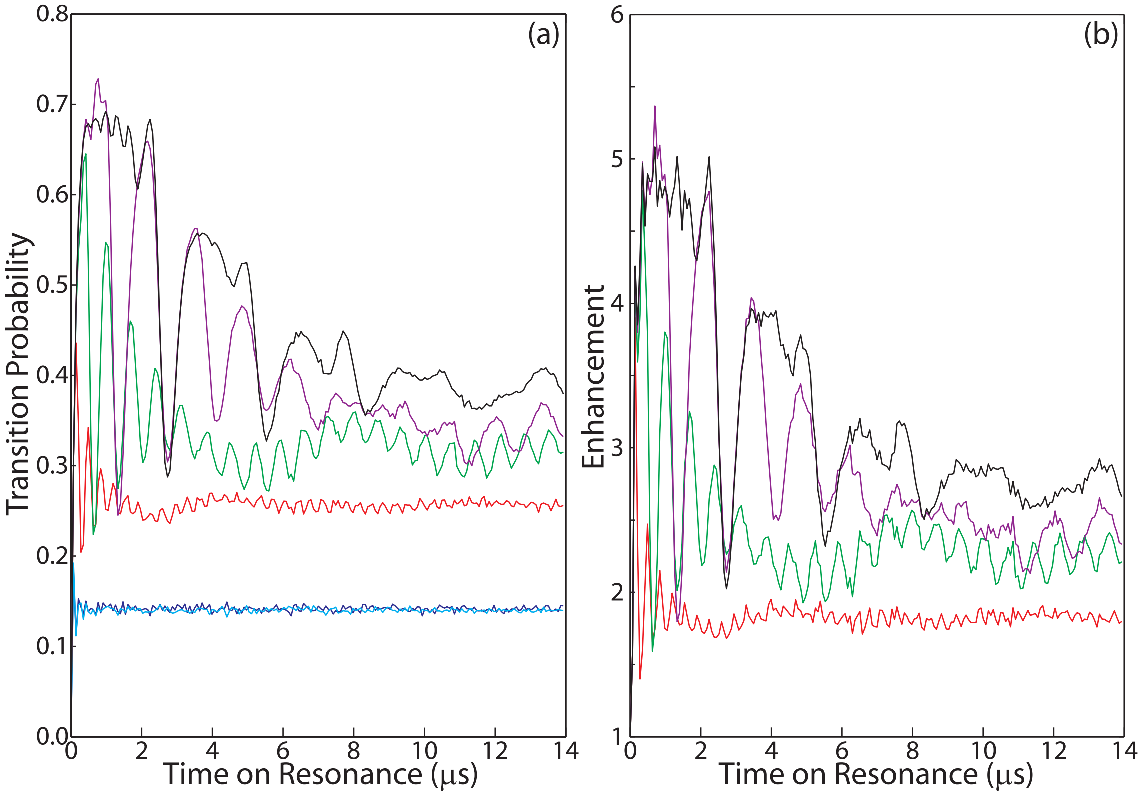

Figure 6.12: Simulated transition probabilities and enhancement factors as a function of the total interaction time for several different jump sequences. Ignoring inhomogeneous effects, we calculate the transition probability for the same parameters used to acquire the data shown in figure 6.6 (detuning 5.5 MHz, density 2×10^9 cm^{-3}) for electric field sequences with 1 jump (red), 3 jumps (green), 7 jumps (purple), 15 jumps (black) and no jump on the high (blue) and low (cyan) field sides of the resonance. (b) The enhancement in the transition probability for the jump sequences in (a). Note that after averaging over the prompt oscillations, the enhancement factors for 1 and 3 jumps are roughly constant and do not show the exponential decay observed in the experiments. For 7 and 15 jumps, the simulations show a decay in the enhancement similar to that seen for all jump sequences in the experiment. As discussed in the text, this decay in the calculations appears to be an artifact of the prompt oscillations which are not observed in the experiment. The decay in the 7 and 15 jump simulations arises from a *decrease* in the jump sequence transition probability while the experimentally observed decay is the result of a slow *increase* in the signal obtained when remaining on one side of the resonance.

gasses and have shown that these oscillations are eliminated if interactions between more atoms are explicitly included [108]. If we average over the short time oscillations in the simulations for zero, one and three jumps we find that the transition probabilities and enhancement factors are essentially independent of the total interaction time and do not show the experimentally observed exponential decay. This appears not to be the case for simulations involving seven and fifteen jumps, which show no rapid prompt oscillations under the same detuning and density conditions. However, the oscillations are observed for seven and fifteen jumps when the simulations are performed at lower density or at larger detunings. This fact, coupled with the large transfer probabilities predicted for the seven and fifteen jump sequences in figure 6.12, suggests that the absence of oscillations in these cases is due to saturation of the transition probability. Long term decay of the transition probability for large numbers of jumps is not observed in the experiments. Thus, its appearance in the simulation appears to be an artifact of the saturation of the oscillations in the transition probability which are also not observed experimentally. While the calculated decay in the enhancement for seven and fifteen jumps is very similar to the experimentally observed decay, it derives from a different source. The decay in the calculated enhancement curves results from a decline in the transition probability for the jump sequence while the decay of the experimental data results from the slow rise of the signal produced while remaining on one side of the resonance. Therefore, in the remainder of the analysis, we consider only fewer numbers of jumps where known artifacts from the simulations do not seem to impact the qualitative agreement with the experiments.

Decoherence on the time scale of tens microseconds could be caused by atom motion. The average atom in a 70 μK cloud with a density of 2.1×10^9 cm^{-3} travels the average interatomic distance in 32 μs but the dipole-dipole potential would be substantially changed by moving a fraction of this distance.

To model the effect of the atom motion on the enhancement, we diagonalize the three-body Hamiltonian while allowing one of the nearest neighbors to move in three dimensions

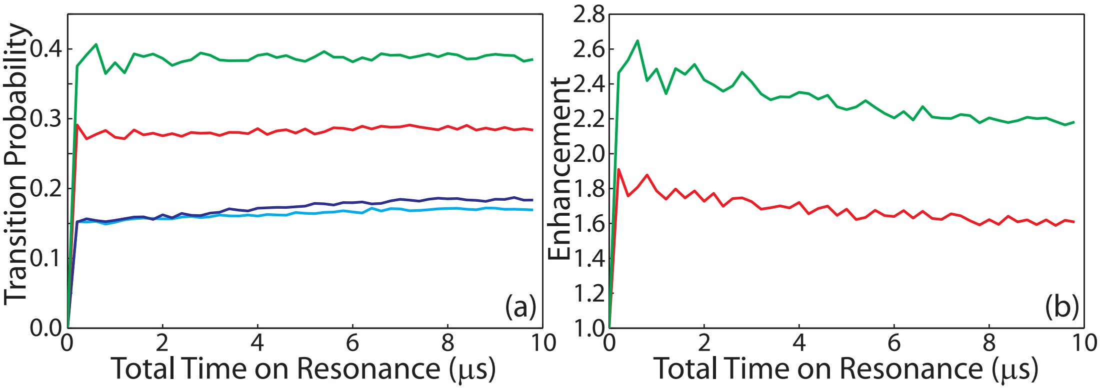

Figure 6.13: (a) Simulated transition probabilities and enhancements for zero, one and three jump sequences including atom motion. We simulate the effect of atom motion on the transition probability by allowing one of the nearest-neighbor atoms to move in three dimensions while the other two atoms remain fixed for the experimental parameters of the data shown in figure 6.6 (detuning 5.5 MHz, density 2×10^9 cm^{-3}, temperature of 70 μK) for electric field sequences of 1 jump (red), 3 jumps (green), and no jump on the high (blue) and low (cyan) field sides of the resonance. (b) Simulated enhancement in the transition probability associated with the curves in (a). The model shows a decay in the enhancement of the transition probability which is qualitatively similar to that observed experimentally in figure 6.7 for the 1 and 3 jump sequences.

with the root mean square velocity for a 70 μK ideal gas ($v_z = \sqrt{2kT/m}$ along the nearest-neighbor pair axis and $v_\rho = 2\sqrt{kT/m}$ in the perpendicular direction) while the other atoms remain fixed. As shown in figure 6.13, averaging over the nearest and next-nearest-neighbor distributions, we find a decay in the enhancement which is qualitatively similar to that observed experimentally for one and three jumps. Interestingly, the inclusion of atom motion averages out the prompt rapid oscillations from the simulation.

It is important to note some of the limitations of this simple moving atom model. Because the model includes only three atoms and only the average longitudinal and transverse relative speeds are used for all atom configurations, the net motion always results in increased separation of the atoms at long times. Once the nearest neighbors have moved out of interaction range, the probability that the atoms are in the p states is constant. There are no other atoms for the moving atom to come in contact with, nor do other atoms approach the stationary partner. The model also neglects the motion of the next-nearest neighbor, acceleration due to dipole-dipole forces, the loss of $25s$ state population due to spontaneous emission, and inhomogeneous broadening effects. Clearly a more complete model is necessary to make a quantitative comparison to the data. Nonetheless, this model indicates that thermal atom motion can lead to a time-dependent change in the interaction potential which is manifest as decoherence in the system. This decoherence leads to a decay in the enhancement of the transition probability when the jump sequence is applied.

To firmly establish if the dephasing is due to the atom motion, we would like to change the rate at which the atom pairs travel in and out of interaction range. This could be done either by changing the temperature of the atoms or by changing their density, both of which proved difficult in practice. We were unable to find an effective way to change the MOT temperature while holding the density stable. Also, the density range over which the enhancement can be measured is limited because the enhancement is only observable for detunings outside the inhomogeneous width, making it necessary for the resonance to be wider than 6 MHz. Unfortunately, it also becomes difficult to observe the enhancement at high densities once the two resonances begins to overlap because some signal acquired on the low field side of the $|m_j| = 3/2$ resonance is due to the $|m_j| = 1/2$ resonance. Despite these challenges, enhancement measurements were made for resonance widths of 5.5 MHz and 7.5 MHz, but the enhancement effect was not as pronounced. The data for the 5.5 MHz wide resonance was taken at a detuning of 5.2 MHz. The signal was small, leading to poor signal to noise. For the 7.5 MHz wide resonance where we detuned by 5.6 MHz, the $|m_j| = 1/2$ resonance overlapped with the low field side of the $|m_j| = 3/2$ resonance, diminishing the measured enhancement. Nonetheless, the enhancement for the 5.5 MHz and 7.5 MHz wide resonances do show a consistent exponential decays as shown in figure 6.14(a) and (b).

Figure 6.14(c) shows that decay rates for the 5.5 MHz and 7.5 MHz resonances do not differ (within the experimental uncertainty) from the decay rates shown for the 6.5 MHz resonance in figure 6.10(b). If the dephasing is due to atom motion, it is not surprising that

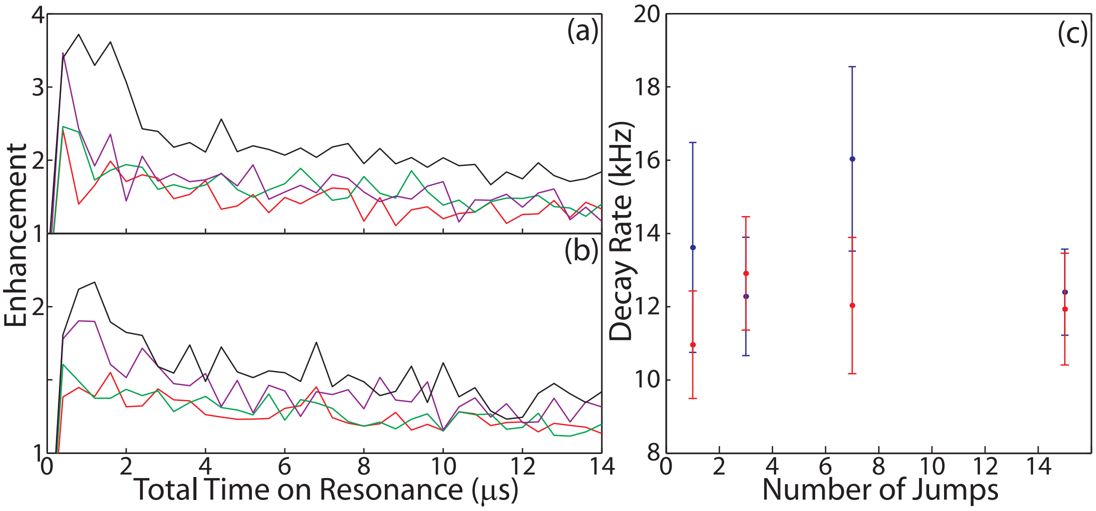

Figure 6.14: Decays in the enhancement for 5.5 MHz (a) and 7.5 MHz (b) wide resonances for 1 (red), 3 (green), 7 (purple) and 15 (black) jump sequences as a function of on-resonance time. (c) The decay rates of the data in (a) in blue and (b) in red do not differ within experimental accuracy from the decay rates for the 6.5 MHz wide resonance shown in figure 6.10.

the decay rates are virtually the same at these three densities. The average interatomic separation varies only from 3.9 μm to 5.1 μm, and typical atoms travel the average interatomic distance in 30 μs to 39 μs. The exponential fits to the enhancement for these resonances do not indicate a decrease in decay rate with multiple jumps across the resonance, but this maybe due to the poor signal quality, and further investigation is warranted.

In summation, we have demonstrated a novel technique that probes the coherence of resonant energy transfer in a cold Rydberg gas. We observe dephasing times of about 10 μs which is comparable to the 13 μs spontaneous emission lifetime of the 25s state. these coherence times are two orders of magnitude larger than the dephasing times measured using the Ramsey interference technique employed by Anderson *et al.* [110] and more than an order of magnitude longer than those measured in experiments employing rotary echoes in cold Rydberg gasses [38, 39]. Preliminary modeling indicates that atom motion may contribute to the observed the dephasing. Further investigation is necessary to confirm that atom motion is causing the dephasing and to determine whether the observed dephasing can be prevented by jumping across the resonance multiple times. Future work would be greatly aided by reducing the inhomogeneous contribution to the resonance width by improving the electric field homogeneity or by switching off the trapping magnetic field before initiating the resonant energy exchange process.

Chapter 7

Summary and Conclusions

The preservation of quantum-mechanical coherence remains a fundamental challenge to practical quantum computation. Developing methods to measure and prevent decoherence is an important first step to overcoming its deleterious effects and has been the focus of many of the experiments discussed in this dissertation. Although these experiments have focused on Rydberg atoms, many of the techniques demonstrated could be applied to other systems.

The lithium experiments described in chapters 3 and 4 demonstrate that many of the techniques originally developed to control dephasing and decoherence in NMR can be extended to other quantum systems. Specifically, we demonstrate the use of a population echo to measure the decoherence times in an ensemble of single qubits. Pulsed and continuous dynamic decoupling techniques are shown to prevent the loss of phase coherence. In the first instance, an electric field is used to toggle the spin-orbit coupling, flipping the qubit state vector and reversing the acquisition of phase in both qubit bases [5]. This bang-bang control may be applicable to other systems where internal or external interactions can be toggled rapidly.

In chapter 4, decoherence is suppressed by driving the lithium qubits with a resonant radio frequency control field. The control field dresses the qubit states, locking their energy separation to the rf frequency, provided the Rabi frequency is much greater than the dephasing rate [4]. This frequency locking is quite general and could be implemented via any coherent coupling. For example, in chapter 6, we observe that on resonance, the always resonant next-nearest neighbor energy exchange appears to have little effect on the $25s_{1/2}+33s_{1/2} \rightarrow 24p_{1/2}+34p_{3/2}$ resonant energy transfer. This is likely due to the fact that the resonant coupling is larger. The resonant interaction locks the phase probability amplitude oscillations to its Rabi frequency preventing energy transfer to next nearest neighbors. Other couplings could also be effective, including those involving multi-photon processes in ladder or lambda configurations. Both pulsed and continuous dynamic decoupling are powerful techniques for preventing decoherence because they do not require explicit knowledge of the decoherence mechanism.

Chapter 5 describes a method of reducing the relative velocities between interacting Rydberg atoms without the use of a chopper wheel. Although technical issues specific to our implementation precluded further investigation of the coherence of resonant energy exchange in the beam, this technique could allow for such inquiries without the expense of constructing a MOT. For example, in our implementation the average atomic transit time at 2 μs of delay is 790 ns which should provide sufficient time to perform a Ramsey interference measurement similar to the one that is described in chapter 6 provided slight higher densities could be achieved by using a different style of oven. Recent work by Saquent *et al.* [117] shows that resonant energy transfer can be effectively studied in velocity reduced beams. In general, this method might be used with other atomic or molecular systems, for example, to studying interactions between atoms or molecules excited to metastable or stable neutral or ionic states. Even lower temperatures could be achieved by combining this method with a super-sonic expansion.

In chapter 6, we use a novel coherent spectroscopy to measure a coherence time for the $25s_{1/2} + 33s_{1/2} \rightarrow 24p_{1/2} + 34p_{3/2}$ resonant energy exchange interaction which is much longer than dephasing times previously observed in a cold Rydberg gas [38, 39, 110]. Jumping across the resonance leads to an enhancement in the transition probability as long as the interaction remains coherent. The enhancement is observed to decay over several microseconds. Previous measurements of dephasing times using Ramsey interference [110] and rotary echoes [38, 39] showed dephasing times of less than one microsecond. The long coherence time we observe may make dipole-dipole coupled Rydberg atoms even more appealing candidates for quantum information processing [42, 45, 47, 91, 118–120] as such a long coherence time would allow for the implementation of dynamic decoupling schemes and quantum error correction. Our preliminary modeling suggests that the coherence time may be limited by atom motion and, therefore, could be extended using colder atoms in an optical or magnetic trap or Bose-Einstein condensate.

Future research in this system could proceed in a number of directions. The on-resonance time could be extend to observe when the enhancement completely dissipates, and thus, determine when the coherence of the system has been lost. However, this may not be possible as the on-resonance time is already longer than the spontaneous lifetime of the $25s$ state. Finding a method to change the MOT temperature might allow us to determine the contribution of the atom motion to the decay in the enhancement. This might also allow us to better assess whether multiple jumps can be used to prevent the loss of phase coherence in a method similar to that discussed in chapter 3. Switching off the magnetic field gradient prior to starting the energy exchange process would allow us to work at a wider range of densities, but this might not clarify the source of the dephasing as both the atom transit times and the nearest neighbor spacing would be changing. Furthermore, switching off the magnetic field poses a challenge because the process of switching off the coils induces a large amount of current which tends ring for several milliseconds. It would, therefore, be necessary to perform the experiments at a time when the induced current was passing through zero. Another direction that could be pursued would be to regularize the atomic spacing either by implementing a lattice [121] or by using the forces between Rydberg atoms to push the atoms into a more regular spacing [122]. Alternatively, we could explore the use of control fields to implement dynamic decoupling schemes similar to those discussed in chapter 3 and 4. For example, working with a single resonance, it might be possible to implement a true echo sequence. The echo might be implemented by tuning to resonance for a short time t, detuning completely off resonance to E for a variable time T, jumping to $-E$ on the other side of the resonance, and then returning to resonance for a final time t.

Resonant energy transfer might also be used to transfer phase coherence from one set of atoms to another. For example, a wave packet created in the $25s$-$24p$ atoms might be transferred to the $33s$-$34p$ atoms via the dipole-dipole interaction. For such a transfer to be successful, the dephasing and decoherence of the interaction must be well controlled making its observation another possible gauge of the decoherence.

The experiments discussed in this dissertation demonstrate a number of techniques for measuring and controlling dephasing and decoherence in Rydberg atom systems. Many of these control methods can be extended to other systems. The long coherence time we observe for the resonant energy transfer process indicates that cold Rydberg atoms are a promising system for quantum information processing.

Bibliography

[1] Continuum, Mountain View, CA. *Operation and Maintenance Manual for SureLite Lasers*, 1997.

[2] New Focus, San Jose, CA. *User's Guide: 6000 Vortex Series Tunable Diode Laser*, 2002.

[3] Harold J. Metcalf and Peter van der Straten. *Laser Cooling and Trapping.* Springer, 1999.

[4] R. S. Minns, M.R. Kutteruf, M.A. Commisso, and R.R. Jones. Decoherence suppression in a resonant driving field. *J. Phys. B*, **41**:074012, (2008).

[5] R. S. Minns, M. R. Kutteruf, H. Zaidi, L. Ko, and R. R. Jones. Preserving coherence in rydberg quantum bits. *Phys. Rev. Lett.*, **97**:040504, (2006).

[6] M. J. Renn, W. R. Anderson, and T. F. Gallagher. Resonant collision of K Rydberg atoms. *Phys. Rev. A*, **49**:908, (1994).

[7] R. Feynman. Simulating physics with computers. *International Journal of Theoretical Physics*, **21**:219, (1985).

[8] D. Deutsch. Quantum theory, the Church-Turing principle and the universal quantum computer. *Proc. R. Soc. Lond A.*, **400**:97, (1985).

[9] P. W. Shor. Algorithms for quantum computation: discrete logarithms and factoring. *Foundations of Computer Science, 1994 Proceedings., 35th Annual Symposium*, page 124, (1994).

[10] P. W. Shor. Algorithms for quantum computation: Discrete logarithms and factoring. *SIAM J. on Computing*, **26**:1474, (1997).

[11] A. R. Calderbank and P. W. Shor. Good quantum error-correcting codes exist. *Phys. Rev. A*, **54**:1098, (1996).

[12] R. Laflamme and et al. Perfect quantum error correcting code. *Phys. Rev. Lett.*, **77**:198, (1996).

[13] L. Viola and S. Lloyd. Dynamical suppression of decoherence in two-state quantum systems. *Phys. Rev. A*, **58**:2733, (1998).

[14] D. Vitali and P. Tombesi. Using parity kicks for decoherence control. *Phys. Rev. A*, **59**:4178, (1999).

[15] L. Viola, E. Knill, and S. Lloyd. Dynamical decoupling of open quantum systems. *Phys. Rev. Lett.*, **82**:2417, (1999).

[16] C. Search and P. R. Berman. Suppression of magnetic state decoherence using ultrafast optical pulses. *Phys. Rev. Lett.*, **85**:2272, (2000).

[17] L. M. Duan and G. C. Guo. Preserving coherence in quantum computation by pairing quantum bits. *Phys. Rev. Lett.*, **79**:1953, (1997).

[18] D. A. Lidar, D. Bacon, and K. B. Whaley. Concatenating decoherence-free subspaces with quantum error correcting codes. *Phys. Rev. Lett.*, **82**:4556, (1999).

[19] D. G. Croy, M. D. Price, W. Maas, E. Knill, R. Laflamme, W. H. Zurek, T. F. Havel, and S. S. Somaroo. Experimental quantum error correction. *Phys. Rev. Lett.*, **81**:2152, (1998).

[20] Nicolas Boulant, Lorenza Viola, Evan M. Fortunato, and David G. Cory. Experimental implementation of a concatenated quantum error-correcting code. *Phys. Rev. Lett.*, **94**:130501, (2005).

[21] J. Chiaverini, D. Leibfried, T. Schaetz, M. D. Barrett, R. B. Blakestad, J. Britton, W. M. Itano, J. D. Jost, E. Knill, C. Langer, R. Ozeri, and D. J. Wineland. Realization of quantum error correction. *Nature (London)*, **432**:602, (2004).

[22] T. B. Pittman, B. C. Jacobs, and J. D. Franson. Demonstration of quantum error correction using linear optics. *Phys. Rev. A*, **71**:052332, (2005).

[23] Paul G. Kwiat, Andrew J. Berglund, Joseph B. Altepeter, and Andrew G. White. Experimental verification of decoherence-free subspaces. *Science*, **290**:498, (2000).

[24] D. Kielpinski, V. Meyer, M. A. Rowe, C. A. Sackett, W. M. Itano, C. Monroe, and D. J. Wineland. A decoherence-free quantum memory using trapped ions. *Science*, **291**:1013, (2001).

[25] L. Viola, Evan M. Fortunato, Marco A. Pravia, Emanuel Knill, Raymond Laflamme, and David G. Cory. Experimental realization of noiseless subsystems for quantum information processing. *Science*, **293**:2059, (2001).

[26] J. B. Altepeter, P. G. Hadley, S. M. Wendelken, A. J. Berglund, and P. G. Kwiat. Experimental investigation of a two-qubit decoherence-free subspace. *Phys. Rev. Lett.*, **92**:147901, (2004).

[27] E. Fraval, M. J. Sellars, and J. J. Longdell. Method of extending hyperfine coherence times in Pr^{3+}:Y_2SiO_5. *Phys. Rev. Lett.*, **92**:077601, (2004).

[28] E. Fraval, M. J. Sellars, and J. J. Longdell. Dynamic decoherence control of a solid-state nuclear-quadrupole qubit. *Phys. Rev. Lett.*, **95**:030506, (2005).

[29] P. Facchi, D. A. Lidar, and S. Pascazio. Unification of dynamical decoupling and the quantum Zeno effect. *Phys. Rev. A*, **69**:032314, (2004).

[30] P. Facchi, S. Tasaki, S. Pascazio, H. Nakazato, A. Tokuse, and D. A. Lidar. Control of decoherence: Analysis and comparison of three different strategies. *Phys. Rev. A*, **71**:022302, (2005).

[31] Takao Aoki, Go Takahashi, Tadash Kajiya, Jun ichi Yoshikawa, Samuel L. Braunstein, Peter van Loock, and Akira Furusawa. Quantum error correction beyond qubits. *Nature Physics*, **5**:541, (2009).

[32] S. Damodarakurup, M. Lucamarini, G. Di Giuseppe, D. Vitali, and P. Tombesi. Experimental inhibition of decoherence on flying qubits via "Bang-Bang" control. *Phys. Rev. Lett.*, **103**:040502, (2009).

[33] C. O. Reinhold, S. Yoshida, J. Burgdorfer, B. Wyker, J. J. Mestayer, and F. B. Dunning. Large-scale quantum coherence of nearly circular wave packets. *J. Phys. B*, **42**:091003, (2009).

[34] S. Yoshida, C. O. Reinhold, J. Burgdorfer, W. Zhao, J. J. Mestayer, J. C. Lancaster, and F. B. Dunning. Electric dipole echoes in rydberg atoms. *Phys. Rev. Lett.*, **98**:203004, (2007).

[35] E. L. Hahn. Spin echoes. *Phys. Rev.*, **80**:580, (1950).

[36] H. Y. Carr and E. M. Purcell. Effects of diffusion on free precession in nuclear magnetic resonance experiments. *Phys. Rev.*, **94**:630, (1954).

[37] C. P. Slichter. *Principles of Magnetic Resonance.* Springer-Verlag, second edition, 1980.

[38] Ulrich Raitzsch, Vera Bendkowsky, Rolf Heidemann, Bjorn Butscher, Robert Low, and Tilman Pfau. Echo experiments in a strongly interacting Rydberg gas. *Phys. Rev. Lett.*, **100**:013002, (2008).

[39] Kelly Cooper Younge and Georg Raithel. Rotary echo tests of coherence in Rydberg-atom excitation. *New Journal of Physics*, **11**:043006, (2009).

[40] J. V. Hernandez and F. Robicheaux. Simulations using echo sequences to observe coherence in a cold Rydberg gas. *J. Phys. B*, **41**:195301, (2008).

[41] Thomas F. Gallagher. *Rydberg Atoms.* Cambridge University Press, 1994.

[42] D. Jaksch, J. I. Cirac, and P. Zoller. Fast quantum gates for neutral atoms. *Phys. Rev. Lett.*, **85**:2208, (2000).

[43] M. S. Safronova, C. J. Williams, and C. W. Clark. Optimizing the fast Rydberg quantum gate. *Phys. Rev. A*, **67**:040303, (2003).

[44] E. Brion, V. M. Akulin, D. Comparat, I. Dumer, G. Harel, N. Kbaili, G. Kurizki, I. Mazets, and P. Pillet. Coherence protection by the quantum Zeno effect and nonholonomic control in a Rydberg rubidium isotope. *Phys. Rev. A*, **71**:052311, (2005).

[45] M. D. Lukin, M. Fleischhauer, R. Cote, L. M. Duan, D. Jaksch, J. I. Cirac, and P. Zoller. Dipole blockade and quantum information processing in mesoscopic atomic ensembles. *Phys. Rev. Lett.*, **87**:037901, (2001).

[46] D. Tong, S. M. Farooqi, J. Stanojevic, S. Krishnan, Y. P. Zhang, R. Ct, E. E. Eyler, and P. L. Gould. Local blockade of Rydberg excitation in an ultracold gas. *Phys. Rev. Lett.*, **93**:063001, (2004).

[47] M. Saffman and T. G. Walker. Analysis of a quantum logic device based on dipole-dipole interactions of optically trapped Rydberg atoms. *Phys. Rev. A*, **72**:022347, (2005).

[48] Boris Vasil'evich Numerov. A method of extrapolation of perturbation. *Monthly Notices of the Royal Astronomical Society*, **84**:592, (1924).

[49] Boris Vasil'evich Numerov. Note on the numerical integration of $d^2x/dt^2 = f(x,t)$. *Astronomische Nachrichten*, **230**:359, (1927).

[50] John M. Blatt. Practical points concerning the solution of the Schrodinger equation. *J. Comput. Phys.*, **1**:382, (1967).

[51] Myron L. Zimmerman, Michael G. Littman, Michael M. Kash, and Daniel Kleppner. Stark structure of the Rydberg states of alkali-metal atoms. *Phys. Rev. A*, **20**:2251, (1979).

[52] Th. Forster. Zwischenmolekulare energiewanderung und fluoreszenz. *Annalen der Physik*, **437**:55, (1948).

[53] Orazio Svelto. *Principles of Lasers.* Plenum Press, 1976.

[54] D. S. Thomson, M. J. Renn, and T. F. Gallagher. Transform-limited collisions of K Rydberg atoms. *Phys. Rev. Lett.*, **65**:3273, (1990).

[55] T.W. Hansch. Repetitively pulsed tunable dye laser for high resolution spectroscopy. *Applied Optics*, **11**:895, (1972).

[56] Michael G. Littman and Harold J. Metcalf. Spectrally narrow pulsed dye laser without beam expander. *Applied Optics*, **17**:2224, (1978).

[57] Karen Liu and Michael G. Littman. Novel geometry for single-mode scanning of tunable lasers. *Optics Letters*, **6**:117, (1981).

[58] S. N. Pisharody, J. G. Zeibel, and R. R. Jones. Imaging atomic stark spectra. *Phys. Rev. A*, **61**:063405, (2000).

[59] CVC Products, Inc., Rochester, NY. *CVC Instruction Manual No. 6-70 B Rev. 8.*

[60] Gamma Vaccuum, Shakopee, MN. *Gamma Vaccuum General Brochure.*

[61] Gamma Vaccuum, Shakopee, MN. *Gamma Vaccuum Technical Bulletin 00.003.971 Ion Pumping of Cesium and Rubidium*, 2006.

[62] Gamma Vacuum, Shakopee, MN. *Ion Pump Users Manual*, 2000.

[63] Jason Zeibel. *Manipulating Wavepacket Dynamics with Half-Cycle Pulses.* PhD thesis, University of Virginia, 2003.

[64] F. Reif. *Fundamentals of Statistical and Thermal Physics.* McGraw-Hill, 1965.

[65] J.R. Veale, W. Anderson, M. Gatzke, M. Renn, and T.F. Gallagher. Line-shape analysis of resonant energy transfer collisions. *Phys. Rev. A*, **54**:54, (1996).

[66] F. B. Dunning and Randall G. Hulet, editors. *Atomic and molecular and Optical Physics: Atoms and Molecules, Volume 29B Experimental Methods in the Physical Sciences.* Academic Press, Inc., 1996.

[67] Giacinto Scoles, editor. *Atomic and molecular beam methods*, volume 1. Oxford University Press, 1988.

[68] C. Monroe, W. Swann, H. Robinson, and C. Wieman. Very cold trapped atoms in a vapor cell. *Phys. Rev. Lett.*, **65**:1571, (1990).

[69] E. L. Raab, M. Prentiss, Alex Cable, Steven Chu, and D. E. Pritchard. Trapping of nuetral sodium atoms with radiation pressure. *Phys. Rev. Lett.*, **59**:2631, (1987).

[70] Steven Chu, L. Hollberg, J. E. Bjorkholm, Alex Cable, and A. Ashkin. Three-dimensional viscous confinement and cooling of atoms by resonance radiation pressure. *Phys. Rev. Lett.*, **55**:48, (1985).

[71] SAES Getters S.p.A., Colorado Springs, CO. *Alkali Metal Dispensers.*

[72] Wenhui Li. *Probing Dipole-Dipole Interactions in a Frozen Rydberg Gas with Millimeter Waves.* PhD thesis, University of Virginia, 2005.

[73] T. Bergeman, Gidon Erez, and Harold J. Metcalf. Magnetostatic trapping fields for neutral atoms. *Phys. Rev. A*, **35**:1535, (1987).

[74] H. Ludvigsen, A. Aijala, A. Pietilainen, H. Talvitie, and E. Ikonen. Laser cooling of rubidium atoms in a vapor cell. *Physica Scripta*, **49**:424, (1994).

[75] Wolfgang Demtroder. *Laser Spectroscopy: Basic Concepts and Instrumentation, Second Enlarged Edition.* Springer-Verlag, 1996.

[76] IntraAction Corp, Bellwood, IL. *Model AOM-402AF3 Acousto-Optic Modulator Instruction Manual*, 2007.

[77] Jeremy J. Murray-Krezan. *Probing Start Atoms.* PhD thesis, University of Virginia, 2007.

[78] Xiangdong Zhang. *Probing Time-Dependent Electron Interactions in Double-Rydberg Wave packets.* PhD thesis, University of Virginia, 2008.

[79] Jianing Han. *Dipole effects in a cold Rydberg gas.* PhD thesis, University of Virginia, 2009.

[80] F. Robicheaux, C. Wesdorp, and L. D. Noordam. Selective field ionization in Li and rb: theory and experiment. *Phys. Rev. A*, **62**:043404, (2000).

[81] Stanford Research Systems, Sunnyvale, CA. *DG535 Digital Delay / Pulse Generator Operation and Service Manual*, 2002.

[82] Tektronix Inc., Beaverton, OR. *User Manual: AWG510 & AWG520 Arbitrary Waveform Generator*, 2000.

[83] Avtech Electrosystems LTD, Ottawa, Ontario Canada. *Instructions: Model AV-141F* $\times 10$ *Gain,* $\pm 5\,V$ *Output Pulse Amplifier with 4 ns Rise and Fall Times*, 2009.

[84] R. R. Jones and L. D. Noordam. Electronic wavepackets. *Adv. At., Mol., Opt. Phys.*, **38**:1, (1997).

[85] S. N. Pisharody and R. R. Jones. 2-electron dynamics of an atom. *Science*, **303**:813, (2004).

[86] T. C. Weinacht, J. Ahn, and P. H. Bucksbaum. Measurement of the amplitude and phase of a sculpted Rydberg wave packet. *Phys. Rev. Lett.*, **80**:5508, (1998).

[87] W. Zhao, J. J. Mestayer, J. C. Lancaster, F. B. Dunning, C. O. Reinhold, S. Yoshida, and J. Burdorfer. Engineering very-high-n polarized Rydberg states using tailored half-cycle-pulse sequences. *Phys. Rev. Lett.*, **95**:163007, (2005).

[88] W. Zhao, J. J. Mestayer, J. C. Lancaster, F. B. Dunning, C. O. Reinhold, S. Yoshida, and J. Burdorfer. Navigating localized wave packets in phase space. *Phys. Rev. Lett.*, **97**:253003, (2006).

[89] J. Ahn, D. N. Hutchinson, C. Rangan, and P. H. Bucksbaum. Quantum phase retrieval of a Rydberg wave packet using a half-cycle pulse. *Phys. Rev. Lett.*, **86**:1179, (2001).

[90] J. Ahn, T. C. Weinacht, and P. H. Bucksbaum. Information storage and retrieval through quantum phase. *Science*, **287**:463, (2000).

[91] L. Isenhower, E. Urban, X. L. Zhang, A. T. Gill, T. Henage, T. A. Johnson, T. G. Walker, and M. Saffman. Demonstration of a neutral atom controlled-NOT quantum gate. *Phys. Rev. Lett*, **104**:010503, (2010).

[92] T. Voft, M. Viteau, A. Chotia, J. Zhao, D. Comparat, and P. Pillet. Electric-field induced dipole blockade with Rydberg atoms. *Phys. Rev. Lett.*, **99**:073002, (2007).

[93] E. Arimondo, M. Inguscio, and P. Violino. Experimental determinations of the hyperfine structure in the alkali atoms. *Rev. Mod. Phys.*, **49**:31, (1977).

[94] T. H. Jeys, F. B. Dunning, and R. F. Stebbings. Quantum-beat echoes. *Phys. Rev. A*, **29**:379, (1984).

[95] E. Shapiro, I. A. Walmsley, and M. Yu Ivanov. Suppression of decoherence in a wave packet via nonlinear resonance. *Phys. Rev. Lett.*, **98**:050501, (2007).

[96] E. Collin, G. Ithier, A. Aassime, P. Joyez, D. Vion, and D. Esteve. NMR-like control of a quantum bit superconducting circuit. *Phys. Rev. Lett.*, **93**:157005, (2004).

[97] W. Demtroder. *Laser spectroscopy : basic concepts and instrumentation.* Springer, second enl. edition, 1996.

[98] Harald Friedrich. *Theorectical atomic physics.* Springer-Verlag, 1991.

[99] R. C. Stoneman, M. D. Adams, and T. F. Gallagher. Resonant-collision spectroscopy of Rydberg atoms. *Phys. Rev. Lett.*, **58**:1324, (1987).

[100] M. J. Renn and T. F. Gallagher. Ramsey interference fringes in radiatively assisted collisions of K Rydberg atoms. *Phys. Rev. Lett.*, **67**:2287, (1991).

[101] M. J. Renn, W. R. Anderson, and T.F. Gallagher. Frequency evolution of radiatively assisted collisions of K Rydberg atoms. *Phys. Rev. A*, **49**:409, (1994).

[102] Philip R. Bevington and D. Keith Robinson. *Data Reduction and Error Analysis.* McGraw-Hill Higher Education, third edition, 2003.

[103] F. Robicheaux, J. V. Hernandez, T. Topcu, and L. D. Noordam. Simulation of coherent interactions between Rydberg atoms. *Phys. Rev. A*, **70**:042703, (2004).

[104] David Scott Thomson. *Resonant Collisoins of Rydberg Atoms.* PhD thesis, University of Virginia, 1990.

[105] Milton Abramowitz and Irene A. Stegun, editors. *Handbook of Mathematical Functions With Formulas, Graphs, and Mathematical Tables.* U.S. Department of Commerce., 1972.

[106] William Robert Anderson. *Resonant Dipole-Dipole Collisions of Rydberg Atoms in a Magneto-Optical Trap.* PhD thesis, University of Virginia, 1990.

[107] B. Shirinzadeh and Charles C. Wang. Accurate determination of the vapor pressure of potassium using optical absorption. *Applied Optics*, **22**:3265, (1983).

[108] S. Westermann, T. Amthor, A. L. de Oliveria, J. Deiglmayr, M. Reetz-Lamour, and M. Weidemuller. Dynamics of resonant energy transfer in a cold Rydberg gas. *Eur. Phys. J. D*, **40**:37, (2006).

[109] B. Sun and F. Robicheaux. Spectral linewidth broadening from pair fluctuations in a frozen Rydberg gas. *Phys. Rev. A*, **78**:040701, (2008).

[110] W. R. Anderson, M. P. Robinson, J. D. D. Martin, and T. F. Gallagher. Dephasing of resonant energy transfer in a cold Rydberg gas. *Phys. Rev. A*, **65**:063404, (2002).

[111] W. R. Anderson, J. R. Veale, and T. F. Gallagher. Resonant dipole-dipole energy transfer in a nearly frozen Rydberg gas. *Phys. Rev. Lett.*, **80**:249, (1998).

[112] I. Mourachko, D. Comparat, F. de Tomasi, P. Nosbaum, V. M. Akulin, and P. Pillet. Many-body effects in a frozen Rydberg gas. *Phys. Rev. Lett.*, **80**:253, (1998).

[113] I. Mourachko, Wenhui Li, and T. F. Gallagher. Controlled many-body interactios in a frozen Rydberg gas. *Phys. Rev. A*, **70**:031401, (2004).

[114] Schott data sheet: BG39, 2004.

[115] Daniel A. Steck. "Rubidium 85 D line data" available online at http://steck.us/alkalidata (revision 2.1.2, 12 August 2009).

[116] Pierre Meystre and Murray Sargent III, editors. *Elements of Quantum Optics.* Springer., third edition, 1998.

[117] Nicolas Saquet, Anne Cournol, Jerome Beugnon, Jacques Robert, Pierre Pillet, and Nicolas Vanhaecke. Landau-Zener transitions in frozen pairs of Rydberg atoms. *Phys. Rev. Lett*, **104**:133003, (2010).

[118] T. Wilk, A. Gaetan, C. Evellin, J. Wolters, Y. Miroshnychenko, P. Grangier, and A. Browaeys. Entanglement of two individual neutral atoms using Rydberg blockade. *Phys. Rev. Lett*, **104**:010502, (2010).

[119] Ditte Moller, Lars Bojer Madsen, and Klaus Molmer. Quantum gates and multiparticle entanglement by Rydberg excitation blockade and adiabatic passage. *Phys. Rev. Lett*, **100**:170504, (2008).

[120] M. Muller, I. Lesanovsky, H. Weimer, H. P. Buchler, and P. Zoller. Mesoscopic Rydberg gate based on electromagnetically induced transparency. *Phys. Rev. Lett*, **102**:170502, (2009).

[121] K. C. Younge, B. Knuffman, S. E. Anderson, and G. Raithel. State-dependent energy shifts of Rydberg atoms in a ponderomotive optical lattice. *Phys. Rev. Lett.*, **104**:173001, (2010).

[122] M. L. Wall, F. Robicheaux, and R. R. Jones. Controlling atom motion through the dipole-dipole force. *J. Phys. B*, **40**:3693, (2007).